Università degli Studi di Firenze
Scuola di Ingegneria
DIEF - Department of Industrial Engineering of Florence

PhD School: *Energetica e Tecnologie Industriali ed Ambientali Innovative*
Scientific Area: ING-IND/08 - *Macchine a Fluido*

Numerical Analysis of Dynamics and Stability in Lean-Burn Gaseous Flames for Heavy Duty Gas Turbines

PhD Candidate: Ing. Daniele Pampaloni

Tutor: Prof. Ing. Bruno Facchini
Academic Supervisors: Dr. Ing. Antonio Andreini
Prof. C.O. Paschereit
PhD School Coordinator: Prof. Ing. Maurizio De Lucia

XXXI PhD School Cycle - 2015-2018

Acknowledgements

At the conclusion of a journey, it is normal to find yourself thinking about all the people who have contributed to the achievement of such an important goal. These few lines are certainly not sufficient to express my deep gratitude for you all.

First and foremost, I would like to thank Prof. Bruno Facchini for giving me this growth opportunity, not only from a professional, but also from a personal point of view. I am extremely grateful also to Ing. Antonio Andreini for his invaluable advice and constructive guidance, besides his comforting enthusiasm. My achievements would be unattainable without his help. I would like to thank Prof. C. O. Paschereit as well, for welcoming me at TUB and for all the support has given me during this thesis. My time in Berlin was a huge learning experience, not only academically, thanks to his great technical expertise, but also from a personal development perspective that I will always cherish. My warmest thanks also to all the TUB guys who helped me in living such a great experience.

My gratitude to the members of the Aerothermal Combustion Team of BHGE-Nuovo Pignone; it is indeed a pleasure and an honour to have the possibility to work with them.

Many thanks and my warmest regards to my former colleagues: Lorenzo M. and Alessandro (the supervisors of my former thesis: it's your fault I got here!), Lorenzo W. and Stefano. A special thank to all the members of the HTC group, in which I found the warmth of extraordinary people: Davide (we did it, at last!), Lorenzo C. (how many trips together!), Sabrina, Andrea, Dominique, Matteo (without your IT assistance this result would not be possible!), Simone, Lorenzo P., Carlo, Tommaso, Leonardo and Pier Carlo (a right-hand man during the last year: I feel particularly in debt with you!), as well as all the lab-guys at THT.

Finally, I would like to thank my whole family for believing and for supporting me in all my choices. If I have been able to arrive here, I owe it to you all.

Mi fan patir costoro il grande stento,
Che vanno il sommo bene investigando,
E per ancor non v'hanno dato drento.
E mi vo col cervello immaginando,
Che questa cosa solamente avviene
Perché non è dove lo van cercando.
Questi dottor non l'han mai intesa bene,
Mai son entrati per la buona via,
Che gli possa condurre al sommo bene.
Perché, secondo l'opinion mia,
A chi vuol una cosa ritrovare,
Bisogna adoperar la fantasia,
E giocar d'invenzione, e 'ndovinare;
E se tu non puoi ire a dirittura,
Mill'altre vie ti posson aiutare.

Galileo Galilei

Abstract

Lean burn combustion represents the state-of-the-art technology for heavy-duty gas turbine applications, as it provides limited NO_x and soot emissions. However, one of the main issues in lean burn technology development is the stability of the combustion process that becomes more susceptible to thermo-acoustic instabilities and blow-off events.

From a design perspective, a depth insight on lean burn combustion is required and Computational Fluid Dynamics (CFD) can be an useful tool for this purpose. Several interacting phenomena are involved in flame dynamics and various modelling strategies, with huge differences in terms of computational costs, are available. This research activity is therefore aimed at developing numerical tools, to be used in an industrial design process, which are able of describe these complex phenomena and provide reliable predictions.

Considering thermo-acoustic instabilities, direct computational simulations of the entire combustor, solving most part of the range of length scales involved, from the tiny chemical reaction scales and small turbulent low scales to the very long acoustic wavelengths, although possible, are impractical in the industrial framework.

Decoupling the calculations of the perturbed flame response and the acoustic waves is a much less time-consuming approach: the generation, propagation and reflection/transmission of the acoustic waves can be captured by either a low-order acoustic network model or a 3D Helmholtz solver, whereas the unsteady heat release rate resulting from acoustic excitation can be characterized via numerical simulations.

To this end, both linear and nonlinear flame modelling can be used, making use of the so-called Flame Transfer Function (FTF) and Flame Describing Function (FDF). FTF represents the response of the flame to small amplitude perturbations and can thus be only used to predict whether a thermo-acoustic system is stable (without oscillations) or unstable (increasing oscillations). However, in order to predict not only the

onset of pressure oscillations, but also their amplitude (and, as a consequence, their impact on the engine reliability), the non-linear response of the flame, such as the FDF, should be modelled.

In the first part of the dissertation the state-of-the-art numerical procedure for linear thermo-acoustic analysis has been applied to the study of a practical Baker Hughes GE gas turbine combustor, with the aim of giving more physical insight on the dynamic behaviour of the flame and understanding the driving mechanism as well. Experimental results from a recent campaign performed by BHGE on a full-scale annular combustor have been exploited for validation purposes. A multi-step approach has been followed, calculating the flame response to acoustic perturbations by means of transient CFD simulations coupled with System Identification techniques (CFD-SI) and building a Finite Element model of the combustor to be exploited for stability analysis. The wide range of tested operating conditions represents an opportunity to validate the numerical approach, so that several sensitivities to the main operating parameters have been performed, highlighting their impact on flame response. Furthermore, concerning the acoustic model, a boundary condition for rotational periodicity based on Bloch-Wave theory has been implemented and validated against full-annular chamber simulation, allowing a significant reduction in computational time. Several improvable aspects are also highlighted, pointing the way for further enhancements.

In this framework, in the second part of the work, two lab-scale combustors have been considered in order to develop numerical tools and methods to be employed for the investigation of real flames dynamics.

Concerning thermo-acoustics, in order to assess the prediction improvements that can be obtained with a so-called weakly nonlinear analysis, an atmospheric lean premixed combustor investigated at the Technical University of Berlin has been numerically studied for validation purposes, exploiting a multi-step approach. As the first step, the FDF calculation from Large Eddy Simulations (LES) has been performed. Then, frequency-domain calculations using a 3D Helmholtz solver have been carried out, in order to predict not only the onset of pressure oscillations, but also their amplitude. Results have been compared against experimental measurements and self-excited LES simulations, showing the improved prediction capability with respect to the commonly used linear stability analysis.

Regarding blow-off predictions, most works has been carried out with experimental methods and therefore the availability of a detailed model during the design phase to predict blow-off inception would reduce project iterations and avoid many expensive tests on prototypes. Due to the

complexity of the involved phenomena, the direct numerical simulation represents a real challenge for modellers and requires a comprehensive description of turbulence-chemistry interaction to investigate in detail the blow-off inception and dynamics. In this framework, the correct account for high strain levels, combined with the heat loss of the flame, can be extremely important, as highlighted in the last part of the dissertation, where an atmospheric lean premixed combustor investigated at the University of Cambridge has been analysed through numerical calculations. The blow-off inception and dynamics have been investigated, allowing detailed observations of the flame characteristics just before the complete extinction.

Contents

List of Figures

List of Tables

Nomenclature

A	Area	$[m^2]$
a	Strain rate	$[1/s]$
A	Zimont model constant	$[-]$
B	Constant in g_{cr} correlation	$[-]$
c	Progress variable	$[-]$
C_s	Smagorinsky constant	$[-]$
Co	Courant number	$[-]$
D	Molecular diffusivity	$[m^2/s]$
D_b	Bluff body diameter	$[m]$
D_e	External diameter of burner	$[m]$
D_t	Turbulent mass diffusivity	$[m^2/s]$
Da	Damkhöler number	$[-]$
E_a	Activation energy	$[-]$
G	Stretch factor	$[-]$
g_{cr}	Critical strain threshold	$[1/s]$
k	Turbulent kinetic energy	$[m^2/s^2]$
Ka	Karlovitz number	$[-]$
L_k	Kolmogorov length	$[m]$
L_t	Turbulence integral length scale	$[m]$
Le	Lewis number	$[-]$
$\dot{m}$	Mass flow rate	$[kg/s]$
Ma	Markstein number	$[-]$
$\boldsymbol{n}$	Normal vector to the flame front	$[-]$
p	Pressure	$[Pa]$
$P(\cdot)$	Probability density function	$[-]$
Pr	Prandtl number	$[-]$
R	Specific gas constant	$[J/kgK]$
Re	Reynolds number	$[-]$
s	ITNFS factor	$[-]$
S_c	Consumption speed	$[m/s]$
S_l	Laminar flame speed	$[m/s]$
S_l^0	Unstretched laminar flame speed	$[m/s]$
S_N	Swirl number	$[-]$
S_t	Turbulent flame speed	$[m/s]$
Sc	Schmidt number	$[-]$
t	Time	$[s]$

T_{ad}	Temperature of products at adiabatic conditions	$[K]$
T_{prod}	Products temperature	$[K]$
T_u	Unburned gas temperature	$[K]$
T_w	Wall temperature	$[K]$
u'	Velocity fluctuation	$[m/s]$
u	Velocity	$[m/s]$
u'_{Δ}	Subgrid turbulent velocity fluctuation	$[m/s]$
U_b	Bulk flow velocity at burner exit	$[m/s]$
x	Spatial coordinate	$[m]$
Y	Species mass fraction	$[-]$
z	Mixture fraction	$[-]$

Acronyms

BO	Blow-Off
BDF	Burner Describing Function
CFD	Computational Fluid Dynamics
CMC	Conditional Moment Closure
CRZ	Corner Recirculation Zone
DES	Detached Eddy Simulation
DNS	Direct Numerical Simulation
FEM	Finite Element Method
FFT	Fast Fourier Transformation
FGM	Flamelet Generated Manifold
FTF	Flame Transfer Function
FDF	Flame Describing Function
FR	Finite Rate
IRZ	Inner Recirculation Zone
$ITNFS$	Intermittent Turbulence Net Flame Stretch
LBO	Lean Blow-Off
LDA	Laser Doppler Anemometry
LDV	Laser Doppler Velocimetry
LES	Large Eddy Simulation
LFL	Lower Flammability Limit
LFS	Laminar Flame Speed
LHV	Lower Heating Value
LP	Lean Premixed
LPP	Lean Premixed Prevaporized
NSE	Navier-Stokes Equations
PDA	Phase Doppler Anemometry
PDF	Probability Density Function
PFR	Product Formation Rate
$PLIF$	Planar Laser Induced Fluorescence
$RANS$	Reynolds-Averaged Navier-Stokes
RQL	Rich Quench Lean
RZ	Recirculation Zone
SAS	Scale Adaotative Simulation
TFC	Turbulent Flame Closure
TFS	Turbulent Flame Speed

UDF	User-Defined Function
$URANS$	Unsteady Reynolds-Averaged Navier-Stokes

Greeks

α	Thermal diffusivity	$[m^2/s]$
β	Heat loss coefficient	$[-]$
δ	Laminar flame front thickness	$[m]$
Δ	LES Filter length	$[-]$
δ_{ij}	Kronecker delta	$[-]$
δ_l^0	Unstretched laminar flame front thickness	$[m]$
$\dot{\omega}_c$	Progress variable source term	$[1/s]$
ε	Turbulent kinetic energy dissipation	$[m^2/s^3]$
γ	Gas expansion parameter	$[-]$
Γ_k	Efficiency function	$[-]$
κ	Flame stretch	$[1/s]$
$\mathcal{L}$	Markstein length	$[m]$
ν	Kinematic viscosity	$[m^2/s]$
ν_t	Turbulent viscosity	$[m^2/s]$
ϕ	Equivalence ratio	$[-]$
ϕ_{BO}	Experimental blow-off equivalence ratio	$[-]$
ρ	Density	$[kg/m^3]$
σ	ITNFS factor	$[-]$
σ_ε	Standard deviation of ε distribution	$[-]$
τ_Δ	Subgrid turbulence time scale	$[s]$
τ_c	Characteristic chemical time scale	$[s]$
τ_t	Turbulence integral time scale	$[s]$
θ	Swirler blade angle respect to axis	$[deg]$
φ	Heat loss parameter	$[-]$

Subscripts

0	Initial Value
eq	Equilibrium Value
in	Inlet
$mean$	Mean Value
ref	Reference Value

Miscellaneous

$(\tilde{\bullet})$	Favre-averaged and Favre-filtered quantity
$(\bar{\bullet})$	Reynolds-averaged and Reynolds-filtered quantity

Introduction

Lean Premixed Combustion (LPC) is by now a reference technology in heavy-duty gas turbine framework, given its ability in reducing NO_X when compared to non-premixed systems. In fact, NO_X formation rate drastically depends on the mixture composition and temperature peaks within the combustion chamber and particular attention has to be therefore devoted to the preparation of the fuel-air mixture. In LPC systems fuel and air are directly premixed within the injector to avoid the creation of non-uniform near-stoichiometric mixture inside the combustor and allowing to local control the flame temperature. Dedicated designs have been developed, where complex flowfields, high turbulence regions and swirled flows are realized within the burner in order to promote the homogeneous mixing between fuel and air.

On the other hand, LPC systems operate very close to the lean flammability limit, the point at which the fuel/air ratio is too lean to support combustion, and thus can be very sensitive to unsteady phenomena such as thermo-acustic instabilities or even global extinction (Blow-Off). Such phenomena may damage combustor's component and limit the range of stable operating conditions, so that their study is of extreme technical importance during the earlier stages of the design process, in order to avoid inefficient design-built-measurement cycles. In fact, one of the primary requirements of a gas turbine combustor is that combustion must be maintained stable over a wide range of operating conditions and operational flexibility is gaining more and more importance in the development of future combustion systems.

In this framework, considering the complexity of the physical phenomena involved, Computational Fluid Dynamics (CFD) has become a powerful tool in the design of the combustion chamber since it is able to provide detailed information about the reacting flow-field. The numerical simulation of gas turbine involves the interaction of many complex physical processes that strongly affect the prediction accuracy, such as

turbulent mixing and chemical reactions.

In an industrial framework, RANS (Reynolds Averaged Navier Stokes) approaches, where only the mean flow is solved and turbulence effects are introduced by means of ad hoc models, represents a standard tool. However, due to the relevance of turbulent mixing processes and unsteady phenomena, RANS techniques are often insufficient or not completely able to properly characterize the complexity of such devices . Therefore, Scale-Resolving Simulations such as Large-Eddy Simulation (LES) are achieving a growing attention and they have been already widely applied for the simulation of practical flames.

Thermo-acoustic Analysis Direct simulations of combustion instabilities, solving most part of the range of length scales involved, from the tiny chemical reaction scales and small turbulent low scales to the very long acoustic wavelengths, although possible, are impractical in the industrial framework. The flame itself interacts with acoustic waves within the CFD simulation, without the introduction of external perturbations, and thus the approach is often referred as *Self Excited*.

Decoupling the calculations of the perturbed flame response and the acoustic waves is a much less time-consuming approach: the generation, propagation and reflection/transmission of the acoustic waves can be captured by either a low-order acoustic network model or a 3D Finite Elements Method (FEM) solver, whereas the unsteady heat release rate resulting from acoustic excitation can be characterized via experimental, analytical models or numerical simulations. This decoupled procedure, after a linearization, can be recast into a linear stability analysis, in order to identify frequency, shape and growth rate of the unstable acoustic modes.

In order to model the fluctuating heat release due to the flame response on the system acoustics a deep understanding and a proper description of the flame dynamics are necessary. The flame can be considered a black-box input-output system, with the driving mechanisms as inputs and the unsteady heat release as output. Therefore, assuming a linear behaviour, each input is usually related to the output through a so-called Flame Transfer Function (FTF). FTF represents the response of the flame to small amplitude perturbations and can thus be only used to predict whether a thermo-acoustic system is stable (without oscillations) or unstable (increasing oscillations).

However, in order to predict not only the onset of pressure oscillations, but also their amplitude (and, as a consequence, their impact on the engine reliability), the non-linear behaviour of the system should be

modelled. In fact, the limit cycle amplitude is the result of the balance between the acoustic energy production, induced by the fluctuating heat release of the flame, and his losses, mainly viscous damping and losses through the boundaries, as shown in Figure 1. Furthermore, noise or non-normal effects may trigger finite amplitude oscillations, even when the thermoacoustic system is linearly stable: in these situations linear stability fails to predict the real behaviour of the system [29].

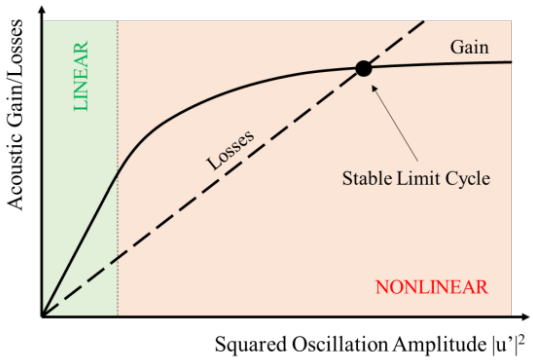

Figure 1: Acoustic energy balance between production and losses.

Within the thermo-acoustic framework, there are three main sources of nonlinearities:

- Gas dynamics, of primary importance to rocket engines;
- Damping due to different mechanisms, such as acoustic radiation, attenuation by suspended particles and baffle or orifices [30];
- Flame response, which represents the main source of nonlinearities for gas turbines and, thus, will be the only one considered in this work [31].

Considering the flame as the dominant non-linear term [31], its behavior is often described in terms of Flame Describing Function (FDF), a generalized Flame Transfer Function where both the gain and the phase of the response may depend on perturbation amplitude. Examples of experimental measurement [32], modelling [31] or CFD simulation [11] of nonlinear flame dynamics can be found in literature.

When the FDF is coupled with an acoustic solver and the stability analysis are repeated in the frequency domain at different excitation amplitudes, the approach is defined as *weakly nonlinear*, due to the fact that several assumption have to be done: the FDF analysis cannot be used to predict the behaviour of non-periodic oscillations and, due to the assuption that the dynamics of a given thermoacoustic mode is decoupled from the dynamics of the others, nonlinear coupling between the modes cannot be retrieved.

Analytical FTF and FDF formulations are in many cases inadequate to represent the complex physics lying behind the flame dynamics and the experimental determination of such quantities for configurations of technical interest is unfortunately very difficult and costly. The flame response to incoming perturbations can be also retrieved from computational time series data generated with unsteady CFD simulations, where the flame dynamics is reproduced. Concerning FTF, exciting the system with a carefully designed broadband signal and exploiting the linearity assumption, system identification (SI) techniques can be used to calculate the flame response over a range of frequencies from one single CFD run. FDF, instead, can be obtained using single frequency harmonic signals at different perturbation amplitude levels, requiring numerous simulations to calculate the whole flame response.

Lean Blow-off Predictions The ability to accurately predict the lean stability limit would allow designs to be explored numerically in greater detail, resulting in an increased ability to understand the underlying physics and to provide useful guidelines for the design processes. However, the numerical simulation of such a complex phenomenon represents a real challenge for modellers, since detailed modelling of turbulence and chemistry with their interactions is essential. For this reason, simplified numerical procedure, such as hybrid modelling based on the separation of fluid dynamics and combustion chemistry are often unable to predict the unsteady local extinctions due to turbulent fluctuations which trigger the blow-off event.

Therefore, the accurate prediction of Lean Blow-Off (LBO) relies on the direct unsteady simulation of the extinction process. However, only advanced combustion models where the turbulence-chemistry interaction is accurately implemented are suitable. The LES approach is inherently unsteady, and results the favourite tool to study transient phenomena like LBO process. The resolution of large turbulent eddies allows a more accurate calculation of the main mixing mechanisms and provides a consistent base for combustion. Despite the combustion still requires

modelling, flame prediction with LES presents significant improvements with respect to simpler approaches [33]. In the perspective of accurately predict the blow-off, local interactions between turbulent fluctuations and flame are fundamental since induce local extinctions and change the flame structure. The proper computation of these phenomena is possible only with a LES approach in practical applications.

These advantages however require high computing resources and this complicates the introduction in the design cycle, which must justify the high cost. In addiction to the prediction of the LBO limit, the high spatial and time accuracy of LES simulation allows the researchers to investigate with an extraordinary detail on the flame dynamics approaching blow-off. Such possibility represents a great advantage with respect to experimental diagnostics, that are often invasive or limited in resolution.

Aim of the work

The main aim of the present research work has been the development of numerical tools, to be used in an industrial design process, which are able to describe flame dynamics phenomena and provide reliable predictions of blow-off inception and thermo-acoustic instabilities. Since such numerical tools and methodology are intended to be used within an industrial framework, particular attention has been devoted to find a trade-off between computational costs and a meaningful representation of the involved phenomena.

In fact, in the first part of the dissertation, the state-of-the-art numerical procedure for linear thermo-acoustic analysis has been applied to the study of a practical Baker Hughes GE (BHGE) gas turbine combustor. The procedure has been validated against the results available from a recent experimental campaign performed by BHGE on a full-scale annular combustor and several sensitivities have been carried on, providing useful information for the design process and for future nozzle design improvements. The linear flame response to acoustic perturbations has been calculated by means of transient CFD simulations coupled with System Identification techniques (CFD-SI). Furthermore, to obtain a significant reduction in computational time, a thermo-acoustic model based on Bloch-Wave theory and exploiting rotational peridicity has been implemented and validated against linear stability analysis of the full-annular domain. Several improvable aspects have also been highlighted, pointing the way for further enhancements.

In the second part of the dissertation simple flame configurations have been numerically investigated in order to develop ad-hoc models and

strategies to be applied to practical burners for heavy-duty applications.

Concerning thermo-acoustics, an atmospheric lean premixed combustor investigated at the Technical University of Berlin has been chosen to carry on weakly nonlinear thermo-acoustic analysis exploiting a multi-step procedure. At first, the FDF has been calculated by means of LES simulation. Results have been compared against experimental measurements, showing the capability of the proposed methodology to reproduce the complex flame dynamics, such as the nonlinear response saturation and the interaction between acoustic and swirl number oscillations. Then, a 3D FEM model of the lab-scale combustor has been used to perform frequency-domain calculation, varying the perturbation amplitude, in order to predict the frequency and the limit cycle amplitude of pressure oscillations. Finally, results have been compared and validated against experimental measurements and Self-Excited LES simulations.

Regarding blow-off predictions, an atmospheric lean premixed combustor investigated at the University of Cambridge has been analysed through numerical calculations. The blow-off inception and dynamics have been directly simulated, allowing detailed observations about the flame behaviour approaching extinction and its precursors. In this framework, the correct account for high strain levels results crucial for an accurate prediction of the flame behaviour. To this end, a correction to account for flame stretch and heat loss effects has been implemented within the FGM model and validated against detailed experimental measurement over different operating conditions approaching blow-off.

Thesis outline

During this research activity, several aspects related to flame dynamics and stability have been analysed through numerical calculations, exploiting both CFD and FEM calculations and implementing ad-hoc models, boundary conditions and post-processing tools. The dissertation will be organized as described below.

Chapter 1: The research context of the work is presented. The chapter is focused on the limitations that characterize low-emission heavy-duty combustors, mainly in terms of flexibility and stability of the combustion process. Moreover, the basics of the theory of thermo-acoustic instabilities and lean blow-off are given and their phenomenology is here reviewed to better clarify the complexity that characterizes the study of flame dynamics and stability.

Chapter 2: An overview about commonly used numerical methods is reported in order to explain the background and the context in which this research activity has been performed. Following, theoretical notions on flames dynamics investigation and modelling exploiting important results from the literature are given, with particular focus on advanced numerical methods to be applied for the design of next generation combustors, such as nonlinear thermo-acoustic analysis based on Flame Describing Function calculation and direct simulation of lean blow-off inception.

Chapter 3: This chapter provides details on the numerical methods, strategies and post-processing techniques used in this work. Regarding CFD, the implementation of flame stretch and heat loss correction, which has proven to allow an accurate prediction of flame dynamics and stability is presented, as well as the basics of flame response identification. Concerning FEM, weakly nonlinear thermo-acoustics analysis and Bloch-Wave theory are also presented herein.

Chapter 4: The dynamics of a lean full-annular combustor for heavy-duty applications has been numerically studied in this chapter. The well established CFD-SI method has been used to investigate the flame response varying operational parameters such as flame temperature and fuel split. Concerning the acoustic model, a boundary condition for rotational peridicity based on Bloch-Wave theory has been implemented and validated against full-annular chamber simulation, allowing a significant reduction in computational time. Several improvable aspects have been highlighted, in the perspective of future works of nozzle design improvement.

Chapter 6: An atmospheric lean premixed combustor investigated at the Technical University of Berlin has been numerically studied in this chapter. A multi-step approach to perform weakly nonlinear thermo-acoustic analysis is presented and validated against experimental measurements. At first, the FDF identification from Large Eddy Simulations has been performed. Then, frequency-domain calculations using a 3D Helmholtz solver have been carried out and the amplitude and frequency of the pressure oscillation limit cycle are accurately retrieved. Finally, through the comparison against experimental measurements and self-excited LES simulations, the improved prediction capability with respect to the commonly used stability analysis has been shown.

Chapter 5: A premixed swirl burner experimentally studied at Cam-

bridge University has been investigated in this chapter, by means of LES, exploiting a correction that include specifically, in the FGM context, the physical effects of flame front stretching and heat loss and thus allows a better prediction of the fragmentation of the flame structure that triggers the blow-off event. A numerical procedure to trigger the flame extinction is presented: the blow-off is directly simulated, exploting an accelerate multi-step reduction of equivalence ratio at the inlet and analysing the history of chamber volume-averaged quantities during the transient. Results highlight the accuracy in predicting the blow-off event and allow a deeper insight into the phenomenology.

In the last chapter, a summary of the main achievements of this research is given together with conclusions and recommendations for future works.

Chapter 1

Technical Background

The research context of the work is presented in this chapter, focusing on the limitations that characterize low-emission heavy-duty gas turbine combustors, mainly in terms of flexibility and stability of the combustion process. Moreover, the basics of the theory of thermo-acoustic instabilities and blow-off are given and their phenomenology is here reviewed to better clarify the complexity that characterizes the study of flame dynamics ad stability.

1.1 Development of Industrial Low-Emission Gas Turbine Combustors

Gas turbines for power generation and heavy-duty applications typically used diffusion flame combustors because of their reliable performance and reasonable stability ranges [34]. The poor mixing characteristics of the commonly used diffusion burners created many performance problems, not the least being a high rate of pollutant emissions formation in the primary zone, in particular NO_X. During the years, the regulation for pollutant emissions has become more and more strict, leading engine manufacturers to develop combustors with increasingly low levels of emissions. Among all the factors determining pollutants formation, the most important is by far the temperature within the reaction zone [1].

As shown in Figure 1.1, by operating lean, the combustion temperatures at which NO_X formation rates start to accelerate can be avoided while the oxidation of unburned hydrocarbons as well as carbon monoxide can be improved. The most straightforward way to achieve locally lean conditions is to premix the fuel and air, with the introduction of the

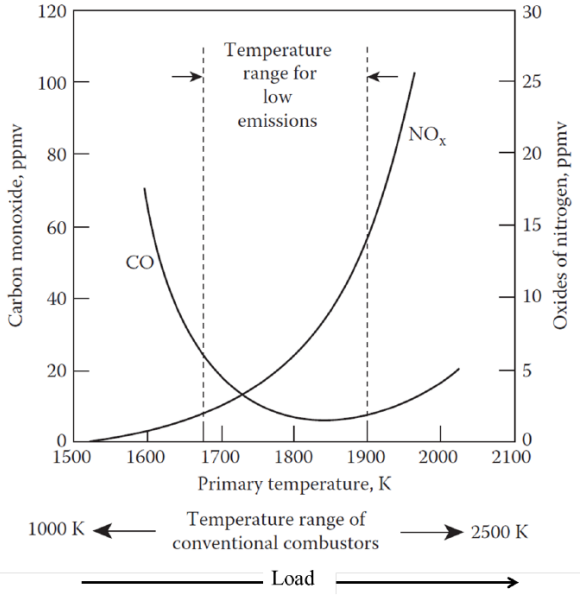

Figure 1.1: Influence of primary zone zone temperature on main pollutant emissions [1].

so-called Lean Premixed Combustion (LPC). This technologies represents nowadays the baseline of the combustion chambers in heavy-duty gas turbines. The lean premixed combustion demands very tight control of the fuel/air ratio over the entire load range, so the fuel and air are premixed accurately upstream of the combustor to avoid the formation of stoichiometric regions. The temperature in the combustion zone is strictly controlled with a precise low equivalence ratio and excess air in order to virtually eliminate the thermal NO_X formation source.

Typical lean combustion systems involve mixing the fuel and air far upstream of the reaction zone, since longer residence time in the premixer will benefit the mixedness before entering the primary combustion zone. Efficient premixing is also achieved by high turbulence in the mixing region. A way of achieving this is by introducing swirl in the injector: as an example, in Figure 1.2 is depicted a widely employed GE burner for industrial gas turbines, the Dual Annular Counter Rotating Swirl

(DACRS) injector, where the fuel is injected within the swirler passages and the mixing with the feeding air is enhanced by the interaction of the two swirled flows.

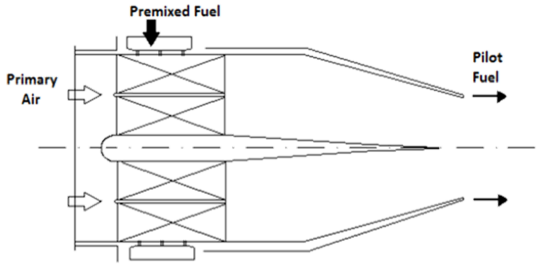

Figure 1.2: GE Double Annular Counter Rotating Swirl Nozzle for heavy-duty lean premixed combustor [2].

However, the intense search for highly premixed mixtures makes the flame more vulnerable to small disturbances that may result in instabilities. Moreover, due to the lower flame temperature, operations can be limited by lean blow-out occurrence. In order to overcome these issues, it is very common to rely on additional pilot fuel, i.e. localized fuel injections generally devoted to enrich a specific location in the combustor in order to stabilize the reaction [35]. As an example, a series of pilot fuel injections sorrounding the main premixed flame are adopted as flame stabilizers in DACRS burners (Figure 1.2), in the so-called ELBO (Enhanced Lean Blow-Out) system.

An alternative design for low-emission burner without swirler vanes is the Alstom EV burner. It consists of two half cones shifted perpendicular to their centerlines, determining two inlet slots for air with constant width, while fuel is injected through a large number of holes along each of the slots or over the central lance. During the startup of the gas turbine, pilot fuel gas is injected over the central lance and leads to a fuel enrichment of the burner core flow, guaranteeing a broad stable range under this condition. At higher load, instead, the burner is operated in the full premix mode in order to achieve the lowest emission (Figure 1.3).

Another proposal involves fuel staging operations: the fuel flow is switched from one zone to another in order to maintain a fairly constant combustion temperature. One simple method of fuel staging is by *selective fuel injection* [36]. With this technique, at different operating conditions the fuel is supplied only to selected groups of burners. The objective of this modulation technique is to increase the temperature of the localized

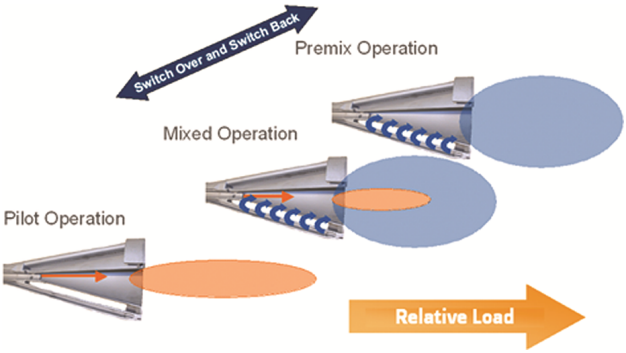

Figure 1.3: Alstom EV burner: operation modes [3].

combustion zones at low-power operation, thus extending the lean blowout limit to lower equivalence ratios [1].

Also staged combustor architectures in which combustion chamber is divided into smaller chambers with each zone controlled separately and optimally [37] have been adopted. With this technique, there is tipically a lightly loaded primary zone, which provides only the temperature rise needed at low-power conditions while acts as a pilot flame at higher power settings. An example of this architecture is the GE DLN1 combustor [38]: fuel injection occurs in each combustion zone through the primary and secondary fuel nozzles, so that the combustion system represents a two-staged architecture [39].

Tha main design differences between lean-premixed and conventional combustors equipped with diffusion flames can be highlighted considering the aero-derivative GE LM6000 combustor, depicted in Figure 1.5: a triple annular design for fuel staging is adopted to achieve an ultra-lean flame with a reduced temperature. There is no dilution and cooling injection along the liner and a shorter chamber is employed, in order to minimize the amount of cooling air. However, the combustor volume is greatly increased in order to reach higher residence times for CO and UHC oxydation.

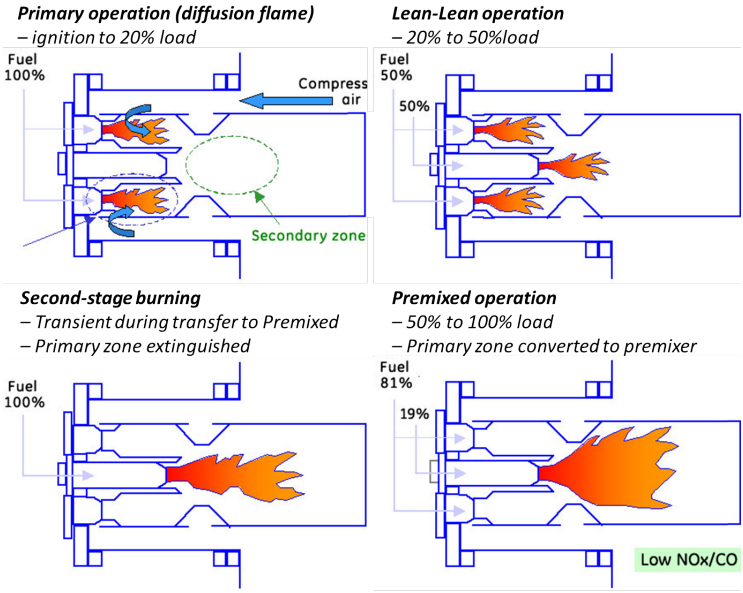

Figure 1.4: DLN1 modes of operation [4].

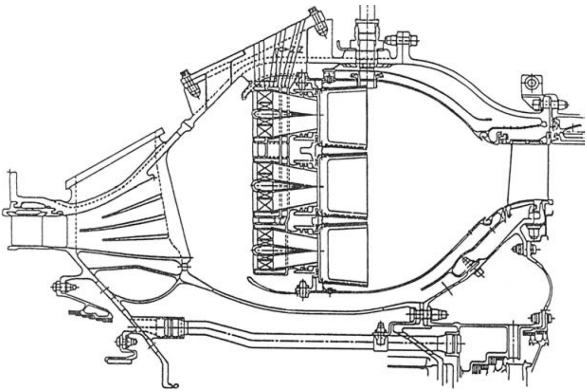

Figure 1.5: GE LM6000 Dry-Low NOx combustors [1].

1.2 Low-Emission Combustor Stability Issues

One of the primary requirements of a gas turbine combustor is that combustion must be maintained stable over a wide range of operating conditions. Lean Premixed systems operate very close to the lean flammability limit (LFL), the point at which the fuel/air ratio is too lean to support combustion, and thus can be very sensitive to combustion instabilities such as thermoacustic resonances or even global extinction (blow-off): in these conditions even a small perturbation in the equivalence ratio can lead to high heat release oscillations.

Moreover, concerning the design features of LPC systems described in the previous section, the reduced amount of available cooling air determines a reduction of the damping effect due to coolant injections, beneficial for the system stability. For these reasons, there is a great demand for models which are able to predict the dynamics of turbulent flames in LPC systems. In order to identify the conditions where the machine can operate safely, since the design phase, without the risk that the flame extinguish or thermo-acoustic instabilities occur, it is customary to study the dynamics of the flame and the stability of the combustor.

1.2.1 Combustion Instabilities

The mechanism responsible for combustion instabilities is the coupling between pressure oscillations and thermal fluctuation induced by unsteady heat release (see Figure 1.6). In gas turbines, such instabilities induce fluctuating mechanical and thermal stresses, that, depending on their amplitude, may lead to serious consequences: the flame can quench or flashback, burning part of the injection system or, if the pressure pulsation are large enough, the combustor components can be damaged and even a catastrophic failure may occurs.

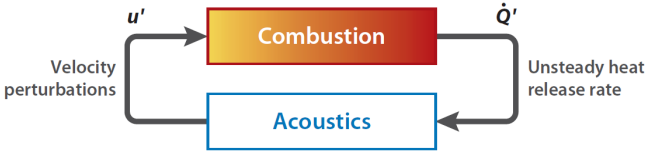

Figure 1.6: Scheme of the feedback process responsible for combustion instabilities.

Depending on the coupling between combustion and acoustics, thermo-acoustic instabilities are not a local phenomenon, influenced only by the dynamics of the flame and the sorrounding flow field, but are strongly affected by the acoustics of the chamber, and in particular by its boundary conditions.

When an instability is triggered, a perturbation in one of the flow variables is amplified and grows in time. When a saturation of the flame response occurs or the acoustic damping of the system increases, a limit cycle of pressure oscillations is reached. The first part of the process exhibits a linear trend that develops in the growth of the dominant mode, non-linear saturation and, finally, the limit cycle [40, 41]. A schematic representation of the described behaviour is depicted in Figure 1.7.

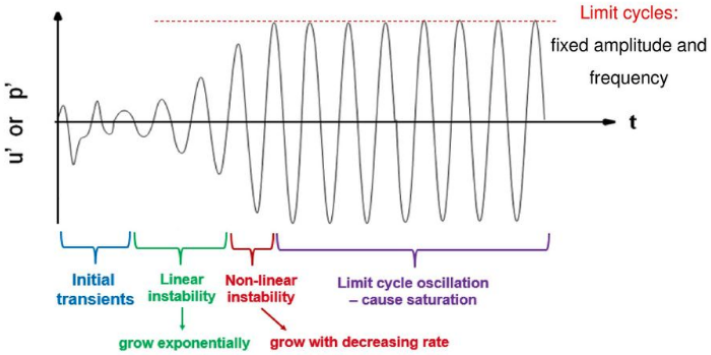

Figure 1.7: Temporal evolution of pressure oscillations for an unstable mode.

1.2.1.1 Classification of gas turbines instabilities

Several classifications have been proposed to describe combustion instabilities in gas turbine, most of them based on the oscillation frequencies, even if with different frequency boundaries [42, 43]. Following the classification proposed by Mongia et al. [42], thermo-acoustic instabilities can be grouped into three categeories:

- *Low-frequency instabilities*, that appear at frequencies lower than 100 Hz and are strongly related to blow-off phenomena. These instabilities are often referred in different ways: they are named

chugging, if related to the coupling with the feeding system during the engine transitories or *bulk* or *Helmholtz* mode of oscillation, following the classification proposed by Krebs et al. [44]. Another common way to refer to them is *rumble instabilities*, due to the sound they produce, which are typical of very lean conditions with incipient blow-off [43]. Finally, these instabilities are often referred as *cold tones*, due to the fact that the oscillation amplitude tends to increase as the flame temperature is reduced.

- *Intermediate-frequency instabilities*, or *buzz*, occurs in the range 100–1000 Hz and are usually related with the interaction between equivalence ratio and acoustic perturbations. These instabilities are also typical of longitudinal acoustic mode of the combustor and are often referred as *hot tones*: their dynamics shows an increasing amplitude of oscillation with higher flame temperature.

- *High-frequency oscillations*, or *screeching*, are observed at frequencies higher than 1000 Hz, due to the coupling between acoustic oscillations and flame kinetics. These instabilities are tipically related to azimuthal acoustic modes and result very dangerous, causing the failure of the combustor in a very short period of time.

1.2.1.2 Driving Mechanisms of Combustion Instabilities

To really understand how to model and predict combustion instabilities is of paramount importance to accurately describe:

- which are the condition for the oscillations to occur;

- which are the mechanisms for driving and substaining the growth of such oscillations.

Concerning the first term, the dependence on the coupling between heat release and acoustic oscillations was first stated by Lord Rayleigh [45], who formulated the so-called Rayleigh criterion for the onset of thermo-acoustic instability, mathematically written as:

$$\int_V \int_T p'(x,t)q'(x,t)dtdV \geq \int_V \int_T \sum_i \mathcal{L}(x,t)dtdV \tag{1.1}$$

where $q'(x,t)$, $p'(x,t)$ and $\mathcal{L}_i$ are the fluctuations of heat release and pressure and the i-th acoustic energy losses, respectively. According to Eq. 1.1, the only way to add energy to the acoustic field is to release heat when the pressure oscillation is near its maximum, otherwise the

pressure fluctuation is attenuated by the heat source. This is not a sufficient condition for the instability to occur: in fact, in order to study the stability of the system, the energy balance between the energy addition and the acoustic losses, such as the damping produced by well-established passive control devices (multi-perforated plates, Helmholtz resonators...) should be considered.

On the other side, considering the mechanisms for driving the onset of such instabilities, the dominant physical processes for driving unsteady flow oscillations in a gas turbine combustion system arise from either heat release and gasdynamic fluctuations. The former are largely related to local equivalence ratio and mass flow rate [46], the latter include acoustic motions in the chamber, evolution of large-scale coherent structures, and other flow phenomena.

In a gaseous premixed flame, velocity perturbations are identified as the typical thermoacoustic driving mechanism [47], according to the following mechanism: a perturbation in the acoustic velocity travels at the local speed of sound influencing the turbulent flow field and, once it reaches the flame, giving rise to a fluctuating heat release. Heat realease oscillations radiate acoustic waves, which, in turn, modulate the initial perturbation, closing the loop.

On the other hand, in a real combustion chamber, together with acoustic velocity fluctuations, also equivalence ratio fluctuations contribute to the dynamic response of the flame. When the fuel and/or the air supply is altered, the resulting equivalence ratio varies periodically in time [48, 49]. The mixture is transported convectively to the flame front and burnt, so that heat release fluctuations are generated which can drive the instability [50, 51]. The description of the flame response to different incoming perturbations is definitely a challenging topic for both, numerical and experimental investigations. An overview of the acoustic-flame interaction is represented in Figure 1.8.

Once understood the driving mechanism, it is important to understand how does the energy exchange occur, such as the main pathways to tranfer acoustic energy between the mean, periodic (coherent), and turbulent (random) fields. A triple decomposition technique has been proposed and applied by Huang et al. [6] to mass, momentum and energy equations in order to model the pathways through which energy is added to oscillatory motions in a turbulent reactive flow. These pathways are summarized in the scheme depicted in Figure 1.9, following the notation used in [6].

The main pathways through which energy is added to oscillatory motions are:

- From the mean flowfield ($-\overline{\rho u_i^a u_j^a} \partial \overrightarrow{u_i} / \partial x_j$), which is the primary

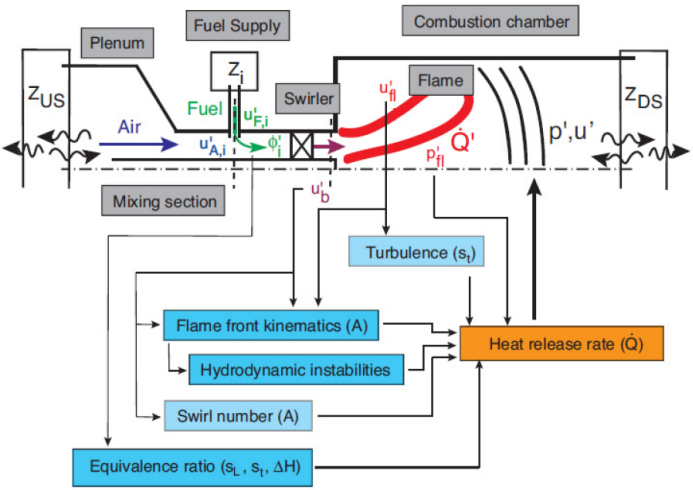

Figure 1.8: Overview of the acoustic interaction of the flame [5].

energy source for periodic motions in case of absence of combustion;

- From chemical reactions ($\frac{\gamma-1}{\gamma\overline{p}}\overline{p^a\dot{q}^a}$), which represents the main driver of instabilities. This term can assume both positive or negative values, depending on the phase difference between oscillations (see Eq. 1.1), adding or subtracting energy from the system;

- From background turbulent motion ($-(\overline{\rho u_i^t u_j^t})^a \partial\overrightarrow{u_i^a}/\partial x_j$).

1.2.2 Lean Blow-Off

The term stability is used to describe either the range of fuel/air ratios over which stable combustion can be achieved or as a measure of the maximum air velocity the system can tolerate before blow-off occurs. The stability performance of a combustor are typically determined by carrying out a series of extinction tests at constant levels of inlet air temperature and pressure [1]. After turning on the fuel and igniting the mixture, the fuel flow is gradually reduced until flame extinction occurs. The fuel and air flows at this event are registered as the weak extinction or lean blow-off point. In another procedure, the fuel flow is slowly increased until a rich extinction occurs. This process is repeated at increasing levels

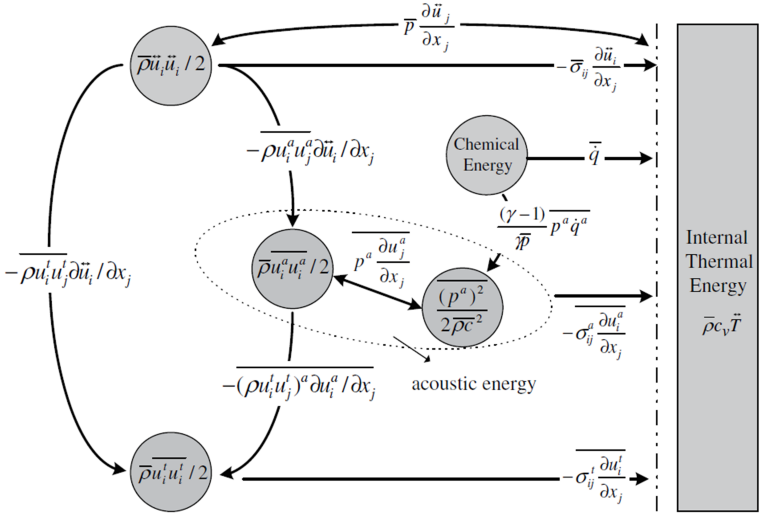

Figure 1.9: Energy exchange pathways between mean, periodic, and stochastic motion in turbulent reacting flows [6].

of air mass flow until the complete stability loop can be drawn. In Figure 1.10 the typical stability loop of a gas turbine combustor is shown for a specific value of inlet pressure.

The region of stable burning is bounded by two limits, divided by the stoichiometric fuel/air ratio. The upper branch represents the rich limit, while the lower bound is the lean limit. This two limits gradually converge increasing mass flow rate until a flow rate is reached beyond which combustion is unattainable at any fuel/air ratio. Within this stability loop, two points are specially important. They correspond to points of the limits at the air mass flows that is used to the design value of chamber reference velocity. In this work the attention is focused on the weak extinction or blow-off limit.

It is stressed that determining the LBO curve is mandatory not only to achieve the fundamental stability prerequisite, but also to low-emission combustion and fuel-efficiency, as explained above. If the lean blow-off limit is accurately identified, it is possible to obtain leaner conditions, reduce the temperature in the combustion chamber and contain the NO_X emissions. In fact, lean combustors are prone to flame quenching, a condition that can, in some cases, be related to combustion instabilities. The

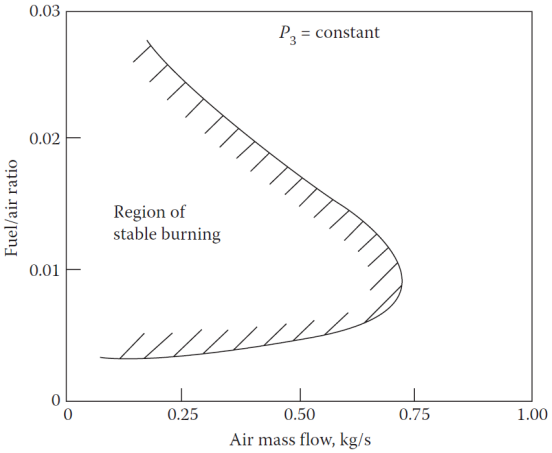

Figure 1.10: Typical combustion chamber stability loop [1].

flame can undergo rapid oscillations and eventually blow off completely. Most current gas turbines operate far from the lean limit to avoid these dynamical effects and as a result, produce unacceptable levels of NO_X. In this view, the accurate lean blow-off prediction represents a valuable instrument to reduce the pollutant emissions. This numerical study is intended to investigate the accuracy of CFD simulations as the flame approaches and blows off and to provide supplemental informations on the behaviour over the last stages of extinction that are difficult to be measured.

1.2.2.1 Lean blow-off phenomenology

The blow-off phenomenon is properly referred in literature as the extinction of flame from attached-starting conditions and it is formally different from the blow-off that refers to the extinction of flame from lifted-starting conditions [52]. Despite this distinction, in the present work the blow-off term indicates the global extinction of the flame regardless its previous anchoring position.

From the extensive literature on bluff-body flame stabilization, it is evident that the fundamental mechanisms that initiate and control blow-off are not completely understood [28] and many descriptions of blow-off and the controlling processes were proposed.

However, there is general agreement that the blow-off process is controlled by a competition between fluid mechanical and chemical kinetic processes and, for liquid fuelled combustors, eventually other time scales associated with droplet evaporation and mixing [7, 53]. This fact suggests that a key control quantities for blow-off inception should be the Damköhler number as the ratio of a flow time scale and a characteristic chemical time:

$$Da = \frac{\tau_{flow}}{\tau_{chem}} \tag{1.2}$$

Longwell et al. [54] suggested that blow-off occurs when it is not possible to balance the rate of entrainment of reactants into the recirculation zone, viewed as a well stirred reactor, and the rate of burning of these gases. Since entrainment rates scale as the ratio of the characteristic length and the bulk velocity it then follows that this criterion reduces to a Damköhler number blow-off criterion, using a chemical time that is derived from the well stirred reactor:

$$Da \geq Da_{LBO} \tag{1.3}$$

A similar idea relates to an energy balance between heat supplied by the hot recirculating flow to the fresh gases and that released by reactions [55, 56, 57]. In this view, blow-off occurs when the heat required by the combustible stream exceeds the one received from the recirculation zone. This leads to the same time scaling as above, and the resultant similar Damköhler number blow-off criterion. A different view is that the contact time between the mixture and hot gases in the shear layer must exceed a chemical ignition time [58, 59]. For example, according to Zukoski [58], ignition of the incoming fresh unburned mixture occurs in the shear layer as it mixes with combustion products from the re-circulation zone. Several studies have also proposed a flamelet based description based upon local extinction by excessive flame stretch [60, 61].

According to Shanbhogue et al. [7], this last description seems to be the one that better agrees with experimental measurements. For example, there are no evidences that the blow-off is influenced by changing fuels with different ignition time, suggesting that the time taken for the mixture to spontaneously auto ignite is not the controlling time scale. Furthermore, as noted by Driscoll [62], there is actually little evidence of the existence of distributed combustion or well stirred reactors and probably blow-off theories based on this assumption do not correctly capture the controlling processes. Instead, Driscoll [62] emphasizes that the flamelets exist under a very broad range of conditions, since modern diagnostics and computations

have often shown that reaction regions consist of highly contorted, three dimensionally oriented reaction sheets.

The extinction of flamelets can occur through the two mechanisms of heat losses and flame straining [63, 64]. Flame strain is apparently the dominant effect, with heat/radical losses only dominant near the bluff body. Flame strain occurs due to misalignment of convective and diffusive fluxes within the preheat zone [63], which occurs because of flow divergence upstream of the flame or flame curvature. Flames are only capable of withstanding certain levels of strain before extinction, though, even if the flamelet extinction occurs near blow-off, this does not immediately lead to blow-off [7]. In other words, blow-off does not occur the instant when a critical strain is exceeded at some point along the flame.

For bluff body stabilized flames Shanbhogue et al. [7] identifies the increasing occurrence of local extinctions in the flame sheet only as a first stage of blow-off phenomenon wherein flames can persist apparently indefinitely (see Figure 1.11).

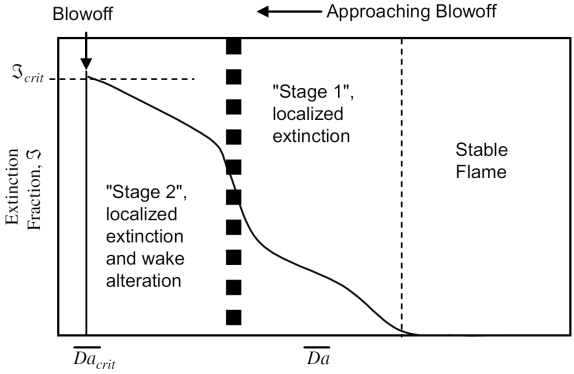

Figure 1.11: Representation of pre-blow-off processes, including local extinction and large scale wake alteration, followed by blow-off [7].

However, if a global Damköhler number is further reduced a second stage is reached. It is associated with large scale disruption of the wake fluid mechanics that leads to a change in character of the mean and fluctuating strain rate. Then blow-off occurs, well before the majority of the flame sheet is extinguished. The critical level of flamelet disruption and extinction is still unclear. Therefore a description of the blow-off phenomenon based only on local extinctions induced by strain is not really

complete.

Different stages were observed also by Muruganandam and Seitzman [65] approaching the blow-off in a swirl combustor by chemiluminescence sensors and high speed imaging. Reducing the equivalence ratio they observed the detachment of the flame from the inlet, partial extinction events, a new flame shape stabilized by the hot side walls of the combustor and the complete extinction of the flame.

In a bluff body stabilized premixed flame, Chaudhuri et al. [66] used time resolved imaging of OH* chemiluminescence at 500 Hz to show that the blow-off event occurs over a period of a few milliseconds. This was contrary to the reports in studies performed early in literature of blow-off being an abrupt phenomenon. It was found that with reduction of equivalence ratio as blow-off is approached, the flame shape and the interaction of the flame front with the shear layer increases. Near blow-off, the flame front along the shear layer is subjected to high local strain that exceed the corresponding extinction stretch rates, resulting in local flame extinction. Following shear layer extinction, fresh reactants entrain through the shear layers to react within the recirculation zone due to favourable residence time there. This flame kernel within the recirculation zone may survive for several milliseconds and can reignite the shear layers such that the entire flame is re-established temporarily. This extinction and reignition event can happen repeatedly before final blow-off which occurs when the flame kernel fails to reignite the shear layers.

Kariuki et al. [67] investigated the structure of unconfined premixed methane–air flames stabilized on an axisymmetric bluff body with high speed OH* chemiluminescence and OH-PLIF diagnostics. Approaching blow-off they observed the closing of the flame brush across the flow, the entrainment of fresh reactants from the downstream end of the RZ and fragmentation of the downstream flame parts. Very close to blow-off, reaction fronts have been observed to enter the RZ, and a shortening of the flame brush with progressive fragmentation occurs. Total blow-off occurs once the flame at the bluff body edges has been destroyed, and ignition of the shear layers is no longer possible.

As far as concern the effect of swirl on blow-off of premixed bluff body stabilized flames, limited work has been done [28]. Swirl conditions increase the size of the recirculation zone in a flow around a bluff-body, which can improve stabilization by increasing the volume of recirculating hot gases to sustain combustion. Therefore swirl can enhance the lean flame stability limits.

Zhang et al. [68] investigated the blow-off mechanism of bluff body and swirl stabilized H_2/CH_4 flames. Kariuki [28], comparing the behaviour of

premixed confined and unconfined flames, confirmed that the key stages of open flames observed by Kariuki et al. [67] were similar to the confined flames without swirl and with strong swirl approaching blow-off.

These studies showed that even with strong swirl conditions present, the key characteristics of the blow-off process for bluff body stabilized flames (localised extinctions, reactivity in RZ and progressive fragmentation) also influence the blow-off process of swirl stabilized flame.

Chapter 2

Numerical Study of Flame Dynamics and Stability

An overview about commonly used numerical methods is reported in order to explain the background and the context in which this research activity has been performed. The first part of the chapter is devoted to thermo-acoustic instabilities, whereas an in-depth on blow-off predictions is provided in the following. Theoretical notions on flames dynamics investigation and modelling exploiting important results from the literature are given, with particular focus on advanced numerical methods to be applied for the design of next generation combustors, such as weakly nonlinear thermo-acoustic analysis based on Flame Describing Function calculation and blow-off predictions by means of high fidelity numerical simulations.

2.1 Overview of numerical methods for thermo-acoustic stability analysis

The numerical study of combustion instabilities represents one of the most challenging problems in gas turbine technology development, given the combined effect of unsteady flows in complex-shaped geometries, turbulence, acoustics and chemistry [11]. A wide range of different scales have to be captured, varying from the tiny laminar flame thickness (less than 0.1 mm) to the large acoustic length (in the order of meters) and from the slow flame speed (lower than 1 ms) to the sound speed in burnt gases (higher than 600 ms). Moreover, the amount of acoustic power generated by a typical flame is generally very low (less than 10^{-8} times the thermal power), thus making very difficult its accurate prediction by

numerical tools [11].

As already stated in Chapter 1, the coupling between acoustics and flame response can be fully described by the Navier-Stokes conservation equations for mass, species, momentum and energy. This approach is computationally expensive and even impractical in the industrial framework. Thus, several methods based on different degree of simplification of the previous equations have been proposed, in both the time or frequency domain, to determine the thermo-acoustic stability of the system.

A description of the main approaches is presented, starting from the most complex and expensive, such as CFD direct simulation of the instability (Self-Excited simulations), to the methods with the highest degree of simplification, such as analytical approaches and network models. A schematic classification is reported in Figure 2.1.

However, the main idea of all the simplified tecniques, developed in three dimensions, in time or Fourier space, is always the same: flames are not directly simulated, avoiding the complexity of flow and chemistry by lumping all their effects into some form of flame response functions [11]. In the following, particular attention has been devoted to the techniques used in this work, such as FEM approach, used to solve the so-called wave equation in the frequency domain and the Self-Excited CFD simulation, whereas the other methods depicted in Figure 2.1, such as low-order and analytical methods are only briefly described.

2.1.1 Self Excited CFD Simulations

The most straightforward method to investigate the problem is the use of unsteady simulations to solve for the complete Navier-Stokes equation set for a compressible, turbulent reactive flow. This approach is often referred as *Self Excited* simulation, due to the fact that in this case the flame itself interacts with acoustic waves within the CFD simulation, without the introduction of external perturbations. Another way to define this technique is *Brute Force* approach, because of the tremendous computational cost associated and the lack of modelling [11].

Historically, this method to compute explicitly the flame dynamics, using full compressible simulations of the unforced reacting flow, was introduced around 2000 and relies on LES simulations [33] due to the fact that Direct Numerical Simulation (DNS), even if possible, is nowadays infeasible and RANS results unsuitable to model such complex interactions.

The main advantage of *Self Excited* method is the low degree of simplification of the Navier-Stokes equations that avoid any modelling of the interaction between acoustics and flame dynamics, with the associated assumption. However, this method is the most expensive and it raises

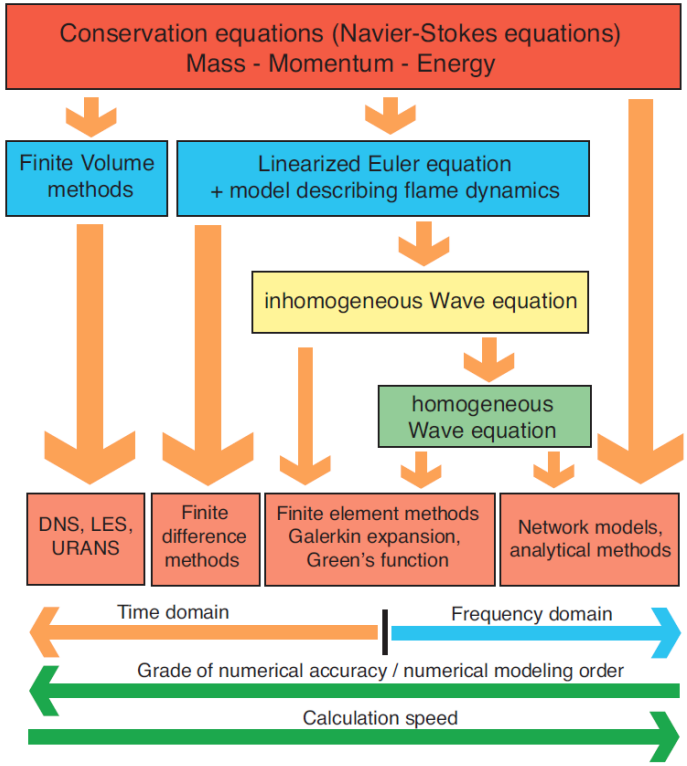

Figure 2.1: A schematic classification of numerical methods to study thermo-acoustic stability [5]

various difficulties to set the computational domain (which should be as large as possible to account for alla geometrical features of the engine) and to handle acoustic boundary conditions, chemistry, turbulence... Moreover, other drawbacks are related to spurious numerical instabilities and to the dependence on the initial condition as well as the adequate boundary conditions assignment [69].

Several applications of the LES Self-Excited technique to both lab-scale flames [70] and practical technically-premixed configurations [71] are present in literature. In Figure 2.2, some snapshots illustrating one cycle of the combustion instability in a realistic gas turbine combustion chamber configuration [8] are depicted.

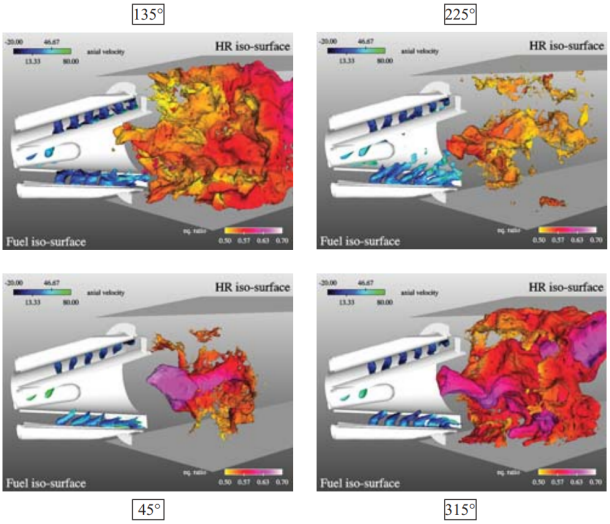

Figure 2.2: Snapshots illustrating one cycle of the combustion instability [8].

The same procedure has been applied also to full-annular combustor configurations, as done in [72, 73] where a fully compressible LES calculation of a real helicopter combustion chamber (see Figure 2.3), already studied in [74] as a single sector, has been performed. The analysis on the full-annular configuration allows to accurately predict the azimuthal modes characteristic of real configurations and to compare results, in

terms of Flame Transfer Function (FTF), of full-annular and single sector LES.

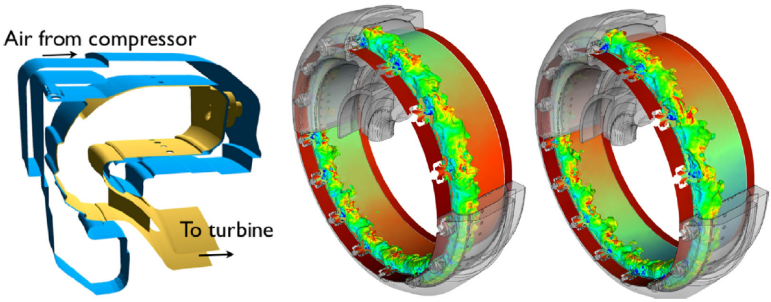

Figure 2.3: LES of the first azimuthal unstable mode in a helicopter engine [9]. Left: geometry of a single sector. Right: two snapshots of pressure on a cylinder passing through the burner axis and isosurfaces of temperature colored by axial velocity.

2.1.2 Solution of the Helmholtz equation with Finite Element Method

The set of linear transport equations for the perturbations of velocity, temperature and density can be derived by linearizing the Navier-Stokes equations [75], where the local unsteady heat release appears as a forcing term. Each variable can be decomposed in a mean term and a fluctuating one and exploiting the assumption of small perturbation the *Linearised Navier-Stokes equations* are obtained.

Further simplification can be done, negelecting viscous effects and obtaining the *Linearised Euler equations*. It is often assumed that the mean flow is at rest so that the *inhomogeneous wave equation* for the acoustic perturbations can be derived, which is called *Helmholtz equation* in the frequency domain. Several approaches exist to solve the *Helmholtz equation*, such as the *Galerkin method* and the *Green's function technique*. *Finite-Element Method (FEM)* is usually employed to deal with the geometrical details of the combustor, reproducing the complete 3D problem and allowing a direct solution of the modal coupling between the different types of modes.

However, specific models are required to account for additional effects, like pressure losses and acoustic damping in the system and the fluctuating

heat release term. Furthermore, in some regions of gas turbine combustors, such as the burner region, the Mach number is not negligible and assuming the mean flow at rest may leads to errors in the stability prediction of principal modes [76].

Several applications of the FEM approach to perform linear thermo-acoustic stability analysis can be found in literature: lab-scale combustors as well as full-annular combustion chambers for gas turbine applications have been investigated with this method. A comparison between numerical results and analytical solutions can be found for simple annular configurations, like the ones studied in [77]: a significative impact of the acoustic boundary condition on the calculated eigenfrequencies has been retrieved.

A CFD-FEM coupled approach to study thermo-acoustic stability, exploiting RANS and LES data to provide the conditions for the FEM code, has been proposed and validated by Nicoud et al. [78], investigating the stability of an industrial annular combustor.

Heat release models have been exploited instead by Camporeale et al. [79] to study both simple geometries, where analytical solution were available [80], and simplified annular combustion chambers. In [81, 82] a spatially distributed flame approach has been proposed, exploiting the results of RANS simulations and investigating the impact of flame shape modelling.

A full-annular combustor equipped with a lean injection system, shown in Figure 2.4, has been studied by Andreini et al. [10, 83, 84], exploiting a specific modelling for the acoustic damping provided by multi-perforated liners and investigating the effects of different expressions for the unsteady heat release term.

Nonlinear analysis can also be performed coupling the FEM solver with nonlinear flame reponse functions, with the aim of predict the amplitude and stability of limit cycle oscillations. Suitable predictions of unstable frequencies and amplitudes exploiting different approaches can be found for example in [14, 32, 85, 86, 87]. A more detailed overview of such nonlinear calculations will be provided in Chapter 3.

2.1.3 Low-order network models

Low-order network models, or *acoustic network model*, are the only one employed until the 2000s to study thermo-acoustics in gas turbines. Such methods consist of dividing a complex system, such as a combustor, into a network of simple, homogeneous, 1D elements where the acoustic problem

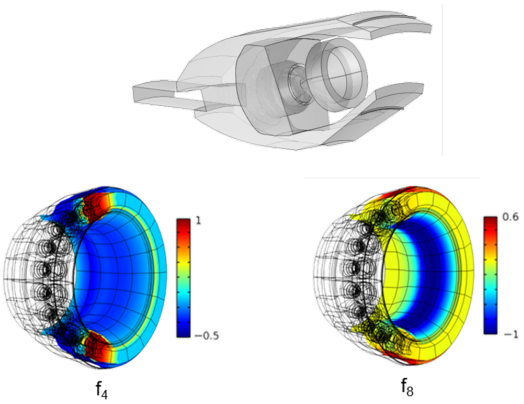

Figure 2.4: Sector of the full-annular combustor and results from FEM analysis obtained by Andreini et al. in [10].

can be described by means of a transfer matrix and solved analytically [76].

The main drawback is that the geometrical details of the combustor cannot be accounted for due to the (quasi)-1D assumption. Nowadays, low-order network models represent a useful design tool and allow a fast and robust estimation of the thermo-acoustic behavior of combustion systems. To name a few, the effects of entropy waves have been investigated exploiting this approach by Polifke at al. [88], while acoustic dampers have been extensively studied in [89, 90]. Complex configuration can be studied, like the one showed in Figure 2.5, and azimuthal modes can be retrieved with a proper chamber modelling [11].

The simplified approaches presented herein need for a proper modelling of flame response, representing the heat release fluctuations to be coupled with the acoustics of the system. As already discussed in the previous sections, several approaches can be numerically used to obtain this term, Both linear and nonlinear flame modelling can be used, ranging from analytical formulations or CFD-based flame responses and will be presented in the following sections.

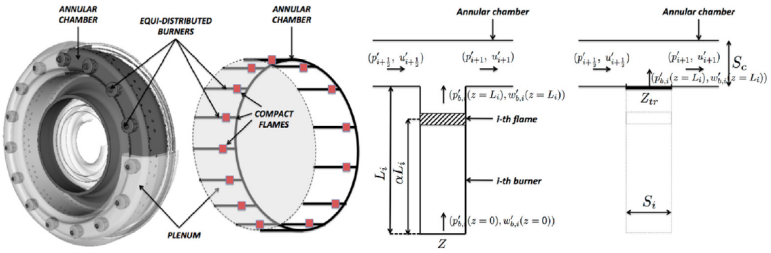

Figure 2.5: Left: modelling a full-annular combustor by a network of 1D elements. Right: Burner modelling [11].

2.2 Flame Modelling

The frequency response of a flame to small amplitude perturbations can be represented by its Flame Transfer Function $FTF(\omega)$, defined usually with respect to acoustic fluctuations at the burner exit as:

$$FTF(\omega) = \frac{\dot{Q}'(\omega)/\overline{\dot{Q}}}{u'(\omega)/\overline{u}} \tag{2.1}$$

where $\dot{Q}'$ and u' represent respectively the heat release and velocity fluctuations, whereas $\overline{\dot{Q}}$ and $\overline{u}$ the corresponding mean values. According to the above definition, in the linear regime, the system can be modelled as a Single-Input Single-Output system (SISO), such as a block-box characterized by velocity fluctuations upstream the flame, usually recorded at the burner outlet, as input and the heat release rate as output (see Figure 2.6).

Figure 2.6: Scheme of the SISO model of a perfectly premixed flame.

Assuming a harmonic behaviour, the fluctuations of input and output quantities can be expressed in terms of amplitude and phase as:

$$\dot{Q}'(\omega) = \hat{Q}(\omega)e^{i(\omega t+\phi_Q)}$$
$$u'(\omega) = \hat{u}(\omega)e^{i(\omega t+\phi_u)} \tag{2.2}$$

Following this assumption the FTF becomes:

$$FTF(\omega) = F\hat{T}Fe^{i\phi_{FTF}} = \frac{\hat{Q}(\omega)}{\hat{u}(\omega)}e^{i[\phi_Q-\phi_u]} \tag{2.3}$$

Due to the fact that the heat release fluctuations are considered all over the combustion chamber, the FTF can be seen as a global term, allowing the simplified description presented in the previous sections.

Ad already stated in Chapter , it is important to deal with nonlinear effects on flame response, in order to accurately predict not only the onset of combustion instabilities but also the behaviour of the system. In fact, knowing the response of the flame when submitted to perturbations covering a range of amplitudes allows to calculate the limit cycle amplitude of pressure oscillations in case of unstable system.

The change of the flame response with the incoming perturbation level can be modelled generalizing the Flame Transfer Function concept and defining a Flame Describing Function (FDF) [32] as:

$$FDF\left(\omega, |u'|\right) = \frac{\dot{Q}'\left(\omega, |u'|\right)/\overline{\dot{Q}}}{u'\left(\omega, |u'|\right)/\overline{u}} \tag{2.4}$$

This nonlinear dependance of the FDF with respect to the amplitude of perturbations, approximated as harmonic solutions, leads in many cases to the accurate description of the nonlinear behaviour observed in practice [91]. However, the FDF analysis assumes that the dynamics of a given thermoacoustic mode is decoupled from the dynamics of the others, which has been demostrated to be not always true [92]: the nonlinear coupling between the modes can lead to significant changes in the behaviour of a thermoacoustic system with respect to the one predicted by the FDF.

2.2.1 Flame Transfer Function calculation

The experimental determination of FTFs can be difficult, very expensive and requires very careful experimental work (especially in the presence of turbulent flow or combustion), sophisticated post-processing and long test runs [93, 94]. Otherwise, analytical models have been proposed which are derived under simplifying assumptions or, alternatively,

numerical methods can be used in a variety of approaches. A brief review of these numerical and analytical methods to obtain a Flame Transfer Function is presented herein.

One global characteristic of the Flame Transfer Function is a time delay τ in the heat release response to an excitation. The flame reacts at a time t to a perturbation at the burner occurred at a time $t - \tau$.

A general form of Flame Transfer Function is given in the frequency domain in terms of amplitude $A(\omega)$, and phase $\phi(\omega)$. The former relates the intensity of the heat release response relatively to the perturbation which caused it, while the latter determines the time lag of the flame response.

$$F(\omega) = A(\omega)e^{i\phi(\omega)} \tag{2.5}$$

Generally, the time delay has a different behaviour depending on the mechanism responsible for the flame perturbation: an acoustic oscillation travels at the speed of sound whereas mixture or swirl number perturbations within the burner are convected by the flow into the flame, showing a much slower characteristic time. The most common analytical formulation for the Flame Transfer Function is the $n - \tau$ model, proposed by Crocco and Chen [95], in which a constant time delay representative of the all physical processes involved is assumed:

$$FTF(\omega) = ne^{-i\omega\tau} \tag{2.6}$$

However, such model is not able to describe the experimentally observed low-pass filter behaviour of the flame, due to the constant gain assumed. Several alternative models have been proposed to overcome this issue (see for example [96, 97, 98, 99]). Other mechanisms affecting the flame response can be included, such as swirl number oscillations [100] or fluctuations of droplet diameter caused by the fluctuation of air velocity in liquid-fuelled flames [101].

Other Flame Transfer Function formulations for specific applications, such as liquid fuelled flames, can be found in [102, 103], where the heat release rate is directly proportional to droplet evaporation rate, or in [101], in which a relation between droplet diameter fluctuations and velocity fluctuations at the injection plane is proposed.

The effects of different analytical formulations on linear stability analysis of a lean-burn aero-engine combustor developed by Avio Aero GE have been investigated in [12]: in Figures 2.7 and 2.8 the FTFs calculated exploiting the n-τ model (FTF-1) and the models developed in [96] (FTF-2) and in [101] (FTF-3) are depicted, together with the

obtained results.

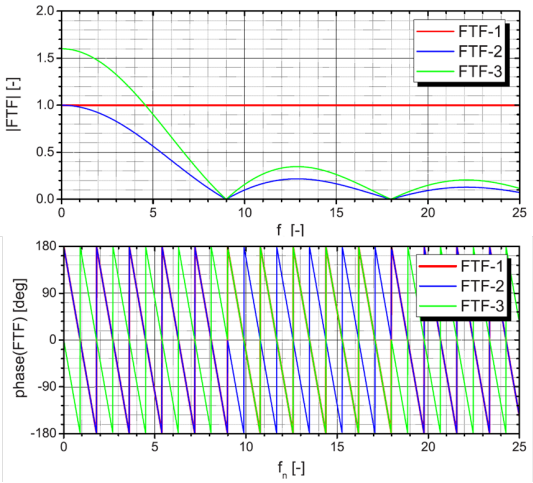

Figure 2.7: Comparison between the FTFs analysed in [12].

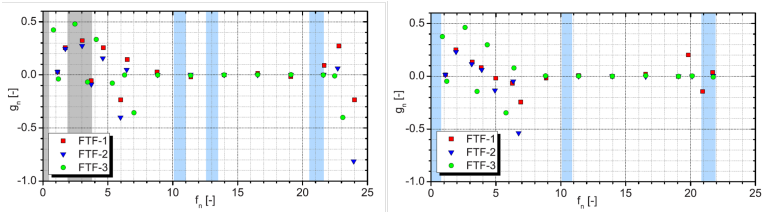

(a) Case A. (b) Case B.

Figure 2.8: Effect of different FTF formulations on predicted modes stability [12].

To describe both the Flame Transfer Function amplitude and the time lag as a function of the frequency, many approaches exploit unsteady CFD to analyse the dynamic response of the flame to a forcing of the acoustic variables. The response at a single frequency can be calculated exciting the transient CFD simulation with a harmonic forcing at the frequency of interest, in the same way as it is done in experiments: both lab-scale flames [104] and industrial configurations [105, 106, 107, 108] have been

investigated in such a way.

However, the approach results expensive if the FTF needs to be calculated over a wide range of frequencies, due to the fact that a different transient CFD simulation has to be performed for each frequency of interest.

An alternative and attractive way to calculate the FTF is to exploit System Identification (SI) techniques coupled with unsteady CFD simulations: a broadband signal is imposed as forcing for the unsteady CFD simulations, time series data are extracted and the obtained signal are post-processed with SI in order to calculate the Unit Impulse Response [109]. The computed UIR is then Z-transformed to obtain the FTF.

2.2.1.1 Flame response calculation by means of CFD/SI

Before being applied to thermo-acoustics, CFD/SI has been successfully exploited to non-reactive contexts, to calculate the acoustic transfer matrix to be implemented into acoustic networks [105, 110, 111]. The first applications of CFD/SI to calculate the FTF can be found in [13, 94] where a turbulent premixed swirled flame experimentally studied in [112] has been investigated with both URANS and LES approaches (see Figure 2.9). On the same burner, the impact on flame dynamics of fluctuations of swirl number and heat losses at the combustor walls have been studied, finding a strong impact on flame response.

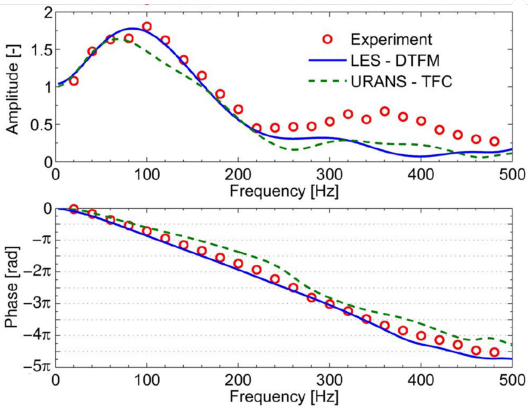

Figure 2.9: Comparison between experimental and numerical FTFs from LES and RANS simulations [13].

Furthermore, the CFD-SI procedure has been extended to model practical premix flames with a Multiple-Input Single Output (MISO) model structure, including the effects of equivalence ratio fluctuations by Huber and Polifke [113, 114]: the identification results more difficult, due to the presence of partly correlated input signals [115] but the flame modelling is more representative than a simple SISO system.

In the industrial framework, applications of the CFD/SI technique can be found in [116] for an Alstom combustor, where a SISO modelling has been applied to a practical flame, and in [106] for a Siemens/Ansaldo industrial gas turbine, showing the improvements that can be obtained with respect to simplified FTF formulations.

In [117], the CFD/SI procedure has been applied to a lean premixed swirl-stabilized combustor, experimentally studied at Technische Universität of Munich in order to validate it and perform some sensitivities to the main parameter. After assessing the whole methodology, two applications at practical configurations are presented in [21] and [118], where a technically-premixed lean methane flame, representative of a heavy-duty gas turbine combustor and a liquid fuel combustor for aero-engine applications are studied, respectively.

2.2.2 Flame Describing Function calculation

The FDF may be obtained with both experiment and numerical simulation by forcing harmonically over a range of frequencies and amplitudes or by means of analytical formulation [31, 119].

Currently, most works on Flame Describing Functions has been carried out with experimental methods and therefore the reliable calculation of FDF by numerical tools, especially Computational Fluid Dynamics (CFD), is of high technical relevance in order to improve the thermo-acoustic characterization of gas turbine combustors.

The numerical simulation of such systems involves the interaction of many complex physical processes that strongly influence the nonlinear behaviour of the flame, such as turbulent mixing and chemical reactions. Even if URANS (Unsteady Reynolds-averaged Navier–Stokes equations) approaches have been used to investigate the nonlinear flame dynamics in simple configurations [120], to accurately compute the FDF in highly turbulent flows, a LES modelling is needed and the effects of flame stretch and heat loss into turbulence combustion models should be included [20].

Successful calculations of FDF for partially premixed and premixed configurations have been performed in [121] for a swirl-stabilized flame and in [122] for a bluff-body flame. When the FDF is coupled with an acoustic network solver or a Helmholtz solver, it can be used to

study the amplitude and stability of limit cycle oscillations, approximated as harmonic solutions [32], obtaining suitable predictions of unstable frequencies and amplitudes of limit cycles. Such a model allows to predict also nonlinear instabilities ("subcritical bifurcations" [87]) and hysteresis, but neglects non-normal and nonlinear modal coupling, assuming that higher harmonics are not important due to the low-pass behaviour of the flame.

The main advantage of such decoupled approach is that, as for FTF, once the flame behaviour is provided, the stability of any system containing the flame can be predicted, assuming that the flame is not significantly changed.

Thus, the FDF results to be a versatile tool for modelling nonlinear effects and has been employed in several different applications: Noiray et al. [32] studied a matrix of multiple conical premixed flames, while a ducted flame and a flame holder have been investigated in [98] and [31] respectively. Other applications of the FDF concerns a conical premixed flame [123], a bluff-body stabilized flame [124] and turbulent swirled flames [86, 125, 126].

Finally, Laera et al. [14] used a Distributed Flame Describing Function approach to study an annular combustor with multiple matrix burners, exploiting the experimental flame response (see Figure 2.10) combined with a Helmholtz solver. A so-called harmonic balance nonlinear stability analysis has been performed with the aim of determine the trajectory of the system dynamics in a frequency-growth rate plane (Figure 2.11) . The spinning self-sustained modes observed experimentally have been identified and several sensitivities have been performed to study the flame modelling within the Helmholtz solver. The work highligthed the importance of a distributed and weighted heat release source term.

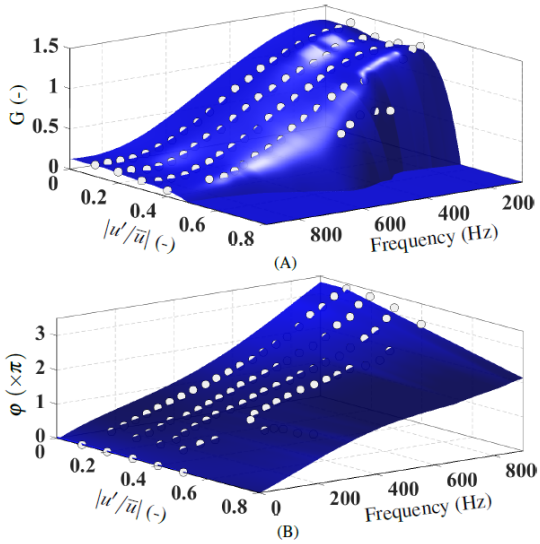

Figure 2.10: Gain (A) and phase (B) of the FDF interpolated from experimental data (white dots) [14]

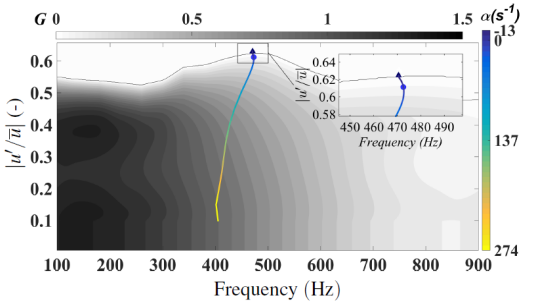

Figure 2.11: Trajectory of the combustor colored with GR and projected over the contour plot of the gain of the FDF. The zoom frame highlights the limit cycle condition for a vanishing damping rate (triangular mark) and for a finite damping rate (circular mark). [14]

2.3 Overview of numerical methods for Blow-off prediction

Despite nowadays CFD methods are used extensively within the industrial design processes, lean blow-off curves are typically determined through an expensive and time consuming process of prototype hardware fabrication and testing [127]. In fact, the experimental approach is the common way to assess the stability of combustion devices by determining the extinction points corresponding to the lean operating limit.

Following this approach, the combustor is considered as a black-box and no information is provided to improve the design. As a result, the obtained limits can be applied only to a specific configuration and are not suitable to be really integrated into the design practices.

Designers, instead, requires spatially resolved information on the flame topology, in order to locally improve the stability of the combustion process and allow to burn leaner mixtures. Due to the fact that LBO limit is dependent on a large number of different parameters, from the geometry of combustors and burners to many operating conditions, real-time monitoring for each of them requires a complicated and expensive diagnostic system.

Within the design phases, the availability of a detailed model to predict blow-off inception would reduce project iterations and avoid many expensive tests on prototypes. Many empirical correlations were proposed to estimate the blow-off inception [128, 129, 130]: a comprensive review can be found in [7]. Beyond their accuracy, every correlation is restricted to specific combustor configurations and strict validity ranges and provides only global informations, due to the fact that is based on global parameters such as the blockage ratio, the flow velocities, the pressure, the preheat temperature, etc. No detailed information on what really happens inside the combustor is given to the designers. Furthermore, due to the adoption of different combustor architectures, as stated in Chapter 1, this approach has limited applicability for modern low-emission gas turbine combustors [131].

In contrast to the correlative approach, numerical computations offer the highest possible flexibility in terms of geometry parameters and operating conditions. However, the numerical simulation of such a complex phenomenon like blow-off represents a real challenge for modellers. Moreover, these studies allow to identify the local flame behaviour before extinction and the precursor events such as fluctuations in the heat release rate or changes in the flame shape and are fundamental to gain insight into the blow-off phenomenology.

As for experiments, the direct numerical simulation of the whole stability curve requires to simulate many test points within the engine operating range (*Direct blow-off simulation*). This operation can be computationally very expensive, so during the last decades an alternative method, often refferred as *Hybrid approach* was developed. These two different methods for blow-off prediction are explained in the following sections.

2.3.1 Hybrid approach

The idea behind the hybrid modelling is the separation between the fluid dynamics and the chemical processes of combustion, due to the different time scales involved. In fact, the method decouples the reaction kinetics from the fluid flow solution, allowing the designers to assess a wide range of operating conditions in a cost effective manner [131]. Within the hybrid framework, at first an isothermal CFD solution at a specific operating condition is performed. Then, the calculated flow-field is post-processed to represent the fluid dynamics by means of a connected network of idealized reactors and the chemistry is solved over the range of desired operating conditions approaching blow-off [132].

Although this approach reduces the time requested by calculations, several fundamental processes are neglected: the turbulence-chemistry interactions on reaction rates are implicitly ignored since the chemistry is solved on a "frozen" flow field. Moreover the stationary flow does not change varying operating conditions and dynamic phenomena near LBO can neither be captured nor influence the solution. These simplifications limit considerably the accuracy in the prediction of the unsteady local extinctions due to turbulent fluctuations which trigger the blow-off event.

2.3.2 Direct blow-off simulation

The most straightforward approach involves the direct simulation of the flame with reactive CFD calculations. The simulations should be repeated several times with progressively leaner mixtures until the combustor LBO limit is reached.

Direct numerical methods rely on the full simulation of the turbulent reacting flow-field in the combustion chamber. This approach is computationally demanding or even prohibitive since detailed modelling of turbulence and chemistry with their interactions is essential. In fact, the numerical LBO prediction can be accurate only with the correct computation of complex phenomena such as the mixing processes, the chemical

reaction rates and combustion heat losses. Specifically, the blow-off process is always accompanied by local extinctions and re-ignitions along the flame front, particularly in the recirculation zones [16]. Therefore the modelling should account for the strong turbulence-chemistry coupling that characterizes the typical gas turbine combustors flames, especially near lean limit.

Simulation of flames in such regimes with detailed chemistry is generally too expensive and cannot really represent a useful tool for industrial design processes. Many combustion models have been developed to overcome these difficulties, usually based on tabulated flame solutions that are mapped on the flow field.

In addiction, due to transient nature of the combustor blow-off phenomena, direct numerical methods for the prediction of LBO limits rely on unsteady calculations. In fact, the typical precursor events of blow-off are localized extinctions and severe fluctuations of the flame, which would be impossible to capture with steady simulation. For these reasons, the typical numerical approaches to study the blow-off are:

- **Unsteady Reynolds-Averaged Navier-Stokes (URANS)**, where all the turbulent scales and mean reaction rates are modelled. Missing the physics of small-scale structures, the turbulent mixing is entirely governed by turbulence model and this influence the transport processes that feed the combustion. Moreover, only the temporal variation of mean quantities can be accounted for, so the highly transient behaviour of the flame near LBO cannot be reproduced. The main advantage of this approach is the reduced computational demand, which allows to investigate many operating conditions near lean limit without an excessive time cost. An example of LBO direct simulation by means of URANS can be found in [133];

- **Large Eddy Simulation (LES)**, which is an inherently unsteady approach and results the favourite tool to study transient phenomena like lean blow-off process. The resolution of large turbulent eddies allows a more accurate calculation of the main mixing mechanisms and provides a consistent base for the combustion simulation. Despite the combustion still requires modelling, flame prediction with LES presents significant improvements with respect to simpler approaches. In the perspective of accurately predict blow-off, local interactions between turbulent fluctuations and flame are fundamental since induce local extinctions and change the flame structure. The proper computation of these phenomena is possible only with a LES approach in practical applications. These advantages, however,

require high computing resources and this complicates the introduction into the design cycle, which must justify the high cost. In addiction to the prediction of BO limit, the high spatial and time accuracy of LES simulation allows the researchers to investigate with an extraordinary detail on the flame dynamics approaching blow-off. Such possibility represents a great advantage with respect to experimental diagnostics, that are often invasive or limited in resolution.

During the last decades LES has been increasingly used due to the continuous increase of computational power. However, since the BO is a stochastic process, relatively few attempts have been made to evaluate the blow-off behaviour through Large Eddy Simulation.

Esclapez et al. [15] investigated the sensitivity of LBO to fuel properties for a spray flame in a realistic combustor with a pressure-swirl atomizer and effusion plates. They simulated the blow-off transient for two fuels using the flamelet/progress variable approach [134], observing negligible differences between them, in accordance with experiments. The blow-off was induced by a progressive fuel depletion over three Flow-Through-Times (FTT) in the primary zone of the combustor. The resulting overall equivalence ratio was linearly decreased from $\phi = 0.1$ to $\phi = 0.07$, a level below the experimental limit to ensure that the BO was triggered. They found that the reduction of the averaged temperature in the IRZ slows the droplet heating and delays the evaporation, reducing in turn the gaseous fuel availability. During the blow-off they analysed the temporal evolution of four key indicators, i.e. the total evaporation rate, the heat release integral, the mean temperature in the IRZ and the flame root distance from the pressure-swirl injector nozzle, as reported in Figure 2.12.

Initially, the combustor response to the change in the injection rate exhibited an initial delay, corresponding to the residence time in the primary zone, then it was observed a linear decrease of the evaporation rate, heat release and mean IRZ temperature while the flame root was progressively shifted downstream toward the primary zone. Finally they registered large variations of the evaporation and heat release integral which they associated with recoveries of the flame in the primary zone. The flame blow-off was identified after 27 ms of simulated time and it was preceded by an atypical flame shape, with fronts distributed throughout the primary zone.

Zubrilin et al. [133] studied the swirled premixed flame stabilization in a modular swirled burner with a conical diffuser. URANS simulations were carried out with the Flamelet Generated Manifold model and different closures for the progress variable source term, different swirl intensities

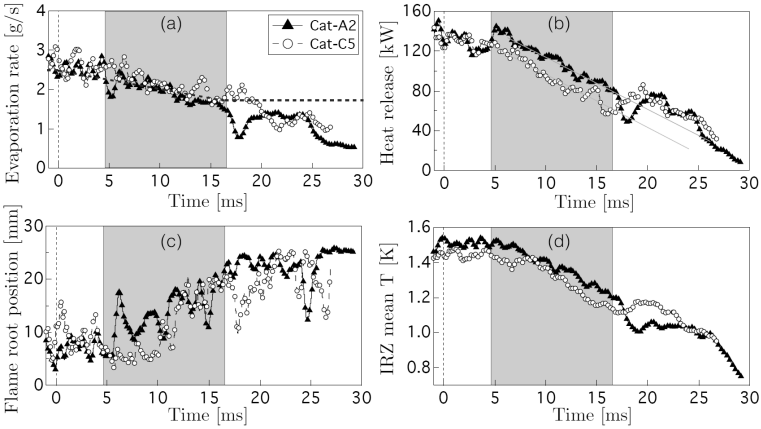

Figure 2.12: Temporal evolution of key quantities during blow-off transient for two different fuels [15].

and fuels were investigated. As key parameter to identify the blow-off event, they monitored the combustor outlet temperature, which exhibited an abrupt decreasing. Their results showed that increasing significantly the number of mesh elements, the lean limit for FR / TFC model results higher if compared to other models. On coarse grids the TFC model predicted LBO with leaner mixture than the other models, while for small elements the TFC and FR models were roughly equivalent. They also observed that increasing the swirl intensity, the amount of fresh air entering the recirculation zone from the atmosphere also increased, with a positive effect on the flame stabilization equivalence ratio range. Finally, it was noticed that using propane as fuel could improve the weak extinction resistance with respect to methane.

A systematic attempt to predict LBO by means of LES has been done by Zhang et al. [135], who investigated a swirl-stabilized non-premixed methane flame using the Conditional Moment Closure with detailed chemistry. They simulated the flame over a wide range of conditions and predicted the entire blow-off limit with good accuracy in a range of fuel flow rates within 25% of the experimental value (Figure 2.13). They investigated in detail the local extinction phenomena and observed a gradual decrement of the total heat release and the appearance of high frequency fluctuations of the conditionally filtered stoichiometric scalar dissipation rate, which resulted in an increased fraction of local extinction

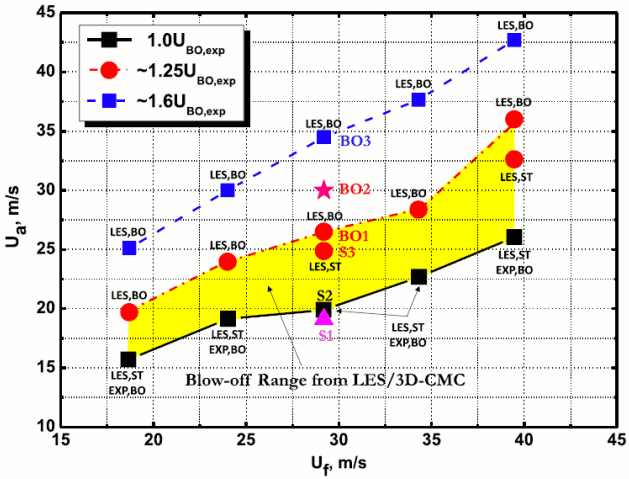

Figure 2.13: Blow-off curve calculation by means of LES-CMC [16].

over the stoichiometric mixture fraction isosurfaces.

A recent LBO prediction by means of LES with an automatic meshing CFD solver can be found in [17, 136]. A liquid-fuelled flame has been studied, investigating different fuel characteristics. The authors exploit a local grid refinement carried out using Adaptive Mesh Refinement (AMR) techniques based on local scalar gradients: this approach aims at overcoming all the problems linked to the use of a static grid by introducing a dynamic mesh where elements size varies during the simulation, as can be seen in Figure 2.14. Firstly, an orthogonal hexahedral base grid is automatically generated, based on a few user-defined control parameters and fixed embedding is possible in the regions of interest, for instance inside the nozzle or close to the walls. During the simulation, the mesh is automatically refined in the regions where the second derivative of user defined variables is higher than a certain threshold. Such technique allows a strong reduction of the computational cost while keeping a high-fidelity prediction of the main flow quantities.

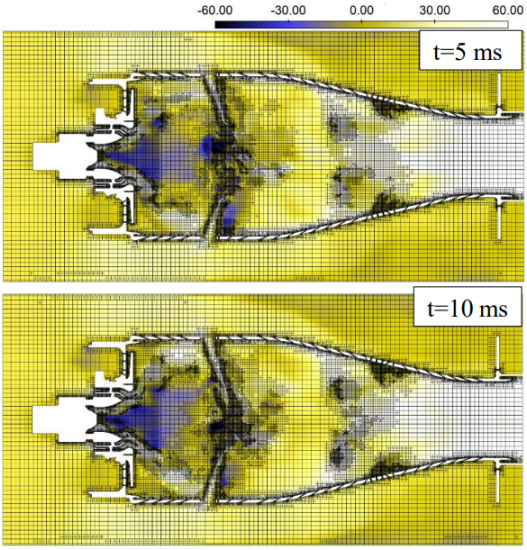

Figure 2.14: Computational grid used for LBO simulations with AMR at different simulated time [17]. Contours are colored with axial velocity (m/s)

Chapter 3

Numerical Methods for Blow-Off and Combustion Instabilities Predictions

In this chapter the numerical methods and the assumptions used for the investigation of the flame dynamics and stability, the data post processing and the thermo-acoustic analysis are presented. In the first part of the chapter the numerical models and the general practices used in the CFD computations for both, blow off and thermo-acoustic instability predictions, are described. A particular focus is devoted to the implementation of an extended model of Tubulent Flame Closure to account for flame stretch and heat loss effects in the FGM framework. Following, the basic of System Identification theory and the different flame modelling techniques devoted to calculate the flame response are discussed. In the final part of the chapter, the main modelling strategies for thermo-acoustic stability analysis are presented. In particular, the theory of weakly non-linear, frequency-based analysis is discussed and an efficient computation method for industrial annular combustion chambers based on Bloch-Wave Theory is presented.

3.1 Transient CFD simulation of reacting flows

The flow field within the typical gas turbine combustor is highly turbulent. The equations that govern the evolution of turbulent flows are the Navier-Stokes equations. In principle it is possible to resolve them numerically through iterative algorithms that are performed in super-

computer. This is commonly referred as Direct Numerical Simulation or DNS. This approach requires enormous amount of computing power and it is not really suitable for the complex flows that are studied in engineering applications.

In fact, to solve completely the Navier-Stokes equations it is necessary to take into account all the scales of time and space. However, in case of turbulent flows the solution contains scales of very different size and it is extremely onerous to resolve all the spectrum of turbulent fluctuations. In order to reduce the computational cost and make the calculations feasible for industrial applications, commonly the attention is focused over particular scales, so it is avoided the need to solve the dynamics of all these scales directly. This means that the full Navier-Stokes equations are manipulated to represent only the scales that are wanted in the solution, leaving the others out.

In general there are two main unsteady approaches to decrease the computational effort by incorporating some additional modelling: Large Eddy Simulation (LES) and Unsteady Reynolds averaged Navier-Stokes (URANS) equations, depending respectively on a complete or partial modelling of the spectrum of turbulent fluctuations. As reported in Chapter 2, Scale-Resolving Simulations such as LES are achieving a growing attention and they have been already widely applied for the simulation of practical flames [33].

3.1.1 Large Eddy Simulation in Flame Dynamics

The regular increase in computing power and the availability of dedicated numerical schemes and combustion models allow Large Eddy Simulation to be applied to real industrial flames. LES codes and models have appeared to be well suited to capture the dynamics of complex flames, allowing an accurate description of velocity and temperature profiles and unsteady phenomena, such as PVC, flashback, combustion instabilities and blowoff [33].

3.1.1.1 Turbulence model

As for RANS, several models for subgrid turbulence exists and are based on the definition of a subgrid turbulent viscosity with the Boussinesq hypothesis. The main function of the subgrid turbulence model is to mimic the drain of energy associated with the energy cascade, i.e., to remove energy from resolved large-scale motions [7]. In this work the Dynamic Smagorinsky-Lilly model [137] is used to model the subgrid eddy viscosity. The basic formulation for the eddy viscosity has the same form

of the standard Smagorinsky-Lilly model, where it is defined in function of the resolved stress tensor and a subgrid mixing length depending on the Smagorinsky constant and filter length. While in standard model this constant is fixed, the Dynamic model takes advantage of a second filter with dimension twice the real filter based on the cell length that provide a second resolved flow field. The difference between the two resolved flow field is related to the scales of dimension between the two filter length and is used to obtain information on the Smagorinsky constant.

3.1.1.2 Combustion model

Despite Large Eddy Simulation solves numerically the scales bigger than the filter length, the scales of combustion reaction are typically unresolved since are smaller than cell dimension and require a modelling. Furthermore, to avoid the solution of a transport equation for every single chemical species involved in the reaction, a common approach is to reduce the number of scalars with quantities defined appositely. The combustion model fulfil this two needs. As for the turbulence, many combustion models have been developed.

In engineering applications for gas turbine framework, the Flamelet Generated Manifold is very appreciated for its good accuracy in a wide range of applications despite the low computational cost. This is the model used in this work and is described in detail below.

Pierce and Moin [134] originally proposed a reduction technique that intended to substitute the widely-used scalar dissipation rate as a flamelet parameter in favour of a reaction progress variable.

The model was then extended, leading to the present Flamelet Generated Manifold or FGM model. The main idea underlying the FGM combustion model is that the thermochemical states in a turbulent flame can be locally assumed similar to the ones in a laminar flamelet. Of course this idea is not always true since it is made the hypothesis that the turbulence does not destroy the inner laminar structure of flame. With reference to regime of combustion it can be stated that this is true up to the limit of Karlovitz number (squared ratio of laminar flame thickness and Kolmogorov length scale) $Ka = (\delta_l^0/L_k)^2 < 100$ that is the upper limit of thin reaction zone (Figure 3.1). In this regime the preheat zone of flame front is penetrated by smaller vortices, but not the inner reaction zone [138], preserving its structure. If also the integral time scale τ_t is bigger than a characteristic chemical time τ_c, i.e. Damköhler number $Da = \tau_t/\tau_c > 1$, that is also the typical operating regime of real gas turbines and it is correct to apply a low-dimensional flamelet manifold to the turbulent flow field [18].

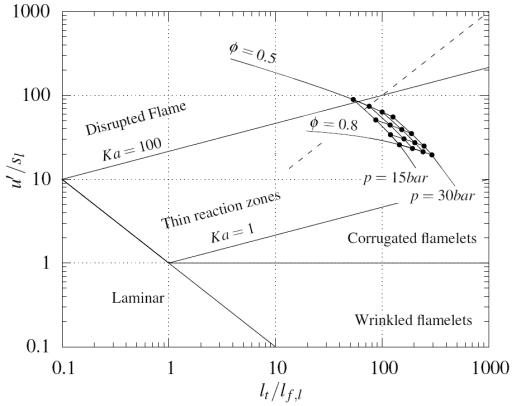

Figure 3.1: Typical operating range of gas turbines on combustion regimes diagram [18]. The dotted line represents $Da = 1$.

In fact, the FGM method involves tabulating a manifold of species and temperature obtained from either premixed or diffusion flamelet calculation as a function of some control variables. It is very important to stress that the model does not make any assumption on flame structure and it can theoretically be used to simulate ignition, slow chemistry, and quenching effects far away from the equilibrium. One of the main advantages of the FGM method allows an advanced reduction of the equations needed to model a reaction, saving a lot of computational effort.

As far as concern the FGM model as implemented in ANSYS Fluent [139], the independent control variables used are the scalars of mixture fraction and progress variable. While the mixture fraction (z) describes the mixing of two streams tracing the atomic mass fraction of single elements, conserved through a classic reaction, the progress variable (c) quantifies the progress of the reaction to equilibrium conditions. With this definition, the model is suitable for partially-premixed, premixed or diffusion flames. The progress variable is typically defined as an arbitrary linear combination of products mass fraction, it is only required that the resulting progress variable increases monotonically through the flamelet, so that the entire flamelet, from unburned inlet reactants to burnt outlet products, can be uniquely parametrized by c [140]. In Fluent model, c is defined as:

$$c = Y_{CO} + Y_{CO_2} \tag{3.1}$$

The progress variable can be also normalized with the respective mass fractions at equilibrium, so that it varies only from 0 to 1:

$$c = \frac{Y_{CO} + Y_{CO_2}}{Y_{CO}^{eq} + Y_{CO_2}^{eq}} \tag{3.2}$$

Where $c = 0$ represents the mixed unburned state, and $c = 1$ represents the fully burnt state at chemical equilibrium.

The distribution on the flow field of z and c are determined with the solution of a transport equation for each one. In particular, besides a transport equation for Favre-averaged mixture fraction, Fluent solves a transport equation for Favre-averaged *un-normalized* progress variable, so that cross derivatives of mixture fractions due to the dependence $Y_i^{eq}(z)$ in (3.2) are avoided [139]. The two equations of transport are expressed in the form:

$$\frac{\partial \bar{\rho}\tilde{z}}{\partial t} + \frac{\partial \bar{\rho}\tilde{u_i}\tilde{z}}{\partial x_i} = \frac{\partial}{\partial x_i}\left(\bar{\rho} D_{tot} \frac{\partial \tilde{z}}{\partial x_i}\right) \tag{3.3}$$

$$\frac{\partial \bar{\rho}\tilde{c}}{\partial t} + \frac{\partial \bar{\rho}\tilde{u_i}\tilde{c}}{\partial x_i} = \frac{\partial}{\partial x_i}\left(\bar{\rho} D_{tot} \frac{\partial \tilde{c}}{\partial x_i}\right) + \overline{\dot{\omega}_c} \tag{3.4}$$

where $\bar{\rho}$ is the Reynolds averaged density, $\tilde{u}_i$ is the i-component of velocity and $\overline{\dot{\omega}_c}$ is a source term of the progress variable. The turbulent fluctuations of both the quantities are closed with the classic gradient diffusion hypothesis, leading to the total diffusion coefficient:

$$D_{tot} = D + D_t = \frac{\nu}{Sc} + \frac{\nu_t}{Sc_t} \tag{3.5}$$

Note that the molecular diffusivity is not considered negligible with respect to the turbulent mass diffusivity.

The source term for the progress variable ($\overline{\dot{\omega}_c}$ in (3.4)) is fundamental for the description of the flame in FGM since producing c at one location means advancing in the reaction. There are different methods to close the progress variable source term and this is maybe the modelling choice that most influence the flame structure. In Fluent there are three possible closures for $\overline{\dot{\omega}_c}$, referred as Finite Rate (FR), Turbulent Flame Closure (TFC) or an automatic switch to the lower of them. These two approaches are very different and will be explained in the next sections.

3.1.1.2.1 Turbulence-chemistry interaction Once the transport equations for z and c are resolved, there is the need to map the laminar flamelet solution on the turbulent mean or filtered flow field, considering that the characteristics of turbulence motion alter that solution. The

influence of turbulence fluctuations on mean values of the variables is accounted for by a stochastic description of variables. In every point of space and time a variable is described by a Probability Density Function (PDF) defining the probability of occurrence for several states instead of only one fixed state. The PDF $P(x)$ can be thought of as the fraction of time the fluid spends in state x [140]. If the PDF of a variable is known it is possible to compute the averages. Since in the FGM model presented here the two control variables are z and c, a generic quantity φ in the flamelet database, such as temperature or species mass fraction, is expressed in function of them as $\varphi(z, c)$. The fluctuations of φ due to turbulence are attributed to the fluctuations of z and c. Therefore, with the mass-weighted joint PDF of mixture fraction and progress variable the Favre average of a generic quantity φ can be calculated as:

$$\tilde{\varphi} = \int_0^1 \int_0^1 \varphi(z, c)\tilde{P}(z, c)dzdc \tag{3.6}$$

The distribution of PDFs is not known and their computation would be complex and time-consuming. The classic approximation is called "Presumed PDF" approach and assumes *a priori* a functional form for the PDFs. Supposing the statistical independence between z and c it can be written:

$$\tilde{P}(z, c) = \tilde{P}(z)\tilde{P}(c) \tag{3.7}$$

For the single PDFs for z and c it is presumed that they are β-distributed. The β-function is very flexible and can be expressed only in function of the first and second statistical moment of the variable, i.e. the mean and the variance:

$$\tilde{P}(z) = \tilde{P}(z, \tilde{z}, \widetilde{z''^2}) \tag{3.8}$$

$$\tilde{P}(c) = \tilde{P}(c, \tilde{c}, \widetilde{c''^2}) \tag{3.9}$$

With the presumed PDFs the problem is now closed by only solving another couple of transport equations for the mixture fraction and progress variable variance.

However, computing the mean quantities from the flamelet data at runtime according to the integral of (3.6) is very inefficient [140]. To decrease the computational cost, commonly the integration is made before the CFD simulation with multiple different PDFs defined on a discrete $z - c$ grid, since the mean and the variance values can span in a restricted range ($\tilde{z}, \tilde{c} \in [0, 1]$; $\widetilde{z''^2} \in [0, \tilde{z}(1 - \tilde{z})]$; $\widetilde{c''^2} \in [0, \tilde{c}(1 - \tilde{c})]$). The pre-integrated database contains the values of mean quantities in function of every possible mean and variance value of mixture fraction and progress

variable:

$$\tilde{\varphi} = \tilde{\varphi}(\tilde{z}, \widetilde{z''^2}, \tilde{c}, \widetilde{c''^2}, \tilde{h}) \tag{3.10}$$

Actually, the integration can be made also at different levels of enthalpy h to account for non-adiabatic effects on reaction. At the end the effective "manifold" that is accessed by Fluent is this pre-integrated database or look-up table or PDF table.

In the next sections the will be presented in detail two different closures for the progress variable source term, both available in Fluent.

3.1.1.2.2 Finite Rate Closure A first approach to close the source term of progress variable $\overline{\dot{\omega}_c}$ is directly related to the Presumed PDF approach. As for a common quantity φ in (3.6), the PDF can be used to average the reaction rate in function of the mixture fraction and progress variable obtained by the same laminar flamelet solution used for the manifold. The progress variable source can thus be expressed as [139, 140]:

$$\overline{\dot{\omega}_c} = \bar{\rho}\widetilde{\left(\frac{\dot{\omega}}{\rho}\right)} = \bar{\rho}\iint \frac{\dot{\omega}(z,c)}{\rho(z,c)}\tilde{P}(z,c)dzdc \tag{3.11}$$

where $\dot{\omega}(z,c)$ is the reaction rate for the flamelet. With the same assumptions of statistical independence of z and c (3.7) and β-distributed PDFs leading to (3.8) and (3.9) the model is closed. The source is then included in the pre-integrated database in function of statistical moments of z and c and enthalpy level:

$$\overline{\dot{\omega}_c} = \overline{\dot{\omega}_c}(\tilde{z}, \widetilde{z''^2}, \tilde{c}, \widetilde{c''^2}, \tilde{h}) \tag{3.12}$$

The Finite Rate closure does not include any hypothesis on the flame other than those made for the use of FGM, so it can be seen as a "physic" closure. For this reason the Finite Rate has no model constants to set or tune and this is usually an advantage that save much modelling time. Nevertheless, the uncertainties relative to approximation of the variance of progress variable $\widetilde{c''^2}$ besides the presumed β-shape for the PDFs can cause an inaccurate prediction of flame position [139]. In this case there are only indirect changes to improve the prediction such as choosing another shape for the PDFs, vary the turbulent Schmidt number or change some constants in the progress variable variance transport equation [141]. Another possibility is to operate on the chemistry changing the flamelet type (diffusion or premixed) or the discretization of the manifold.

3.1.1.2.3 Turbulent Flame Closure Another approach to the closure of progress variable source term $\overline{\dot{\omega}_c}$ passes through the definition of the turbulent flame speed S_t, sometimes referred as TFS. A premixed freely-propagating turbulent flame front consumes fresh mixture much more rapidly than a laminar flame would do. The main reason is that turbulence causes the wrinkling of flame front, increasing significantly the area of contact between reactants, besides an enhanced transport due to turbulence. Locally, the flame front propagates at speed comparable to laminar flame speed but different from the velocity of a freely-propagating unstretched laminar flame front S_l^0 because of the effects of stretch. Nevertheless, the time averaged flame front (flame brush) moves toward the fresh gas at a speed even with an order of magnitude greater than S_l that is the turbulent flame speed S_t. This phenomenon allows to burn much quicker fuel in higly turbulent flows enabling, for example, compact gas turbines combustion chambers or efficient IC engine combustion. The turbulent flame speed closure models use this turbulent flame speed to define the progress variable source as [142]:

$$\overline{\dot{\omega}_c} = \rho_u S_t |\nabla \tilde{c}| \tag{3.13}$$

where ρ_u is the density of unburned gas and S_t the turbulent flame speed. With a closure of this form the transport equation for c describes the motion of a wave whose speed is S_t. Thus the TFC closure moves the problem to the determination of an expression for the turbulent flame speed. There are different models to account for S_t but the most used in gas turbines applications is Zimont's [142] turbulent flame speed correlation. Nevertheless, a valid alternative is Peters's [138] model. In the next the model of Zimont will be described.

Zimont TFC Zimont [142] derived its model from only dimensional considerations and the notion of turbulent energy cascade for high Reynolds number and moderately fast chemistry. The model is valid in the thickened-wrinkled flamelet or thin reaction regime ($Da > 1$, $Ka > 1$), characteristic regime for lean premixed gas turbine combustion, when smaller vortices of Kolmogorov length (L_k) are smaller than laminar flame thickness but larger than reaction zone width, preserving the flamelet structure (Figure 3.2). In fact the main effect is the increase in diffusion process inside the flame front and consequently the flame thickness: larger and larger eddies penetrate the flame front until convection, heat conduction and chemical diffusion reach a new condition of equilibrium. The result of this process is an thickened and wrinkled flame front that moves at higher speed. On the other hand, bigger vortices of integral length scale

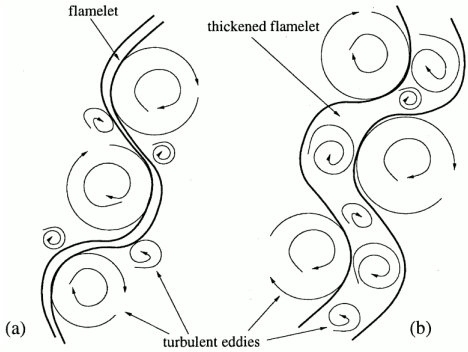

Figure 3.2: Representation of wrinkled (a) and thickened-wrinkled (b) flamelet [19].

(L_t), that are larger than flame front width, wrinkle the thickened flamelet and increase the flame surface. Assuming that turbulent flame speed is proportional to the thickened front speed and the wrinkled surface, with dimensional analysis Zimont derived the expression [143]:

$$\frac{S_t}{S_l^0} \simeq (Re_t Pr)^{\frac{1}{2}} Da^{-\frac{1}{4}} \tag{3.14}$$

where

$$Re_t = \frac{u' L_t}{\nu}, \quad Da = \frac{\tau_t}{\tau_c}, \quad Pr = \frac{\nu}{\alpha} \tag{3.15}$$

indicate respectively the turbulent Reynolds number, the Damköhler number and Prandtl number. u', L_t and $\tau_t = L_t/u'$ are the integral scales of turbulence; ν and α are the kinematic and thermal diffusivity and $\tau_c = \delta_l^0/S_l^0 = \alpha/S_l^{0\,2}$ is a characteristic chemical time scale; S_l^0 and δ_l^0 are the unstretched laminar flame speed and thickness. The quantities are relative to unburned gas conditions. Substituting the expressions (3.15) of the non-dimensional numbers in equation (3.14) yields to the final formulation:

$$S_t = A\, u'^{\frac{3}{4}} S_l^{0\,\frac{1}{2}} \alpha^{-\frac{1}{4}} L_t^{\frac{1}{4}} \tag{3.16}$$

The term A is an empirical constant value referred as Zimont costant.

This turbulent flame speed definition can be easily implemented in a CFD code since it contains only physical-chemical parameters that can be found in literature or calculated and large scale turbulence parameters. As Zimont stressed, no fast chemistry assumption is made and the model

is based on underlying physical behaviour of flame. Changes in pressure, fuel concentration and composition will affect S_l^0 and α values and thus the turbulent flame speed S_t respecting the flame physics. The only tuning constant is constant A.

Equation 3.16 does not account for the effects due to the stretch of flame front. Instead, the turbulence increases always the turbulent flame speed in this model. The stretch is defined by the fractional rate of change of a flame surface element [64] and its effects on flame speed are fundamental for a correct simulation of combustion, especially in low-emission gas turbines applications and near blow-off conditions and every combustion model should include them. Zimont et al. [142] extended the previous form by adding a stretch factor G that describes the probability that the stretch will *not* quench the flame:

$$G = \frac{1}{2}\mathrm{erfc}\left(-\sqrt{\frac{1}{2\sigma}}\left(\ln\left(\frac{\varepsilon_{cr}}{\varepsilon}\right)+\frac{\sigma_\varepsilon}{2}\right)\right) \tag{3.17}$$

$$\varepsilon_{cr} = 15\nu g_{cr}^2, \quad \sigma_\varepsilon = \mu_{str}\ln\left(\frac{L_t}{L_k}\right) \tag{3.18}$$

where ε_{cr} is the turbulence dissipation rate ε at critical strain g_{cr} and σ_ε is the standard deviation of the ε distribution with μ_{str} is a costant of value 0.26. Recasting Equation (3.17) in (3.16) leads to:

$$S_t = A\,G\,u'^{\frac{3}{4}} S_l^{0\,\frac{1}{2}} \alpha^{-\frac{1}{4}} L_t^{\frac{1}{4}} \tag{3.19}$$

that is the final form including stretch effects correction.

The stretch factor (3.17) was determined using the theory on flamelets quenching by Bray [144]: the strained flamelets are reduced to a binary status as either unstrained with no quenching or highly strained flamelets with no contribution to reaction progress by comparing their strain or velocity gradient g to a critical value g_{cr} at which flame extinction is achieved. The higher the value of g_{cr}, the less S_t will be influenced by stretch. This critical value can span over a fairly wide range and is actually the only tuning parameter of the closure [142]. A simple correlation to estimate the value of g_{cr} is [139, 143]:

$$g_{cr} = \frac{B S_l^{0\,2}}{\alpha} \tag{3.20}$$

where B is a constant around 0.5 that should be adjusted in the particular case. It is interesting to note that the correlation (3.20) can be derived from the expression for the stretch Karlovitz number $Ka = \kappa\delta/S_l^0$ assum-

ing $\delta = \alpha / S_l^0$, so the constant B can be thought as a "critical Karlovitz number".

Even with an expression for g_{cr}, the stretch factor formulation results too simple and not very consistent to predict well the influence of stretch on flame speed. The evaluation of g_{cr} is critical to achieve good results [142] and there are considerable uncertainties on its determination. For this reason, the value of g_{cr} is usually a tuning parameter that needs the comparison with experimental data. It is possible to modify Zimont's formulation to include a more complex dependence on stretch, as will be explained in section 3.1.1.3.1.

Zimont's TFC closure was originally developed in RANS context, but the application to LES simulation is straightforward [143]. In fact turbulence large scales enter the formulation through the turbulence kinetic energy dissipation rate that is valid for all scales in the Kolmogorov cascade. This consideration allows to simply refer the scales of turbulence to the filter dimension (Δ) rather than the integral length scale leading to [145]:

$$S_t = A\, G\, u'^{\frac{3}{4}}_{\Delta} S_l^{0\,\frac{1}{2}} \alpha^{-\frac{1}{4}} \Delta^{\frac{1}{4}} \tag{3.21}$$

It is very important that the filter dimension falls in the inertial interval of turbulence spectrum to satisfy the fundamental physical considerations of the model. Furthermore, Δ must be larger than the width of the flame front in order to have thickened-wrinkled flamelets at subgrid level. In other words it is necessary that the grid is coarse enough to ensure that micro-scales of turbulence are not resolved but modelled. For the stretch factor G it can be used the expression (3.17), if it is implicitly made the hypothesis that the contribution for the dissipation spectrum is contained entirely in the subgrid scales [143].

In the commercial code ANSYS Fluent [139] the LES formulation of the model is slightly different since it includes the Smagorinsky constant C_s:

$$S_t = A\, G\, u'^{\frac{3}{4}}_{\Delta} S_l^{0\,\frac{1}{2}} \alpha^{-\frac{1}{4}} (C_s \Delta)^{\frac{1}{4}} \tag{3.22}$$

The constant A in original LES formulation (3.21) has not a well defined value and the two expression (3.21)-(3.22) are equivalent if the Smagorinsky constant is implied in A constant.

3.1.1.3 Influence of stretch on laminar flame speed

In the previous section it was highlighted how the inclusion of stretch effects on flame speed in Zimont's turbulent flame closure is not very reliable due to its excessively simple formulation and the need to tune g_{cr}

value. In general, the stretch increases the gradients of all quantities across the flame front. For example, higher fuel mass concentration gradient means more diffusion transport of reactants that make the flame burn and move faster [146]. On the other hand the increased temperature gradients determine a cooling of the flame front, reducing the speed of chemical reactions. Clearly the overall effect on flame speed depends on the relative weight of the two transport processes (i.e. conduction and fuel diffusion) and can be described in function of the Lewis number of the fuel $Le_F = \alpha/D$, ratio between thermal and species diffusivity. If only these two effects are considered, $Le_F < 1$ leads to an higher flame speed thanks to prevalent diffusion of fuel while with $Le_F > 1$ the main stretch effect is heat loss by conduction. Actually, another fundamental parameter that controls flame response to stretch is the heat loss by radiation, that can quench the flame even if thermal conduction and species diffusivity effects are balanced ($Le_F = 1$). In the limit of small stretch and one-dimensional flame it is possible to derive a simple relation to describe the impact on flame speed.

Defining rigorously the flame speed as the consumption speed at which the reactants are consumed [146]:

$$S_c = \frac{1}{\rho_u Y_F} \int_{-\infty}^{+\infty} \dot{\omega}_F dn \tag{3.23}$$

where ρ_u is the unburned gas density, Y_F the mass fraction of fuel and $\dot{\omega_F}$ the mass burning rate of fuel per unit volume. From asymptotic analysis can be found that the stretched consumption speed S_c is affected linearly by the stretch κ [146]:

$$\frac{S_c}{S_l^0} = 1 - MaKa \tag{3.24}$$

with the Markstein Ma and Karlovitz stretch number Ka defined as:

$$Ma = \frac{\mathcal{L}}{\delta_u}, \quad Ka = \frac{\delta_u}{S_l^0}\kappa \tag{3.25}$$

where $\mathcal{L}$ is the Markstein length, $\delta_u = \alpha_u/S_l^0$ is the laminar flame front thickness and S_l^0 is the unstretched laminar flame speed. According to equation (3.24), the importance and the quality of the flame speed response to stretch (Ka) is decided by Markstein number value and sign. It must be stressed that the equation (3.24) is verified only for small values of stretch, because for higher values non-linear effects are expected [20], so it would not be applicable in industrial highly-turbulent combustion framework. Furthermore, the flame sensitivity to stretch can be intensified

if the flame is considered non-adiabatic and there are heat losses, so a combined model with both the effects interaction is needed [147].

Assuming that for highly turbulent flows with $Ka > 0.1$ the strain a can be considered equal to the stretch κ (i.e. the curvature contribution to stretch is negligible), Tay-Wo-Chong et al. [147] [20] conducted 1D calculations of strained premixed flamelets in asymmetric counterflow configuration to investigate the effects of stretch on flame speed. They finally proposed in [20] an empirical correlation on the basis of the same dimensionless parameters in (3.24) and a new non-dimensional heat loss parameter φ:

$$S_c = S_l^0 \exp[-Ka(Ma + \varphi)] \tag{3.26}$$

The heat loss parameter φ was expressed as [20]:

$$\varphi = \frac{E_a}{2RT_{ad}} \left(\frac{1-\beta}{\beta^4} \right) \tag{3.27}$$

where E_a is the activation energy of main reaction (assumed constant), R is the specific gas constant, T_{ad} is the temperature of products in adiabatic conditions; β is referred as heat loss coefficient and indicates the level of non-adiabaticity as much as it decreases from unity ($0 < \beta < 1$). It is calculated as:

$$\beta = \frac{T_{prod} - T_u}{T_{ad} - T_u} \tag{3.28}$$

with T_u being the temperature of unburned mixture and T_{prod} the temperature of products. The Karlovitz number defined as in (3.25) was evaluated assuming a stretch of $\kappa = a = -du/dx$ for the flamelets while the Markstein number was calculated to best fit the consumption speed values obtained in adiabatic simulations ($\varphi = 0$) in an exponential function.

The correlation (3.26) was derived from one-dimensional simulations of steady laminar flamelets in the asymmetric configuration [20] (fresh-to-burnt) carried out with the software RUN1DL and detailed chemical reaction mechanism GRI 3.0. Only mixtures of methane-air in equivalence ratio range of $0.59 < \varphi < 0.83$ were considered at atmospheric operating conditions ($T_u = 293$ K and $p = 1$ atm). At first adiabatic flamelets were simulated for all equivalence ratio range varying the strain from $a = 180$ 1/s to $a = 10000$ 1/s. The strain determined and enhanced diffusion of radicals due to increased gradients and thinner flame front, that progressively moved to the stagnation point. Though, due to hot temperature of products at adiabatic conditions no complete extinction was observed. An exponential dependence of consumption speed on

stretch (or Ka) was deduced. The Markstein number Ma was introduced similarly to (3.24) and its value was determined to fit the 1D calculations data. Successively, non-adiabatic conditions were obtained by reducing the temperature of products. Some of the results of Tay-Wo-Chong et al. [20] for $\phi = 0.71$ are reported in Figure 3.3.

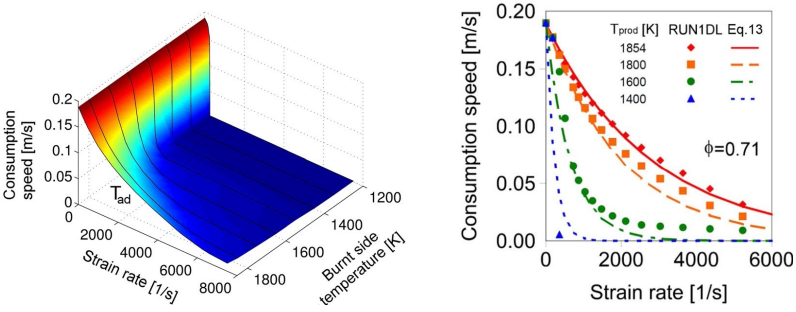

Figure 3.3: Consumption speed dependence on strain rate and burnt side temperature obtained by Tay-Wo-Chong et al. [20] (RUN1DL, $\phi = 0.71$ methane-air asymmetric counterflow flamelets).

From Figure 3.3a it can be seen that the sensitivity of the consumption speed to heat loss (inversely proportional to burnt side temperature) is small for low strain values. Instead, for higher strain values the heat loss increases significantly the reduction of consumption speed, leading to extinction of flamelet for strain higher than 300 1/s and $T_{prod} < 1500$ K. As can be seen in Figure 3.3b, the accuracy of correlation (3.26) can capture main features of flamelet behaviour, even if for strain lower than 200 1/s and temperatures below 1500 K the consumptions speed is overestimated [20].

Analysing the functional form of the correlation (3.26) some considerations can be made. The unstretched laminar flame speed is reduced with a negative exponential term primarily function of stretch (or here equivalently strain) that is included in Karlovitz number Ka. The effects of gas included in Ma and the heat loss φ determine an amplification factor of stretch effect, because $\varphi > 0$ (by definition) and $Ma > 0$ in the methane-air flamelets simulated by [20]. A such direct effect of heat loss on flame speed is related to the strong dependence of chain branching reactions on flame temperature. It is also interesting that if equation

(3.26) is linearized for low strain values ($Ka \simeq 0$) and no heat losses ($\varphi = 0$) it can be derived the exact form of (3.24).

As the authors [20] of the correlation highlight, the validity range is not very large, but following their approach it is possible to calculate a three-dimensional look-up table from flamelet calculations to describe the dependence of consumption speed on equivalence ratio, strain and burnt side temperature. It is probable that with different gas, equivalence ratio and operative conditions a new functional form of heat loss (3.27) and correlation itself (3.26) would be needed.

3.1.1.3.1 Extended TFC model The availability of a correlation like the (3.26), that quantifies the effects of even high stretch with its sensitivity to heat losses on the flame speed, overcomes the restrictions linked to classical asymptotic result of (3.24), valid only for small values of stretch. In fact, the correct account for high strain levels is mandatory in high Reynolds lean combustion modelling, since the quenching effects due to flame front distortion are expected to govern flame parameters like shape, emissions and blow-off. It is thus very important that such effects are included in combustion models.

With this objective, Tay-Wo-Chong et al. [20] (2016) defined a stretch factor I_0 integrating the the consumption speed S_c (3.26) and the unstretched laminar flame speed with a stretch probability density function $P(a)$. Providing a definition for $P(a)$ the stretch factor could be used as reduction coefficient in combustion models that are based on progress variable equation, only by multiplying the progress variable source: $\overline{\dot{\omega}_c} \rightarrow I_0\overline{\dot{\omega}_c}$. They applied this approach to reaction rate model of Schmid [148] in URANS framework, achieving good improvement of flame prediction in a swirl stabilized premixed burner.

As an alternative approach, followed in this work, it is possible to include stretch effects in combustion models that require the specification of a laminar flame speed, for example the Turbulence Flame Closure by Zimont (3.19). This was the approach followed earlier by Tay-Wo-Chong et al. [147] in RANS simulation and recently by Tay-Wo-Chong et al. [149] that explored a similar application for LES. This is also the method used in the present work and it will be explained in detail in the following section.

The main idea is that the stretch influence on flame can be included in Zimont TFC model (3.19) simply by:

1. replacing the unstretched laminar flame speed S_l^0 with the consumption speed S_c defined by the correlation (3.26). In fact, in the model the only term that includes the chemical kinetics is the

laminar flame speed, while the others are characteristics of large scale turbulence or physical properties;

2. omitting the stretch factor G, that was intended to account for reactivity reduction due to the quenching of stretch.

The correlation of Tay-Wo-Chong et al. [20] is implemented in the commercial software ANSYS Fluent v16.2[139] with an user-defined function (UDF) written in C-language. This was necessary because the correlation depends on many flow properties that vary with time and position and are resolved at runtime. In other words, there is the need to access and combine the CFD solver variables during the calculation. The details of the implementation are reported in the next sections. It is highlighted that this model does not require a noticeable increase of computational cost, since no additional transport equations are solved. In the following sections it is first presented the implementation for RANS application and the relative model of turbulent flame closure. Then, the LES formulation is derived with only few simple changes relative to the difference spectrum of turbulence modelled.

RANS implementation in Fluent In this section it is explained how the consumption speed correlation is integrated with Zimont TFC model in Fluent v16.2 [139]. By (1) substituting the consumption speed S_c to unstretched laminar flame speed S_l^0 and (2) omitting the stretch factor $G(g_{cr} = 10^8) \simeq 1$ the extended TFC model reads:

$$S_t = A\, u'^{\frac{3}{4}} S_c^{\frac{1}{2}} \alpha^{-\frac{1}{4}} L_t^{\frac{1}{4}} \tag{3.29}$$

where the consumption speed follows the correlation (3.26) proposed by Tay-Wo-Chong et al. [20].

The model constant A, that in standard Zimont model for RANS is assumed $A = 0.52$, here requires a tuning and a validation of the model over experimental data, since there are no reasons to assume the value for the standard model.

To implement this new model in Fluent it is necessary to replace the default laminar flame speed function with the consumption speed. An user-defined function (UDF) in C language is developed, providing a subroutine that during the simulation accesses flow and material information and returns the consumption speed, according to the correlation above. The obtained value of S_c is passed to the solver within the information of the material, replacing the default laminar flame speed.

However, every term in (3.26) requires a further definition that is analysed singularly in the next paragraphs.

Unstretched laminar flame speed S_l^0
In the FGM implementation in Fluent the unstretched laminar flame speed is automatically calculated for the conditions at which the manifold is created interpolating an internal database and obtaining a function of mixture fraction $S_l^0(z)$. This laminar flame speed function has to be replaced by the consumption speed provided by the UDF, but it is necessary to provide an expression for the unstretched laminar flame speed as input for the calculations within the UDF (see (3.26)).

Stretch Karlovitz Number Ka
The stretch Karlovitz number is defined as:

$$Ka = \frac{\delta_u}{S_l^0} a \tag{3.30}$$

with δ_u being the laminar flame front thickness and S_l^0 is the unstretched laminar flame speed. Note that the correlation is based only on strain influence, neglecting the curvature effects, i.e. $\kappa \simeq a$. The laminar flame thickness is calculated as the diffusive thickness [146] expressed by $\delta_u = \alpha_u / S_l^0$, where the unburned thermal diffusivity α_u is derived from the unburned kinematic diffusivity ν assuming a Prandtl number of $Pr = \nu/\alpha = 0.7$. The value of kinematic diffusivity is estimated through a fourth-order polynomial function of the unburned gas temperature and density.

As far as concern the strain a it is necessary a more complex modelling, since it represents, besides the heat loss, the main influence of the flow field on consumption speed value. The strain is defined as function of velocity by:

$$a = (\delta_{ij} - n_i n_j) \frac{\partial u_i}{\partial x_j} \tag{3.31}$$

where δ_{ij} is the Kronecker delta and $\boldsymbol{n}$ is the normal vector to the flame front.

In principle the strain a can be either positive or negative and the effects on the reaction rate and flame speed is different [150]. While a positive strain slows the reactions, under negative strain it can be maintained or even increased. Since there is no specular response of flame over positive and negative values of strain, to simplify the model following Tay-Wo-Chong et al. [20], it is assumed that with negative strain the consumption speed is equal to unstretched laminar flame speed. This was implemented with a lower limiter of zero for the strain.

In RANS framework the relation (3.31) is Favre-averaged leading to:

$$\tilde{a} = (\delta_{ij} - \widetilde{n_i n_j})\frac{\partial \widetilde{u_i}}{\partial x_j} + \left[\widetilde{(\delta_{ij} - n_i n_j)\frac{\partial u_i'}{\partial x_j}}\right] = \widetilde{a}_{mean} + \widetilde{a}_{turb} \tag{3.32}$$

There are two terms that constitutes the averaged total strain: the contribution of mean flow (mean strain) and the contribution of the modelled turbulence to strain (turbulent strain). The mean strain was calculated as in Tay-Wo-Chong et al. [147] with the divergence of averaged velocity:

$$\widetilde{a}_{mean} = \frac{2}{3}\frac{\partial \widetilde{u_i}}{\partial x_i} \tag{3.33}$$

This form was derived from Veynante et al. [151] relation for $\widetilde{n_i n_j}$ in function of the Reynolds stresses with the hypothesis of isotropic turbulence. The second contribution is the one given by the turbulence fluctuations and was computed according to Meneveau and Poinsot [152] Intermittent Turbulence Net Flame Stretch (ITNFS) model. They investigated the influence of stretch induced by a vortex pair on a laminar flame through Direct Numerical Simulations and then extending the results to a turbulent flow integrating the effects over the turbulence spectrum. The results showed that only vortices with a minimum size of roughly 0.44 times the flame front thickness δ can stretch the flame, provided that Kolmogorov scales are even smaller. In fact, small scales do not stretch the flame front as much as the value of their strain suggests and Kolmogorov eddies have no effects on the flame front, mainly because their lifetime is too short. For these considerations they proposed to estimate the turbulent strain from the inverse of the integral time scale $1/\tau_t = \varepsilon/k$, considered as a reference "large scale strain", and then applying a correction with an efficiency function Γ_k. The turbulent strain can thus be expressed according to:

$$\widetilde{a}_{turb} = \Gamma_k \frac{\varepsilon}{k} \tag{3.34}$$

where

$$\log_{10}\Gamma_k = -\frac{1}{s+0.4}e^{-(s+0.4)} + \left(1 - e^{-(s+0.4)}\right)(\sigma s - 0.11) \tag{3.35}$$

$$s = \log_{10}\left(\frac{L_t}{\delta_l^0}\right), \qquad \sigma = \frac{2}{3}\left(1 - \frac{1}{2}\exp\left[-\left(\frac{u'}{S_l^0}\right)^{\frac{1}{3}}\right]\right) \tag{3.36}$$

In the s value the integral lenght scale was calculated as $L_t = 0.37\,u'^3/\varepsilon$ and the flame front thickness was assumed equal to diffusive thickness

$\delta_l^0 \simeq \delta_u = \alpha_u / S_l^0$. In Figure 3.35 the efficiency function dependence on σ coefficient and L_t/δ ratio is plotted . In the light of Meneveau and Poinsot

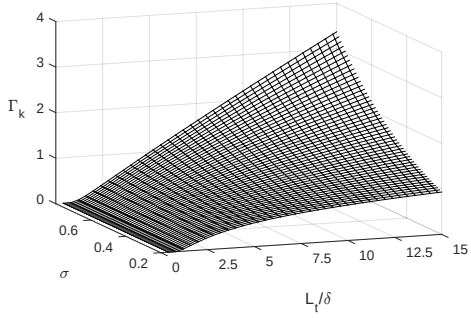

Figure 3.4: Efficiency function Γ_k dependence on L_t/δ and $\sigma(u'/S_l^0)$ according to (3.35).

[152] observations, it was enforced the lower bound of $L_t/\delta \geq 0.44$, to avoid possible divergence of computation since the equation (3.35) has a vertical asymptote in $s = -0.4$ ($L_t/\delta = 0.398$). Furthermore, the limiter on L_t/δ is physically meaningful and is equivalent to impose that the vortices smaller than those that can stretch the flame (according to Meneveau) do not have any influence on stretch.

Markstein number Ma

The Markstein number relative to unburned gases is defined by:

$$Ma = \frac{1-\gamma}{\gamma} \ln\left(\frac{1}{1-\gamma}\right) \tag{3.37}$$

where $\gamma = 1 - \rho_b/\rho_u$ is the gas expansion parameter. The Lewis number of the fuel is considered unitary.

Heat loss parameter φ

The heat loss parameter is calculated as:

$$\varphi = \frac{E_a}{2RT_{ad}} \left(\frac{1-\beta}{\beta^4}\right) \tag{3.38}$$

where E_a is the activation energy of main reaction, R is the specific gas constant, T_{ad} is the temperature of products in adiabatic conditions. According to [20] the activation energy is assumed constant and should be imposed according to a global reaction involving the particular fuel considered, as much as the specific gas constant R. In this study, as will

be explained in the next chapter, the methane-air combustion is analysed and accordingly a constant value of $E_a = 35000$ kcal/kg and $R = 1.9859$ kcal/(kg K) are chosen.

The heat loss coefficient β, that indicated the level of non-adiabaticity, is defined by:

$$\beta = \frac{T_{prod} - T_u}{T_{ad} - T_u} \tag{3.39}$$

with T_u the temperature of unburned mixture and T_{prod} the temperature of products and T_{ad} the temperature of products in adiabatic conditions.

For the implementation the temperature of products T_{prod} is assumed as the local cell temperature. The other temperatures are interpolated from the PDF table in the user-defined function. In RANS framework, the temperatures will be Favre-averaged quantities. In particular the temperature of unburned mixture T_u is extracted from the PDF table using as input zero mean progress variable $\tilde{c} = 0$, mixture fraction variance $\widetilde{z''^2} = 0$ and the adiabatic level of enthalpy $h_{ad}(\tilde{z})$. Similarly, the adiabatic products temperature T_{ad} is extracted with the values of mean progress variable $\tilde{c}$ and mixture fraction variance $\widetilde{z''^2}$ in the cell with the local adiabatic level of enthalpy $h_{ad}(\tilde{z})$. The resulting synthetic expression is reported below (3.40).

$$\beta = \frac{\tilde{T}(\tilde{z}, \widetilde{z''^2}, \tilde{c}, \widetilde{c''^2}, \tilde{h}) - \tilde{T}(\tilde{z}, \widetilde{z''^2} = 0, \tilde{c} = 0, \widetilde{c''^2}, h_{ad}(\tilde{z}))}{\tilde{T}(\tilde{z}, \widetilde{z''^2}, \tilde{c}, \widetilde{c''^2}, h_{ad}(\tilde{z})) - \tilde{T}(\tilde{z}, \widetilde{z''^2} = 0, \tilde{c} = 0, \widetilde{c''^2}, h_{ad}(\tilde{z}))} \tag{3.40}$$

LES implementation in Fluent The formulation presented in the previous section can be extended to LES applications with simple considerations, as shown recently by Tay-Wo-Chong et al. [149]. A such application should increase not only the accuracy of flame characteristics but also the dynamics.

In LES context the standard TFS model is implemented in Fluent [139] as:

$$S_t = A\, G\, u'^{\frac{3}{4}}_{\Delta} S_l^{0\,\frac{1}{2}} \alpha^{-\frac{1}{4}} (C_s \Delta)^{\frac{1}{4}} \tag{3.41}$$

The correlation of consumption speed can be applied in the same way as for RANS, that is substituting the unstretched laminar flame speed and omitting the G stretch factor by setting a $g_{cr} = 10^8$ 1/s. The extended formulation of Zimont TFC for LES reads:

$$S_t = A\, u'^{\frac{3}{4}}_{\Delta} S_c^{\frac{1}{2}} \alpha^{-\frac{1}{4}} (C_s \Delta)^{\frac{1}{4}} \tag{3.42}$$

similar to the RANS formulation (3.29). The value of constant A is usually set as 1.5 for LES simulations in the standard formulation but here are valid the same considerations made for RANS formulation and it is necessary a tuning for its value.

Besides the differences of Zimont formulation already described in the previous section, the only changes in consumption speed formulation concern the definition of Karlovitz number Ka. All the other parameters (Markstein number Ma and heat loss φ) are not affected in their implementation by the different turbulence treatment in LES and they will not be repeated here.

The strain definition (3.31) can be filtered leading to:

$$\tilde{a} = \widetilde{a}_{res} + \widetilde{a}_{subgrid} \tag{3.43}$$

Similarly to RANS, the total filtered strain is defined as sum of the filtered strain generated by resolved scales and the filtered strain of subgrid turbulence. The resolved strain is calculated in the same way as (3.33) only by substituting the time-averaged with the resolved velocity. The subgrid turbulence strain is calculated from the inverse of the subgrid time scale and the efficiency function Γ_k:

$$\widetilde{a}_{subgrid} = \frac{\Gamma_k}{\tau_\Delta} \tag{3.44}$$

where the efficiency function has the form of ITNFS model [152], extended according to Tay-Wo-Chong et al. [149]:

$$\log_{10}\Gamma_k = -\frac{1}{s+0.4}e^{-(s+0.4)} + \left(1 - e^{-(s+0.4)}\right)(\sigma s - 0.11) \tag{3.45}$$

$$s = \log_{10}\left(\frac{\Delta}{\delta_l^0}\right), \qquad \sigma = \frac{2}{3}\left(1 - \frac{1}{2}\exp\left[-\left(\frac{u'_\Delta}{S_l^0}\right)^{\frac{1}{3}}\right]\right) \tag{3.46}$$

It is worth to note that now the model is mesh-dependent since the efficiency function Γ_k is a function of the filter length Δ, which is considered comparable to the scale of biggest vortices modelled. With coarser grids the subgrid turbulence scales span over a wider range and the relative correction (i.e. the efficiency) for the small scales that do not influence strain becomes smaller. This leads to an increase of turbulent strain with the cell dimension, since the turbulent mixing rate ($1/\tau_\Delta$) is not much sensitive to filter length.

3.2 Flame Response Computation

As mentioned in Chapter 2, direct computational simulations of combustion instabilities, although possible, are impractical in the industrial framework.

This strategy is the self-excited method and directly provides the frequency and the amplitude of the pressure pulsations. In a self-excited computation, the simulation becomes unstable by itself. A computational domain ranging from compressor outlet to turbine inlet is required, in order to reproduce the physical boundary conditions of the engine.

An alternative approach is the forced response method, which is investigated in this work and consists of different steps: at first a statistically stable unsteady CFD solution should be obtained, without excitation of the boundaries. Then, using this simulation as an initial solution, the flame is excited by superimposing a perturbation in terms of acoustic pressure, velocity, mixture fraction or other driving mechanisms. Finally, time series of input and output quantities are postprocessed in order to get the required transfer/describing functions, to be implemented in a low-order acoustic network model or a 3D Helmholtz solver.

FTF represents the response of the flame to small amplitude perturbations and can thus be only used to predict whether a thermo-acoustic system is stable (without oscillations) or unstable (increasing oscillations).

However, in order to predict not only the onset of pressure oscillations, but also their amplitude (and, as a consequence, their impact on the engine reliability), the Flame Describing Function shoul be considered.

3.2.1 Identification Strategy

In this section, the procedure used to study the flame dynamics in the application of this work is described. The procedure is based on the coupling of numerical simulations and post-process techniques: the System Identification theory has been used to efficently compute the FTF, while frequency analysis have been performed to study the nonlinear response.

The identification of both the FTF and the FDF by CFD requires an unsteady simulation where the flow variables are excited to obtain a system response. The time series of the input variables (i.e. acoustic velocity) and heat release fluctuations are recorded during the simulation, paying attention to the coupling with the FEM code that solve the problem in terms of acoustic variables (p and u).

As pointed out in [5], the kinematic response to acoustic velocity perturbation can be included in the FEM code in a straightforward

manner extracting the velocity fluctuation at the burner exit. The velocity fluctuations are recorded as mass flow average of the axial component of velocity at a reference plane close to burner exit (the sampling plane will be shown case by case in the following sections). As far as the overall heat release, exploiting the FGM combustion model, its definition is:

$$q' = \int_V \rho_u \cdot PFR \cdot LHV \cdot ZdV \tag{3.47}$$

Where LHV is the heat of reaction per unit mass of fuel and $\rho_u \cdot PFR \cdot LHV$ represents the heat released for unity of mixture per second.

3.2.1.1 FTF calculation by means of CFD-SI

Concerning FTF, exciting the system with a carefully designed broad-band signal and exploiting the linearity assumption, system identification (SI) techniques can be used to calculate the flame response over a range of frequencies from one single CFD run.

Such a signal is of paramount importance for the identification quality and the computational costs, as reported by several works in literature where the effects of different excitation signals are assessed and quality checks are proposed in order to verify their capability (see i.e. [5, 105, 153]). The flame response should be calulated, in general, over a well-defined range of frequencies of interest: thus, the perturbation signal has to excite the frequency spectrum in that range, allowing to calculate the FTF with a single CFD simulation.

Some limitations arise on the signal choice: the intensity of the signal should be limited in order to respect the linearity hypothesis lying behind the identification procedure but, on the other hand, should be sufficient to distinguish the signal from the background noise [5]. A much more expensive approach requires to calculate the FTF frequency by frequency by means of harmonic forcing.

A square wave with randomly variable amplitude (RASW) was used as excitation signal in this work. This approach mixes the features of the random binary and random noise signals. The constant period of the square wave fixes the cut-off frequency, while the broad-banding is given by the variable amplitude.

The signal mean is zero and the amplitude varies around it following a Gaussian distribution of imposed variance. Tests on RASW signal showed good features of broad-banding and filtering. For further details please refer to Andreini et al. [154].

The excitation strength of the different simulations has been chosen

in order to avoid poor identification results due to insufficient signal amplitude and, on the other hand, to assure that the maximum amplitudes do not generate non-linear behaviour. The maximum wave amplitude is limited to 20% for acoustic perturbations, while mean amplitude variation is between 5 and 10%. The time series for the SI post-process are exported from CFD each time step.

3.2.1.1.1 System Identification For small perturbation the system representing the flame can be considered a linear time-invariant (LTI) system: For a given input the system responds always in the same way (time-invariant) and the output is only a function of present and past inputs (causal). In absence of noise, from signal theory is known that the system can be fully described by the Unite Impulse Response, UIR, (h_k). Considering a discrete data set, as the CFD data, representing a Single-Input Single-Output system, the output at the instant $t_n = N \cdot \triangle t$ becomes:

$$y_n = \sum_{k=0}^{M} h_k x_{n-k} \tag{3.48}$$

Where y and x are respectively the output (or response) of the system and the input signal, while M is the "problem dimension" that is, the unit impulse h length (in time). This should be able to represent the system and, generally, it can be considered as the longest characteristic time of the system (e.g. a characteristic convective time) [115].

The transfer function can be determined as the Z-Transform of the Unit Impulse Response vector:

$$FTF(\omega) = \sum_{k=0}^{M} h_k e^{-i\omega k \Delta t} \tag{3.49}$$

Therefore, the problem consists in the determination of the UIR from CFD time series. This is accomplished exploiting a non-recursive least square method. In particular, the identification is based on the Wiener-Hopf linear least square estimator which exploits correlation functions between the input and the output of the system (refer to i.e. [109] for a complete treatment on the SI).

3.2.1.2 FDF numerical calculation

Due to the nonlinear regime, FDF cannot be obtained exploiting SI theory for LTI systems but single frequency harmonic signals at different

perturbation amplitude levels, and consequently numerous simulations to calculate the whole flame response over the wide frequency range, are required.

After obtained a statistically-stable unsteady CFD solution, mono frequency harmonic excitations are superimposed on the mean flow at the inlet for each frequency of interest and for each level of incoming perturbation. To obtain the FDF, time series of the velocity upstream of the chamber and the volume integrated heat release by the flame are recorded during the transient CFD runs and normalized by their mean values.

Thus, the FDF for each frequency of interest and for each level of incoming perturbation is calculated by taking the Fourier Transform (FFT) of the time histories:

$$FDF\left(\omega, \left|u'\right|\right) = \frac{FFT\left(\dfrac{Q'\left(\omega, |u'|\right)}{\overline{Q}}\right)}{FFT\left(\dfrac{U'\left(\omega, |u'|\right)}{\overline{U}}\right)} \tag{3.50}$$

3.3 Thermo-acoustic Stability Analysis

Acoustic analysis in the frequency domain, coupled with the flame response calculated by means of experimental measurements, analytical formulation or numerical calculation, represent the state-of-the-art in combustors thermo-acoustic modelling.

Finite Element Methods (FEM) may be used to solve for the complete problem, taking into account the real geometry of the combustors and allowing to detect modes with complex 3D shape (see for example [155]). For that reason, an approach based on 3D FEM modelling of the combustors has been adopted in this work.

3.3.1 Linear Stability Analysis

The set of linear transport equations for the perturbations of velocity, temperature and density can be derived by linearizing the Navier-Stokes equations [156], where the local unsteady heat release appears as a forcing term. It is often assumed that the mean flow is at rest so that a wave equation for the acoustic perturbations can be derived. Thus, the acoustic wave propagation, the unsteady heat release of the flame and its coupling with the acoustics can be completely described in the frequency domain by the inhomogeneous Helmholtz equation:

$$\frac{\lambda^2}{\overline{c}^2}\hat{p} - \nabla^2\hat{p} = -\frac{\gamma-1}{\overline{c}^2}\lambda\hat{q} \tag{3.51}$$

The solution consists in determining the complex resonant frequencies ω of the combustor, whose real part represents the frequency of oscillations and the imaginary one characterizes the stability of a mode. An unstable mode have a negative imaginary part meaning a growing fluctuation amplitude.

The eigenvalue problem is solved in this work with the acoustic module of COMSOL Multiphysics [157] by means of an iterative linearization procedure based on a variant of the Arnoldi algorithm [158].

The heat release fluctuations $\hat{q}$ can be generally related to the acoustic fluctuations at the injection location $\hat{u}_b$ through the Flame Transfer Function:

$$\frac{\hat{q}}{\overline{q}} = |FTF(\omega)|\frac{\hat{u_b}}{\overline{u}}e^{i\measuredangle FTF(\omega)} \tag{3.52}$$

Where the $|\cdot|$ indicates the modulus and the $\measuredangle$ the phase of the response.

FTF represents the response of the flame to small amplitude perturbations and can thus be only used to predict whether a thermo-acoustic system is linearly stable (without oscillations) or unstable (increasing oscillations).

If the analytical $n-\tau$ model is used, $\hat{q}$ becomes:

$$\frac{\hat{q}}{\overline{q}} = -n\frac{\hat{u_b}}{\overline{u}}e^{-i\omega\tau}, \tag{3.53}$$

3.3.1.1 Source term application

In both cases, the source term has to be applied within the flame region only, defining a dedicated sub-volume inside the combustor where the source term is applied or through a mathematical function.

In the applications presented in this work, the flame region is defined exploiting the results of a reactive CFD simulation, in particular the predicted rate of reaction (Product Formation Rate, PFR), following the approach presented and validated in [21]: at first the PFR field is imported in COMSOL, then a mathematical function, F (flame-identifying function), which is zero outside the flame, can be defined. To apply a non-uniform distribution of the source term, a weighting function ($WF(\mathbf{x})$) proportional to the Product Formation Rate (PFR), shown in Figure 3.5,

can be defined in the flame region.

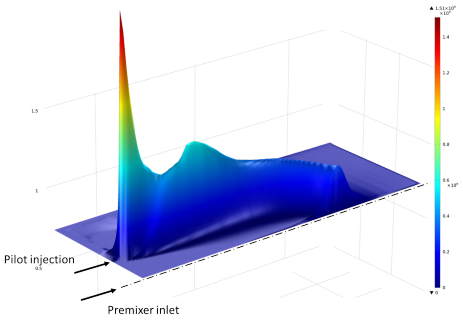

Figure 3.5: Weighting function proportional to the PFR. [21]

The local source term becomes:

$$\overline{q} = \frac{TotalHeatRelease}{\int_V WF(\mathbf{x})} \tag{3.54}$$

and the monopole source:

$$Q^{MP} \propto \overline{q} * WF(\mathbf{x}) * F \tag{3.55}$$

3.3.1.2 Temperature field import

In order to give a more physical representation of the combustor, the temperature distribution is imported in the 3D Helmholtz solver from the CFD results. Consequently, the density and the sound speed assumes local values as:

$$\rho(\mathbf{x}) = \frac{p}{R_g T(\mathbf{x})}, \qquad c(\mathbf{x}) = \sqrt{\gamma R_g T(\mathbf{x})}. \tag{3.56}$$

3.3.1.3 Bloch-Wave Periodicity

Most practical combustors feature a discrete rotational symmetry (Figure 3.6), so that a periodic boundary condition to be used in thermo-acoustic stability analysis should be useful to obtain a significant reduction in computational efforts and memory requirements.

Performing stability analysis on reduced domain, exploiting rotational symmetry, has been already done in [159], by splitting the problem into several steps with alternate boundary conditions. The thermoacoustic

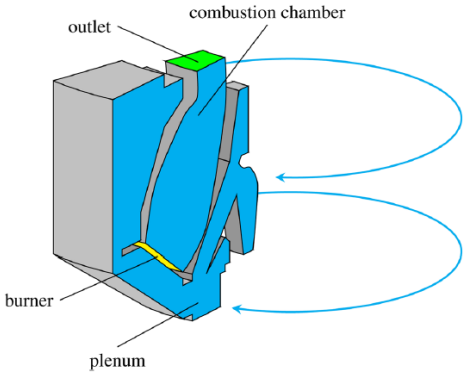

Figure 3.6: Schematic representation of a combustion chamber featuring a discrete rotational symmetry. [22].

modes of the Ansaldo Energia AE94.3A combustion chamber have been recently computed following this approach in [160].

The procedure, applied to one quarter of the annular combustion chamber, consists of two steps: in the first step a symmetric boundary conditions is used, applying the same type of boundary conditions ($u' = 0$) to both the interface planes, while in the second step nonsymmetric boundary conditions are employed, applying different conditions ($u' = 0$ and $p' = 0$) to the interface planes.

A methodology to account for rotational symmetry by considering only one sector, has been recently proposed by [22]. In fact, thermo-acoustic models based on Helmholtz equation admit special solutions of the so-called Bloch type, following a theory originally used in quantum mechanics to solve the Shrodinger equation [161]. These structures are suitable for general thermo-acoustic problems, such as cases with distributed source term and non-uniform physical properties fields within the combustor sector.

Denoting $\mathcal{L}(\omega)$ a linear spatial differential operator which is equivariant by $2\pi/N$, and following the symbols in [22]

$$\mathcal{L}(\omega)\,\widehat{p}\,(\varphi, r, z) = 0 \tag{3.57}$$

being N an integer corresponding to the discrete rotational symmetry of the model, a basis of the eigenspace of the eigenvalue ω can be written as:

$$\widehat{p_{\widetilde{b}}}\left(\varphi, r, z\right) = e^{ib\varphi}\psi_{\widetilde{b}}\left(\varphi, r, z\right) \tag{3.58}$$

where $\widehat{p_{\widetilde{b}}}$ are called Bloch waves (an example of the circumferential structure is given in Figure 3.7), b is an integer named Bloch wavenumber and $\psi_{\widetilde{b}}$ is periodic by $2\pi/N$:

$$\psi_{\widetilde{b}}\left(\varphi + 2\pi/N, r, z\right) = \psi_{\widetilde{b}}\left(\varphi, r, z\right) \tag{3.59}$$

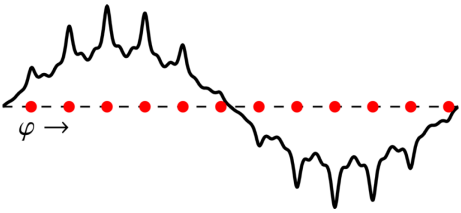

Figure 3.7: General structure of a Bloch Wave with $b = 1$ and $N = 12$. The red dots correspond to the centers of the combustor sectors [22].

For a given degree of rotational symmetry N

$$\widehat{p_{\widetilde{b+N}}}\left(\varphi\right) = e^{i(b+N)\varphi}\psi_{\widetilde{b+N}}\left(\varphi\right) = e^{ib\varphi}\psi_{\widetilde{b}}\left(\varphi\right) = \widehat{p_{\widetilde{b}}}\left(\varphi\right) \tag{3.60}$$

a Bloch wave with wavenumber b can be rewritten as one with wavenumber $b + N$, so that there are only N independent Bloch wavenumbers:

$$\widehat{p_{\widetilde{b}}}\left(\varphi + 2\pi/|b|\right) = e^{ib(\varphi+2\pi/|b|)}\psi_{\widetilde{b}}\left(\varphi + 2\pi/|b|\right) = \widehat{p_{\widetilde{b}}}\left(\varphi\right) \tag{3.61}$$

The whole eigenfunction can be extrapolated from its value on a sector. Given an integer k, according to the Bloch-periodicity:

$$\widehat{p_{\widetilde{b}}}\left(\varphi + k2\pi/N\right) = e^{ib(\varphi+k2\pi/N)}\psi_{\widetilde{b}}\left(\varphi + k2\pi/N, r, z\right) = \tag{3.62}$$

$$= e^{ibk2\pi/N}\widehat{p_{\widetilde{b}}}\left(\varphi\right) \tag{3.63}$$

In this way, the solution of the entire domain can be retrieved from one single sector of an angle of $2\pi/N$ with Bloch-periodic boundary conditions applied to the symmetry boundaries:

$$\widehat{p_{\tilde{b}}}\left(\varphi + 2\pi/N, r, z\right) = \widehat{p_{\tilde{b}}}\left(\varphi, r, z\right) e^{ib2\pi/N} \tag{3.64}$$

The advantages of the Bloch wave approach are:

- A reduced number of mesh elements required, since the domain size is reduced by a factor $1/N$;
- Low computational costs for the extrapolation of the entire solutions;
- Lower memory requirements (the size of the discretization matrices, in fact, is reduced by a factor N^2);
- The possibility to address specific azimuthal mode orders explicitly, by resolving the eigenproblem corresponding to the desired wavenumber b.
- Improved convergence, because, given a specific b, fewer complex eigenfrequencies are possible solutions of the system;
- The capability of deal with complex setup: distributed source terms, non-uniform physical properties fields within the combustor sector and even the effect of asymmetries can be assessed, as pointed out in [22].

Following this approach a different eigenvalue problem has to be solved for each Bloch wavenumber b of interest. For practical configurations, however, only the first wavenumbers, corresponding to the lower frequencies, are relevant. Thus, Bloch wave approach strongly reduces the efforts in terms of computational costs and represents a promising solution in the industrial framework, given the same accuracy as a full domain computation.

3.3.2 Nonlinear Stability Analysis

In order to predict not only the onset of pressure oscillations, but also their amplitude (and, as a consequence, their impact on the engine reliability), the non-linear behaviour of the system should be modelled. Furthermore, noise or non-normal effects may trigger finite amplitude oscillations, even when the thermoacoustic system is linearly stable: in these situations linear stability fails to predict the real behaviour of the system [29], as shown in Figure 3.8.

As already introduced in Chapter 2, considering the flame as the dominant non-linear [31], its behavior is often described in terms of Flame Describing Function (FDF). In this framework, the FDF generalises the

concept of the FTF to perturbations with finite amplitude and can be used to study the amplitude and frequency of limit cycle oscillations, under the following assumptions:

- limit cycle oscillations approximated as harmonic solutions;
- the dynamics of a given thermoacoustic mode decoupled from the dynamics of the others.

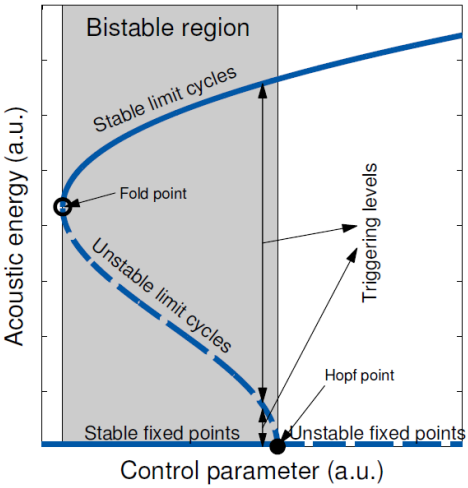

Figure 3.8: Stable (solid) and unstable (dashed) states. Linear stability theory calculates the stability of fixed point solutions with respect to small perturbations. In the bistable region, however, finite amplitude perturbations can trigger the state from the linearly stable fixed points to stable limit cycles, or vice versa [23].

When the FDF is coupled with an acoustic solver and the stability analysis are repeated in the frequency domain at different excitation amplitudes, the approach is defined as *weakly nonlinear*, due to the assumption already discussed. Assuming a weakly nonlinear approach the FDF can be coupled with linear acoustics to predict the nonlinear dynamics of a given system and bifurcation analysis at the variation of a control parameter can be performed.

The procedure is the same already described in 3.3.1 and, repeating the analysis at different excitation amplitudes, the trajectories of growth rates

and oscillation frequencies as a function of perturbation amplitude can be retrieved. Regions of instability, frequency shifts with respect to the acoustic eigenfrequencies and limit cycle amplitude when self-sustained oscillations occur are the outcomes of the analysis.

Concerning the amplitude levels of limit cycles, they can be calculated assuming the equilibrium between the amplitude dependent growth rate and the damping rate of the system, which requires an independent determination of this last quantity.

3.3.2.1 Internal Damping Rate

The Internal Damping Rate has been calculated in this work exploting the combustor resonance response curve calculated by means of unsteady CFD simulations, following the approach proposed by [24]. There is no well established experimental procedure to measure the damping rate under realistic operating conditions. This value can be calculated from the resonance response sharpness by imposing external perturbations in a stable reacting condition. Two acoustic response curves obtained in this way by Palies at al. [24] are shown in Figure 3.9.

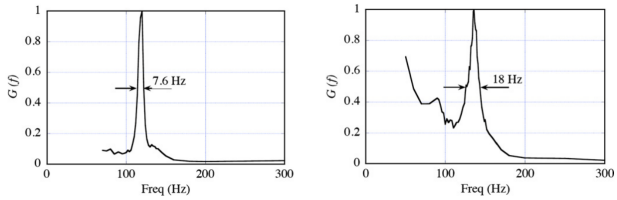

Figure 3.9: Acoustic response sharpness of two operating conditions. The frequency bandwidth Δf determined at half maximum provides the effective damping rates [24].

From the frequency response spectrum it is possible to obtain the half power points which give the frequency bandwidth Δf, as shown in Figure 3.9. As for an harmonic oscillator, the damping rate can be written as:

$$\alpha' \simeq \pi \, \Delta f \tag{3.65}$$

Due to the fact that the flame may damp or drive the oscillations, it is important to consider its effect, considering an "effective" damping rate α' obtained as the sum of the system damping rate α and the growth rate related to the flame dynamics ω_i

$$\alpha' = \alpha - \omega_i \tag{3.66}$$

The proposed methodology consists in calculating α' from the acoustic response and adding an estimate of ω_i, as calculated by system stability analysis in order to obatain an estimation of the system damping rate.

Chapter 4

Stability Analysis of a Full-Annular Lean Combustor for Heavy-Duty Applications

The dynamics of a lean-premixed full-annular combustor for heavy-duty applications has been numerically studied in this chapter. The well established CFD-SI method has been used to investigate the flame response varying operational parameters such as flame temperature and fuel split. The calculated FTFs have been implemented in a 3D FEM model of the chamber, in order to perform linear stability analysis and to validate the numerical approach. A boundary condition for rotational periodicity based on Bloch-Wave theory has been implemented in COMSOL Multhiphysics and validated against full-annular chamber simulations, allowing a significant reduction in computational time. The reliability of the numerical procedure has been assessed through the comparison against full-annular experimental results performed by Baker Hughes GE.

4.1 Combustor Description and Previous Numerical Analysis

The object of the analysis presented in this chapter is a lean-premixed gas turbine combustor for heavy-duty applications, as tested by Baker Hughes GE in a full-annular rig. The geometry of the combustor consists of an annular chamber with 39 equally spaced burners. Each burner features a main premixed flame surrounded by pilot fuel injections. The main flame burns a methane/air mixture, leaving the nozzle through a

converging duct followed by an area expansion in the combustion chamber. The widely employed Dual Annular Counter Rotating Swirl (DACRS) injector provides the mixing between air and main fuel, which is injected within the inner swirler passages. Such a configuration has been choosen as proved to be the most effective solution to reduce NOx emissions over the whole operational range, as observed in a single-cup experimental campaign [162]. A schematic view of the injector is shown in Figure 4.1.

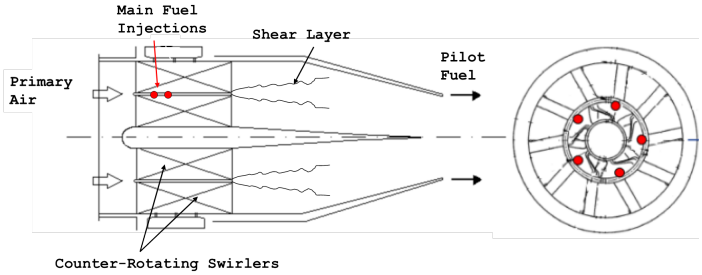

Figure 4.1: Schematic representation of the DACRS injector

Previous numerical analysis have been performed on a similar configuration in [21] to setup and assess the capability of the procedure: at first an idealized partially-premixed flame, featuring a main premixed flame surrounded by axisymmetric pilot fuel injections within a tubular chamber has been numerically studied.

An approach where pilot and premixed flame responses are analysed separately is proposed by Innocenti [163], exploiting the independence of their evolution. The flame response to different perturbations, including the acoustic velocity fluctuations and equivalence ratio oscillations of the premixed flow and the pilot mass flow fluctuations is computed in terms of Flame Transfer Function, exploiting URANS simulations and System Identification techniques. The identified FTFs are analysed in details, providing explanations on the main mechanism affecting the predicted responses and implemented in a 3D FEM model of the full-annular combustor to analyse the system stability. A comparison with results from full-annular combustor experimental campaign has been carried out, allowing to understand the effects of different driving mechanisms on the system stability.

Thus, the aim of this part of the work is to apply the well-established CFD-SI procedure to a real flame, assessing the capability of the analyis in predicting the onset of thermo-acoustic instabilities and in reproducing

the experimental evidences at different operating conditions. Ad hoc strategies to improve the identification quality have been developed and different sensitivities have been carried out, assessing the impact of flame temperature (global equivalence ratio), fuel split and burner pressure drop on the system stability.

A computationally efficient acoustic model of the full-annular combustor has been developed and validated. In fact, during the experimental campaign on the full-annular combustor, larger amplitude pressure fluctuations were measured reducing the amount of pilot fuel and increasing the overall flame temperature, corresponding to the second azimuthal mode of the combustor. Availability of experimental measurements in a wide range of operational conditions allowed an exhaustive comparison study.

4.2 CFD Modelling and Numerical Setup

The simulations reported in this chapter have been performed with the code ANSYS Fluent v17.1 within the URANS framework. The computational domain includes one sector of the annular combustion chamber, the burner and part of the upstream plenum, in order to recreate a homogeneous incoming flow and allow a natural generation of turbulence through the swirler. The cooling system of the heat shield and the liners has been considered, in order to replicate the complex flow field of the reaction zone. The computational domain, with the represented flows highlighted, is shown in Figure 4.2.

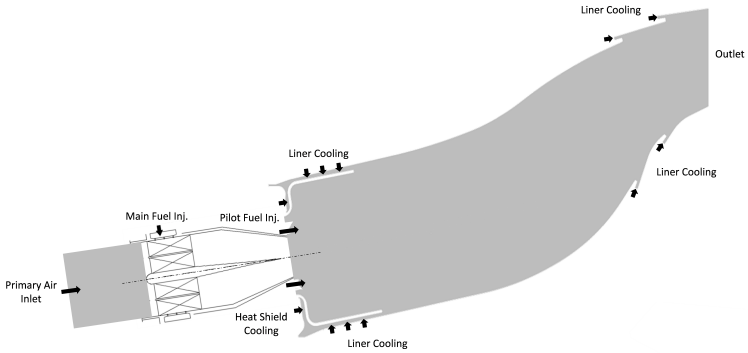

Figure 4.2: Computational domain and represented flows

Different inlets are included in the domain, as shown in Figure 4.2:

- A primary air inlet, upstream the swirlers;
- A main fuel injection, within the inner swirler passages;
- Pilot slot injections, surrounding the main flame, to supply pure fuel for stabilization purposes;
- Air injections along the liners and the heat shield.

The computational mesh in depicted figure 4.3. It consists of approximately 7.5 million polyhedral cells and represents 1/39 of the whole annular geometry. At first an hybrid mesh of about 30 million tetrahedral cells with five layers of prisms adjacent to solid walls was created with ANSYS Meshing and then it was processed with Fluent to generate polyhedral cells.

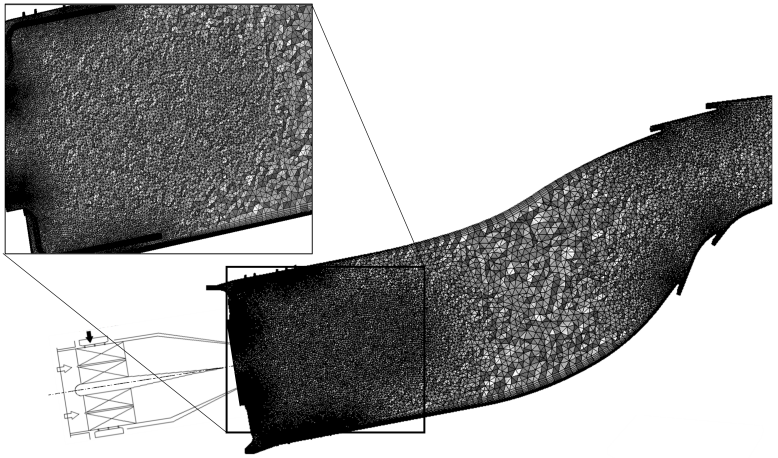

Figure 4.3: Computational grid

Concerning the boundary conditions, a uniform static pressure value has been imposed at the outlet, whereas at the different inlets the experimental mass flow rates have been assigned. The walls of the combustor were assumed to have a constant temperature, following the experimental data provided by Baker Hughes GE, while rotation periodicity has been assigned on the cyclic surfaces.

During the transfer function calculations, a non-reflecting boundary conditions (NRBC) was imposed at the outlet section in order to prevent

resonances inside the domain which could have deteriorated the quality of the response identification. In terms of numerical schemes and solution algorithms, a PISO algorithm together with second order upwind schemes for spatial discretization and a bounded second order implicit formulation for time have been used. A Courant number below 0.7 is assured by the adopted time step of $5 \cdot 10^{-6} s$.

Regarding turbulence modeling, a URANS approach was employed, considering the realizable $k - \varepsilon$ model for the eddy-viscosity closure in order to take into accounts turbulence effects on the solved mean flow [164]. A moderate level of turbulence intensity has been employed at the inlet boundaries because the main turbulent structures were assumed to generate when crossing the swirler geometry.

As far as the combustion modelling is concerned, the Flamelet Generated Manifold (FGM) model has been adopted, where a pre-computed laminar flamelet solution is integrated through a pre-defined probability density function (PDF) to account for turbulence effects. A premixed flamelet configuration has been considered and flamelet equations have been solved using the dedicated solver integrated in ANSYS Fluent and exploiting the Gas Research Institute reaction mechanism GRI Mech 3.0 for methane, with 325 reactions and 53 species. The source term of progress variable has been modelled in the present work using the Finite Rate formulation.

The employed setup has been assessed and validated in [165] through the comparison with detailed experimental measurements on the same burner.

Different sensitivities have been carried out, assessing the impact of several operating parameters on the combustor stability. Among the conditions tested within the experimental campaign, seven test points have been selected, varying the flame temperature (global equivalence ratio), the fuel split between premixed and pilot fuel injections and the burner pressure drop (Table 4.1): such a wide range experimental chracterization represents a great opportunity to validate the employed numerical methods and to give a deeper insight into the flame dynamics.

In fact, increasing the flame temperature and lowering the amount of pilot fuel, a tendency to destabilization of the second azimuthal mode emerges from the experimental measurements. Starting from a stable condition, named 40-L in Table 4.1, which has been used for validation purposes, several sensitivities have been carried out, with the aim of assess the model capability in catching the instability onset.

Table 4.1: Investigated test points and operating conditions.

TP	40-L	25-L	18-L	40-H	25-H	18-H	40LP
Fuel Split	40%	25%	18%	40%	25%	18%	18%
T_{flame}	Low	Low	Low	High	High	High	Low
ΔP	High	High	High	Low	Low	Low	Low

4.2.1 Flame Response Identification

Once obtained a mean URANS solution, the system is excited to generate the time series for the flame response calculation. In particular, in order to investigate the impact of the different operating conditions, acoustic velocity fluctuations are generated at the premixer inlet and recorded at the burner exit.

To obtain the FTF, time series of the velocity upstream of the chamber and the volume integrated heat release by the flame have been recorded during the transient CFD runs. The acoustic velocity and heat release fluctuation have been normalized by their mean values.

Both, broadband and harmonic signals have been used to identify the flame response to incoming acoustic perturbation, upgrading the approach followed in [21] for a simplified axisymmetric flame to describe such a complex configuration.

Concerning the broadband signal a square wave with randomly variable amplitude (RASW) was used. This approach mixes the features of the random binary and random noise signals. The constant period of the square wave fixes the cut-off frequency, while the broad-banding is given by the variable amplitude. The signal mean is zero and the amplitude varies around it following a Gaussian distribution of imposed variance. Tests on RASW signal showed good features of broad-banding and filtering. For further details please refer to Andreini et al. [154].

The excitation strength of the different simulations has been chosen in order to avoid poor identification results due to insufficient signal amplitude and, on the other hand, to assure that the maximum amplitudes do not generate non-linear behaviour.

The employed signal is depicted in Figure 4.4. As can be seen, the RASW signal allows to fix a cut-off frequency at about $St = 1.4$, depending on the period of the square wave, while the broad-banding is given by the variable amplitude. The maximum wave amplitude is limited to 15% for acoustic perturbations within the burner, while mean amplitude variation is between 5 and 10%.

The linear regime of the response has been assessed through the

comparison against simulations with harmonic excitations at different perturbation amplitude: details can be found in the following sections The system is excited for $0.125s$ with a time step of $5 \cdot 10^{-6}s$ and the time series for the SI post-process are exported each time step.

Concerning the harmonic signals, mono frequency harmonic excitations have been superimposed on the mean flow at the inlet for each frequency of interest and for each level of incoming perturbation. The corresponding flame response has been calculated by taking the Fourier Transform (FFT) of the time histories.

Following the approach proposed by Innocenti [163], the two flames, premixed and pilot, are considered independent in their evolution and behaviour: for each simulation three separated FTFs, a global one, one for the premixed flame and another for the pilot, have been calculated, by integrating the heat release over distinct regions.

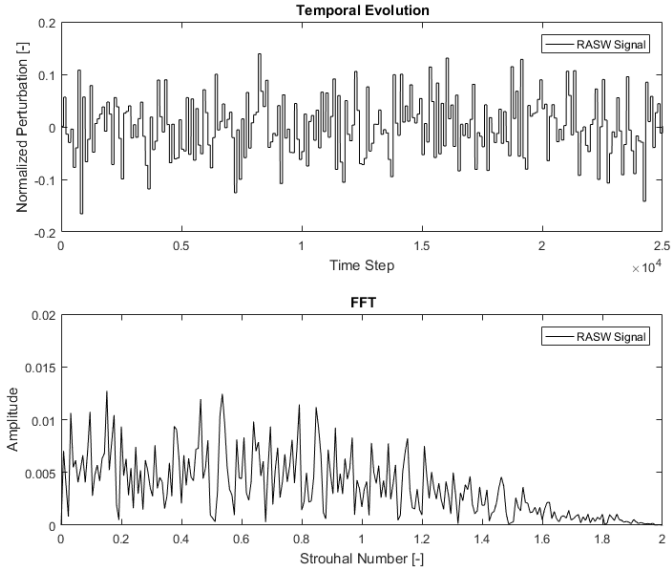

Figure 4.4: RASW signal employed to acoustically force the transient CFD simulation

4.3 CFD Results

4.3.1 Unforced Flames

At first, a brief description of the flame shape and the corresponding flow field are presented in this section. The effects of different operating parameters have been investigated, in particular paying attention to changes in heat release distribution and flame length. In Figure 4.5 the mean results of a URANS simulation for the TP40-L are shown. An approximate number of 3 Flow Trough Time (FTT) are required to initialize the URANS simulation, while a similar time span has been used to average the simulations. As previoulsy said, the burner features a central premixed flame surrounded by discrete pilot injections, while a certain amount of cooling air is injected along the liner walls as can be seen from the progress variable contour (Figure 4.5 top).

Flame stabilization mechanism of the investigated burner is based on the complex aerodynamic flow generated by the two counter-rotating swirlers. As can be seen from the mixture fraction contour (Figure 4.5 middle), the main flame burns a nonuniform mixture: the main fuel is injected close to the burner axis, so that a leaner mixture is present at the higher radii and interacts with the pilots.

Such an injection design has been optimized through numerical [165] and experimental [162] campaigns, showing the highest effectiveness in reducing NOx emissions. Following Innocenti [163], different regions can be defined by means of mixture fraction field: a pilot flame, corresponding to the richest zone, with Z higher than a reference value Z_0, and a premixed flame, with Z lower than Z_0.

By integrating the heat release over these distinct regions the flame response of the pilot and premixed flames can be identified. The difference between premixed and pilot flames can be retrieved also from the volumetric heat release contour in Figure 4.5 bottom: the heat release peaks close to pilot injections are clearly visible, while a longer premixed flame is highlighted.

Concerning pilot flames, in the present burner configuration a stabilization method based on the V-cut shape of the shroud is employed, as shown in [21]: it acts as a sudden area increase, determining the generation of turbulent structures and recirculation zones that drive the hot gases within the reaction zone, igniting the incoming mixture.

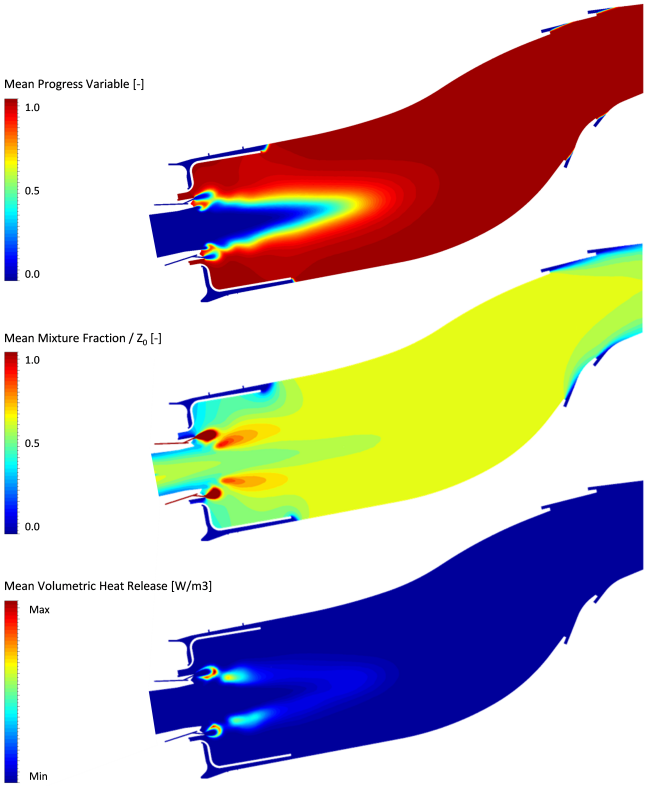

Figure 4.5: Contours of mean field extracted from unforced URANS simulations of TP40-L: progress variable (top), mixture fraction (middle) and volumetric heat release (bottom)

4.3.2 FTF Calculation

After obtained a mean URANS solution, broadband perturbations have been superimposed at the main inlet, in order to calculate the FTFs related to incoming acoustic perturbations. The employed signal, described in Chapter 3 is depicted in Figure 4.4.

In Figure 4.6 the computed FTFs, such as the global one and the FTFs for premix and pilot flame, are reported in terms of amplitude and phase as function of the Strouhal number $St = fL/u_0$), with f the frequency, u_0 the reference velocity and L a characteristic length of the flame. A linear behaviour of the flame is assumed, checking the responses to harmonic signals at different frequencies with an amplitude of 10%. The identified FTFs generally show a good agreement with the harmonic reference responses, excluding the phase plot for the frequencies where flame response is weak, i.e. for $St > 0.8$, in which the System Identification technique is affected by the presence of noise.

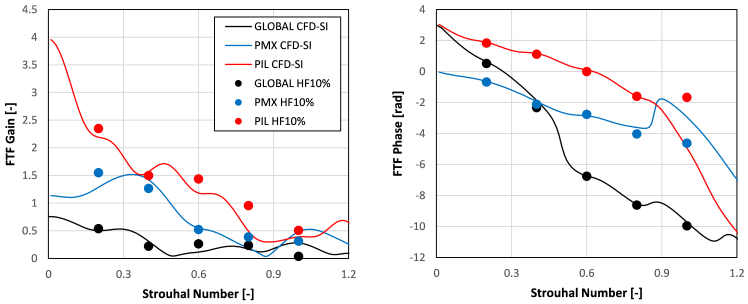

Figure 4.6: Comparison between the FTFs calculated for TP 40-L with broadband (CFD-SI) and harmonic forcing (HF), varying the reference signals for heat release: global or premixed/pilot flame only

After validating the CFD-SI procedure, the FTFs of premixed and pilot flames are firstly analysed. In both cases the FTF amplitude assumes values above unity for a part of the frequency spectrum but with a different trend: for the premix flame, after a peak at around $St = 0.3$, the amplitude decreases and assumes very low values for $St > 0.8$, whereas for the pilot flame the response is globally very high and reduces continuosly in the range between 0 and 0.8 after which it reaches an asymptotic behaviour.

Regarding the phase plots the two flames show a similar time delay, but appear out of phase of a quantities close to π. The response delays appear

close to the acoustic driven time lag, with a slightly shorter time delay associated with the pilot flame. As already observed in [163], mixture fraction fluctuations at the burner exit, which propagates slower at the convective flow speed seem not to affect the pilot dynamic, whereas the time lag of pilot flames relates to a fast response typical of an acoustic propagation of the disturbance. In fact, the part of the main flow that interacts with the pilots is practically air (see i.e. mixture fraction contours in Figure 4.5 middle) so that almost no equivalence ratio fluctuations are present. For this reason, the time delay associated with the pilot flame results slightly lower than the premixed one, due to the shorter distance between the heat release of the flame and the burner exit.

Looking at the FTF calculated with the global heat release a low response is observed within the range of interest, due to the destructive interaction of the two sub-flames. Consequently, the phase plot of the global response shows a higher time delay with respect to the two sub-flames, proving that the dynamics of such a complex flame is not controlled by acoustic phenomena only.

From these observations it can be concluded that the interaction between the responses of premixed and pilot flames can have a strong impact on global flame dynamics: the phase shift between the two FTFs can be conveniently adjusted during the design phases in order to get a destructive interaction, with small changes to the pilot fuel supply lines.

Other criteria to distinguish between premixed and diffusion flames can be adopted, such as the one proposed in [166], once the decoupled analysis has been assessed.

In the following only global flame response will be analysed, in order to obtain the FTFs to be implemented within the Helmholtz solver. Other investigations are required in order to exploit the separated FTFs to study the stability of the combustor and could be the subject of future improvements of the procedure.

4.3.2.1 Linearity Checks

Linearity hypothesis has been verified by performing dedicated simulations with harmonic excitations at different amplitude levels at the frequency where the flame response is about the highest ($St = 0.2$), among those considered in the previous analysis. Results are shown in Figure 4.7 for the three considered flames.

Comparing the calculated responses at different amplitude levels a similar behaviour can be observed for the different flames. Small differences can be retrieved for both gain and phase between the simulations at 10% and 30%, verifying the linearity hypothesis within the adopted amplitude

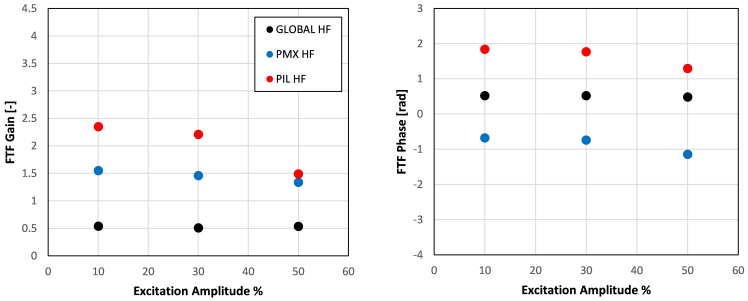

Figure 4.7: Comparison between the flame response calculated with harmonic excitations at different amplitude levels at $St = 0.2$ for TP 40-L, varying the reference signals for heat release: global or premixed/pilot flame only

range: non-linear effects are not significant for the amplitude level of 10% considered in this work. Looking at the highest perturbation ratio (50%), a saturation of the flame response can be seen for the pilot flame only, while the other flames shows a similar response. Greater differences can be found for the phase plot, in particular for the pilot and global flame responses.

4.3.2.2 Sensitivities to the main operating parameters

After validating the proposed procedure on the TP 40-L, several sensitivities have been carried out, with the aim of:

- assess the model capability in catching the instability onset
- get a deeper insight into instability formation mechanisms

At first, a brief description of the differences between the analysed test points in terms of flame shape and mean quantities profiles are presented in this section. The effects of different operating parameters have been investigated, in particular concerning the flame temperature and the fuel flow split between main and pilot injections. In Figure 4.8 the mean progress variable fields of the corresponding unforced URANS simulation for the first six test points are shown.

Starting from the TP 40-L, a reduction of the premixed flame length can be observed both increasing the flame temperature or decreasing the

amount of pilot fuel, due to the increased equivalence ratio of the main flow. In fact, the same total fuel flow rate is employed for all the considered test points and the higher flame temperature is obtained decreasing the air mass flow (see the pressure loss levels reported in Table 4.1).

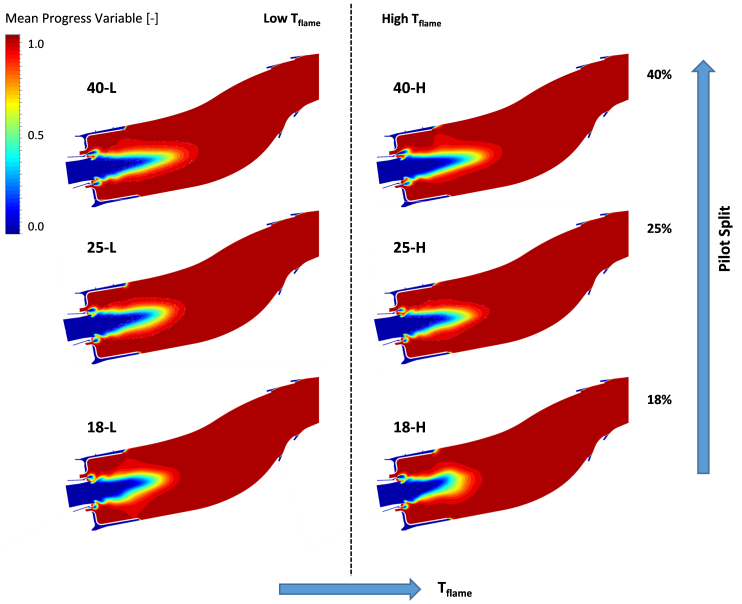

Figure 4.8: Comparison between the contours of mean progress variable extracted from unforced URANS simulations, varying the operating conditions according to Table 4.1

Due to the fact that an higher power density is related to compact flames, for the same thermal power, higher responses are expected for the test points with the highest flame temperature and the lowest pilot split. Moreover, an increased level of dispersion of the incoming perturbation is expected in a longer flame, due to the destructive interactions between different part of the flame. For what stated, smaller amplitudes of the premixed FTF are expected for longer flames.

Concerning the pilot flames, a slight shift upstream is also retrieved for the test points at low pilot split, due to the decreased penetration of the jets. The expected effect of this behaviour on the pilot flame response is a shorter delay with respect to the baseline configuration. These effects

can be better appreciated looking at the mean quantities profiles along the centerline of the burner, as reported in Figure 4.9.

Looking at the mean progress variable profile (left) the different premixed flame lengths can be retrieved: the most compact flame is associated to the TP 18-H, while the longest one is related to the test point with the highest pilot split and the lowest flame temperature (TP 40-L). The same conclusions derive from the analysis of temperature profiles (Figure 4.9 right), where the two employed flame temperature levels are highlighted.

Some differences arise looking at the equivalence ratio of the incoming mixture, as can be seen in Figure 4.9 middle, where the mean mixture fraction profiles are compared each other: for example, even if a richer mixture is present at the burner exit, the flame length corresponding to TP 18-L is longer than TP 25-H, due to the effect of a different flow velocity. This point can be better understood looking at the mean quantities profiles extracted radially at the exit of the burner, as reported in Figure 4.10: the shape of the jet, as well as the different velocities between the test points at low and high flame temperature can be retrieved from the right plot.

As can be seen from the mixture fraction profile (Figure 4.10 left), the main flame burns a nonuniform mixture: the main fuel is injected within the inner swirler, close to the burner axis, so that a leaner mixture is present at the higher radii. At this location, the equivalence ratio of the mixture is insensitive to changes in the operating conditions, as can be seen from the collapse of the curves. It is important to stress that this part of the jet represents the mixture flow that interacts with the pilots.

The same comparisons have been done to assess the effect of the pressure drop along the burner. An additional test point has been considered, named TP 18-LP in Table 4.1, with the same flame temperature and fuel flow split of TP 18-L but with the air flow rate corresponding to the high flame temperature level. Results are shown in Figures 4.11 and 4.12 with respect to the test points with the corresponding pilot fuel split. As expected, the flame shape and the equivalence ratio profiles of the additional test point are equal to TP 18-L, while the velocity field corresponds to TP 18-H.

4.3.2.3 Flame response analysis

In Figure 4.13 the computed FTFs for the test points with pilot fuel split of $25 - 40\%$ are reported in terms of amplitude and phase as function of the Strouhal number. The linear behaviour of the flame has been assessed, checking the responses to harmonic signals at different frequencies, but are not shown for the sake of brevity.

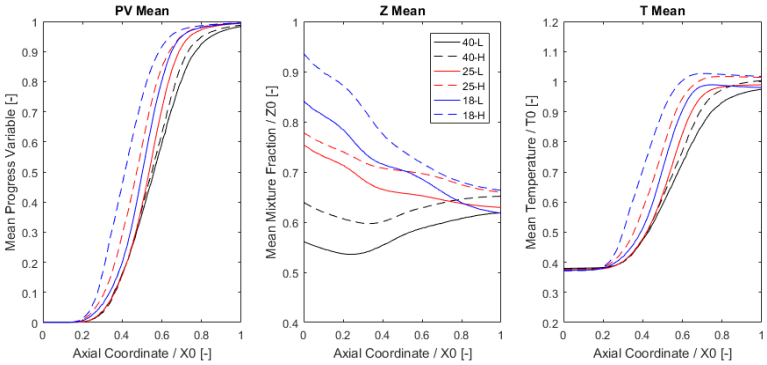

Figure 4.9: Comparison between the profiles of mean progress variable, mixture fraction and temperature extracted on the centerline of the burner from the unforced URANS simulations, varying the flame temperature and the pilot fuel split according to Table 4.1

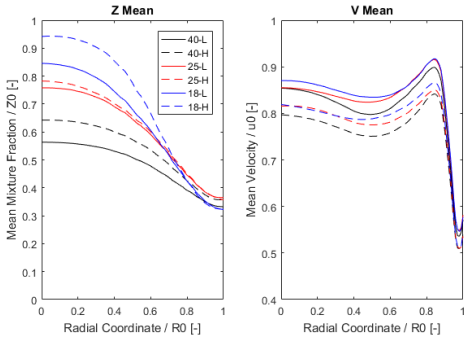

Figure 4.10: Comparison between the profiles of mean mixture fraction and velocity extracted radially at the exit of the burner from the unforced URANS simulations, varying the flame temperature and the pilot fuel split according to Table 4.1

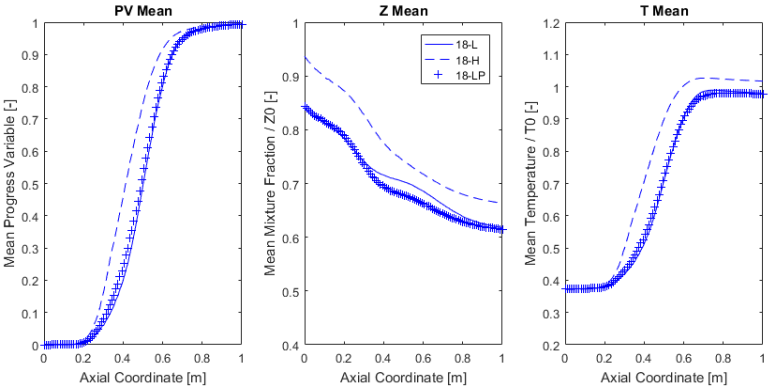

Figure 4.11: Comparison between the profiles of mean progress variable, mixture fraction and temperature extracted on the centerline of the burner from the unforced URANS simulations for the test points with pilot fuel split of 18%

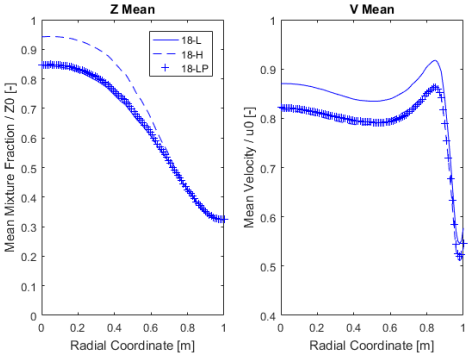

Figure 4.12: Comparison between the profiles of mean mixture fraction and velocity extracted radially at the exit of the burner from the unforced URANS simulations for the test points with pilot fuel split of 18%

The identified FTFs generally show a very low amplitude, as already discussed for the TP 40-L and exhibit a peak at low frequencies, followed by a decreasing amplitude, due to the increasing dispersion of the perturbation.

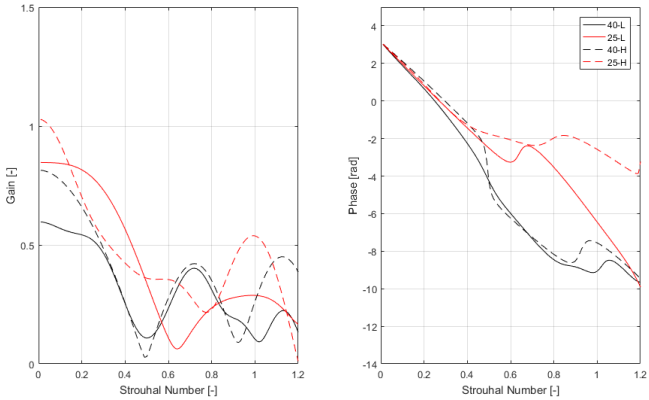

Figure 4.13: Comparison between the calculated FTFs for the test points with pilot fuel split of $25 - 40\%$

Concerning the different operating conditions, an increased value of amplitude is generally retrieved, as expected, for test points with high temperature level, due to the higher power density related to more compact flames. In the same way, decreasing the pilot split from 40% to 25%, an higher gain peak is reached, as the premixed flame shortens. As far as the phase plot is concerned, a constant time lag can be seen in the first part of the spectrum, ascribable to convective propagation of the perturbations, with a slightly higher value of the time delay for the longer flames, due to the additional path required to reach the reaction zone. A different behaviour emerges at higher St: a sudden change in phase slope appear at different frequencies for the investigated configurations. Test points with split 40% exhibit a transition close to $St = 1$, while the ones with split 25% show the same behaviour in the range $St = 0.6 - 0.8$. The phenomenon, already observed in [21], has been ascribed to the complex interaction between pilot and premixed flame. In Figure 4.14 the same comparison is reported for the test points with pilot fuel split of 18%. As far as the amplitude plot is concerned, a different shape of the flame response can be seen for TP 18-H, corresponding to the experimental

unstable condition: a peak at about $St = 0.6$ is present, as well as a generally higher response with respect to the other test points.

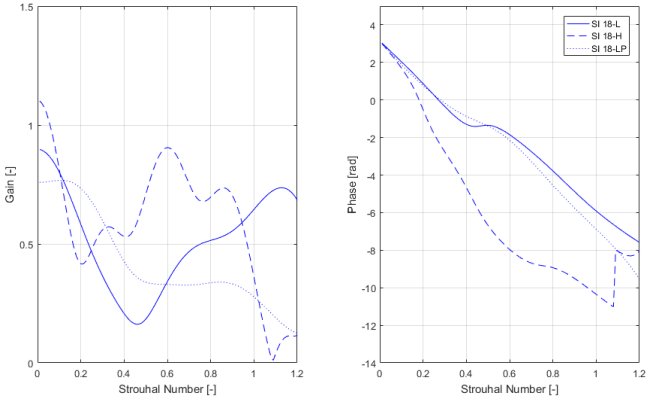

Figure 4.14: Comparison between the calculated FTFs for the test points with pilot fuel split of 18%

Both phase plots of the test points at low temperature show the same constant time lag for the two FTFs, ascribable to convective propagation of the perturbations, while a much higher delay can be retrieved for TP 18-H, despite the fact that the shortest flame is associated to this operating condition. Looking at the FTFs obtained for the premixed and pilot flames separately can give a deeper insight on the calculated flame response. Two test point have been selected, corresponding respectively to the shortest (TP 18-H) and longest flame (TP 40-L), which has been already discussed in Section 4.3.1. Results are shown in Figure 4.15.

Firstly, FTFs calculated by means of CFD-SI technique generally show a good agreement with the harmonic reference responses, in particular regarding the phase plot, further validating the adopted approach. Considering the response of pilot and premixed flame separately at the frequency in which the difference is the highest, i.e. $St = 0.6$, a possible explanation emerges. For TP 40-L, as already discussed in section 4.3.2.1, pilot and premixed responses result out of phase, determining a destructive interaction between the two sub-flames and, consequently, a low global amplitude. Instead, for TP 18-H the shift between the responses is about 2π at $St = 0.6$ and the resultant global gain is much closer to the premixed one.

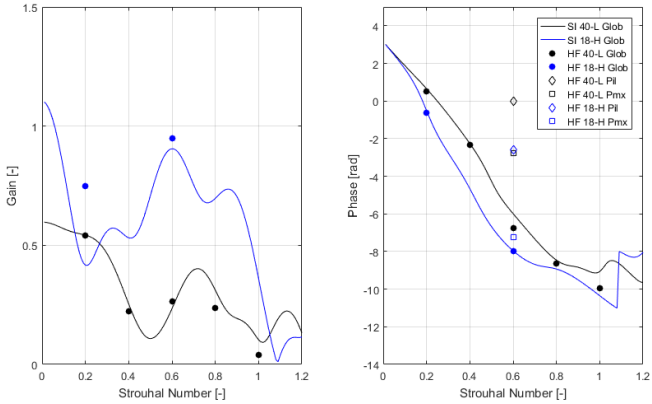

Figure 4.15: Comparison between the calculated FTFs for the test points 40-L and 18-H with both System Identification techniques (SI) and harmonic forcing (HF)

From these observations it can be concluded that the interaction between the two sub-flames can have a strong impact on global flame dynamics: the design of the pilot fuel injection could be conveniently optimized in order to obtain a destructive interaction between the two sub-flames over the whole range of operating conditions of interest.

4.4 FEM modelling and Numerical Setup

Once obtained the responses for the investigated test points, the computed FTFs have been implemented in a 3D FEM model of the BHGE full-annular combustor. The eigenvalue problem is solved in this work with the acoustic module of COMSOL Multiphysics [157] by means of an iterative linearisation procedure based on a variant of the Arnoldi algorithm [158]. The solution consists in determining the complex resonant frequencies ω of the combustor, whose real part represents the frequency of oscillations and the imaginary one characterizes the stability of a mode. Following the notation introduced in Chapter 3 an unstable mode has a negative imaginary part meaning a growing fluctuation amplitude.

4.4.1 Bloch-Wave Periodicity

A boundary condition for rotational periodicity based on Bloch-Wave theory has been implemented in COMSOL Multiphysics, as described in Chapter 3. This condition allows to consider only a sector of the full-annular geometry, determining a significant reduction in computational time, given the same accuracy as a full domain computation and making the model suitable for optimization studies of the chamber. Following this approach a different eigenvalue problem has to be solved for each Bloch wavenumber of interest, such as, for practical configurations, only the first wavenumbers, corresponding to the lower frequencies. The simplified FEM model, together with the full-annular geometry of the chamber, is shown in Figure 5.9. The smallest geometrical feautures, such as the fuel lines, the swirler vanes, the cooling injection holes have been removed, after checking their influence on the acoustics of the system. The main cavities, instead, are considered, as well as the connections among them, as can be seen in Figure 5.9.

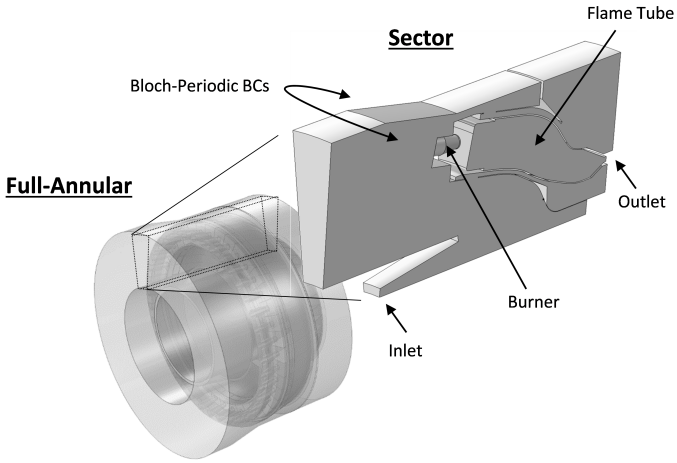

Figure 4.16: FEM model of the investigated BHGE combustor: full-annular geometry (left) and simplified sector model (right)

The computational mesh counts about $1.1 \cdot 10^5$ tetrahedral elements for the sector model, while $4.3 \cdot 10^6$ elements are required for the full annular geometry, counting 39 sectors. Both the computational grids have been employed for validation purposes and are shown in Figure 6.9. The

sizing of the mesh has been chosen considering frequencies far above the range of interest for the combustor.

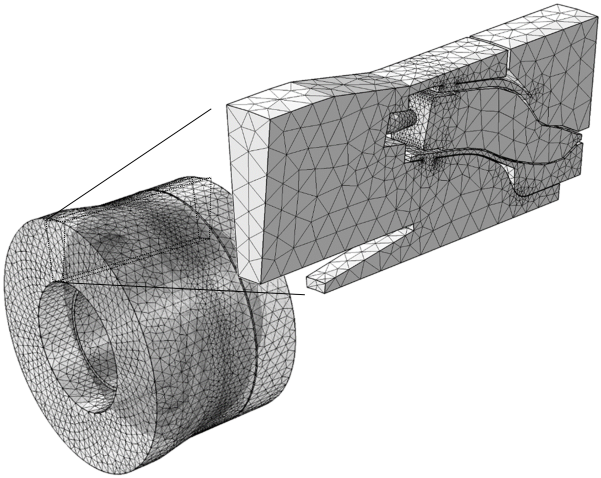

Figure 4.17: Computational grids of the investigated combustor: full-annular geometry (left) and simplified sector model (right)

4.4.2 Boundary conditions and source term modelling

Concerning the acoustic boundary conditions, a plenum condition has been applied at the inlet of the domain, simulating the compressor dicharge whereas a chocked outlet is assumed at the outlet, which represents the turbine inlet section. In order to give a more physical representation of the combustor, the temperature distribution is imported into the 3D FEM model from the CFD results. The density and the speed of sound are consequentely calculated and their distributions are shown in Figure 4.18 top and middle.

The source term of equation 3.51 has been applied within the flame region only, following the approach used in [163]: after importing the PFR field calculated from CFD a flame-identifying function, which is zero outside the flame, is defined and used as a weighting function to apply a non-uniform distribution of the source term (an example can be found in Figure 4.18 bottom). Following this approach the flame shape is accurately described within the Helmholtz solver and the differences

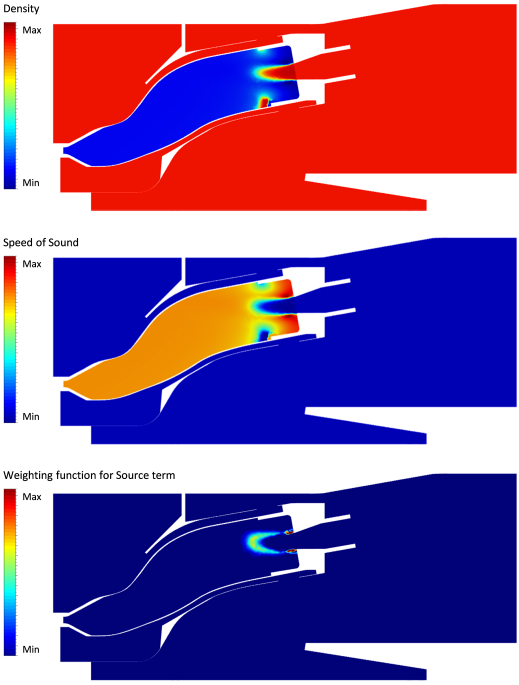

Figure 4.18: Fields of density (top), speed of sound (middle) and source term weighting function (bottom) as calculated from CFD data imported in COMSOL

between the operating conditions (i.e. the flame length and the relative weigth between pilot and premixed flame) are introduced into the analysis.

4.5 Linear Stability Analysis

At first, the results of the adopted simplified sector domain has been compared against the ones of the full-annular chamber, in order to validate the Bloch-Wave approach. The first eigenfrequencies, calculated with the different approaches, are reported in Figure 4.19.

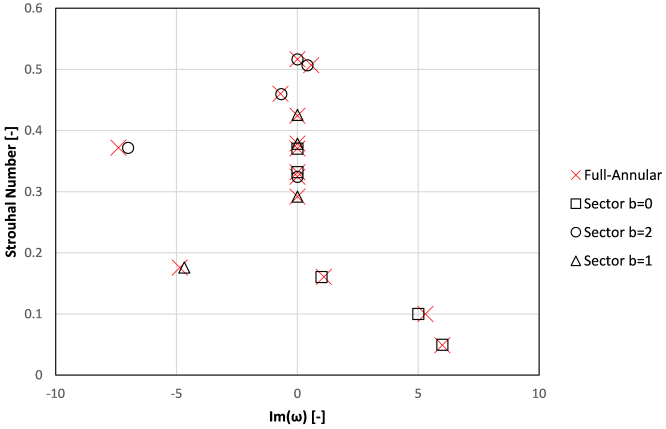

Figure 4.19: Comparison between the eigenfrequencies of the sector domain with Bloch-Wave periodicity conditions and the full-annular chamber.

As can be seen the accuracy of the simplified model is assessed by the comparison between frequencies and growth rates. The significant reduction in computational time, given the same accuracy as a full domain computation, makes the model suitable for the sensitivities analysis presented in the following section.

The reliability of the numerical procedure to study the thermo-acoustic stability have been assessed through the comparison against full-annular experimental results performed by Baker Hughes GE. Analysis was focussed on the second azimuthal mode of the combustion chamber, for which large amplitude pressure fluctuations were measured reducing the amount of pilot fuel and increasing the overall flame temperature. The

shape of the unstable mode, as retrieved from the full-annular calculation, is shown in Figure 4.20 .

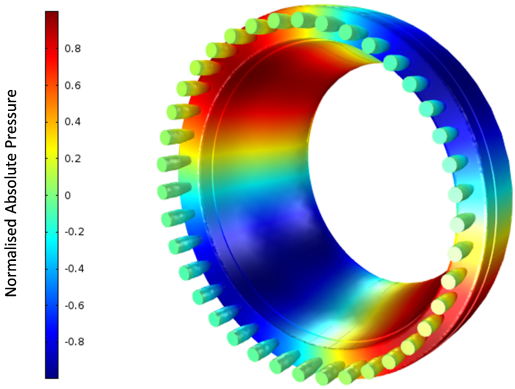

Figure 4.20: Normalised total pressure plotted over the flame tube surfaces for the second azimuthal mode of the combustion chamber

After validating the employed numerical setup the FTFs calculated by means of CFD-SI technique have been exploited to perform linear stability analysis of the full-annular combustor. Numerical results have been compared against experimental findings, in terms of stability of the second azimuthal mode of the combustion chamber: large amplitude pressure fluctuations were measured for the TP 18-H only, characterized by high flame temperature and reduced pilot split.

As can be seen in 4.21, the numerical model results able to determine the stability of all the analysed test points: only the TP 18-H has a positive growth rate whereas the other test points result stable. The frequency of the predicted instability has been also compared to the experimental measurements, finding a difference of about 6%.

Regarding the different sensitivities, for all the investigated split configurations, a higher growth rate is obtained increasing the flame temperature, in line with the experimental observations. Also reducing the amount of pilot fuel an increase in growth rate is observed, varying the different temperature levels.

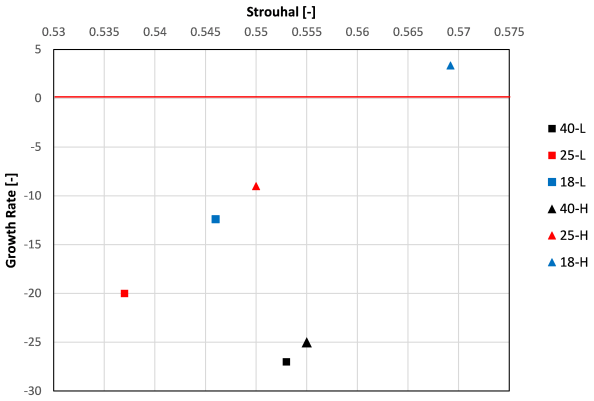

Figure 4.21: Results of linear stability analysis on the simplified sector model of the chamber, varying the FTFs calculated by means of CFD-SI

4.6 Concluding remarks

URANS simulation coupled with System Identification techniques have been used to numerically study the dynamics of a lean-premixed full-annular combustor for heavy-duty applications. Such an approach have been exploited to perform several sensitivities to the main operating parameters such as flame temperature and fuel split.

The main features of the flame have been investigated, exploiting a decoupled approach to consider the behaviour of the two sub-flames and to provide explanations of the observed trends. From these observations it can be concluded that the interaction between the responses of premixed and pilot flames can have a strong impact on global flame dynamics and can be exploited to conveniently modify the thermo-acoustic behaviour of the system in the critical operating conditions.

The calculated FTFs have been implemented in a 3D FEM model of the chamber, in order to perform linear stability analysis and to validate the numerical approach against the available experimental results. A boundary condition for rotational periodicity based on Bloch-Wave theory has been also implemented in COMSOL Multiphysics and validated against full-annular chamber simulation, allowing a significant reduction in computational time.

The reliability of the numerical procedure has been assessed through

the comparison against full-annular experimental results performed by Baker Hughes GE, highlighting the capability of the proposed methodology to accurately predict the instability of the system and the effects of the different operating parameters.

However, in order to predict the behaviour of the system and the amplitude of pressure oscillations, the non-linear behaviour of the system should be modelled. In the following sections advanced numerical modelling of complex flame dynamics phenomena will be developed and validated on simple lab-scale flames. The work allows to assess the capability of such procedure, in the perspective of future application on real technically-premixed flame for gas turbine applications.

Chapter 5

Numerical Analysis of the Nonlinear Dynamic Response of a Lean Premixed Flame

In this chapter a weakly nonlinear thermo-acoustic stability analysis is presented. The identification startegy and the numerical models described in the previous chapters are now applied to a lean premixed swirl-stabilized combustor, experimentally studied at Technische Universitat of Berlin (TUB), for validation purposes. Availability of detailed experimental measurements for this setup, in particular concerning the Flame Describing Function allowed an exhaustive comparison study.

In the first part of the chapter, after a brief description of the experimental test case and the available measurements, the CFD results are presented. Considering the effects of both flame stretch and heat loss into the FGM framework, a numerical setup able to accurately reproduce the stable flame configuration is presented. Acoustically excited transient simulation are then performed, in order to calculate the Burner Describing Function (BDF) and the Flame Describing Function (FDF).

Once obtained the FDF from numerical simulations, it can be used as input for weakly nonlinear thermo-acoustic analysis, in order to predict the frequencies and the amplitudes of pressure oscillations. A 3D FEM model of the combustor has been used and acoustic analysis have been carried out at different excitation levels. Finally, results have been compared against experimental measurements and self-excited LES simulations, showing the capability of the simulations to catch the instability observed during the measurements.

5.1 TUB-MB Combustor: Test Case Description

The test case under consideration is an atmospheric swirl stabilized lean-burn flame, experimentally studied by Schimek et al. [125]. A schematic view of the rig is shown in Figure 5.1, left.

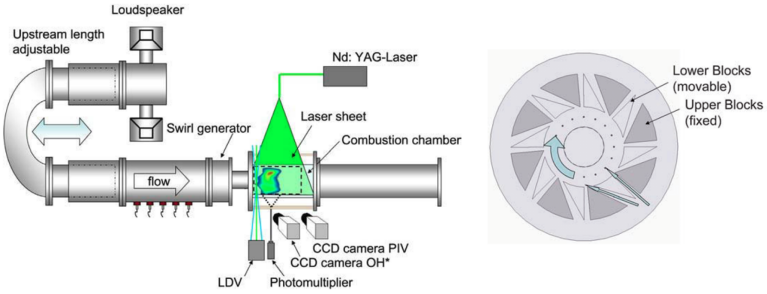

Figure 5.1: Schematic representation of the test rig (left) with details of the swirler (right).

It was originally used to study both perfectly and partially-premixed configuration, but only the fully premixed mode has been considered in this work. The combustor consists of an inlet plenum, a swirl generator, an annular premixer duct and a cylindrical combustion chamber and burns a natural gas/air mixture at ambient temperature and $\phi = 0.7$. The injection of natural gas occurs within the upstream plenum, so that a homogeneous mixing is ensured at the burner exit.

The swirler concept (Figure 5.1 right) was based on the movable block configuration [167], which allows for tuning of the swirl number S_N between 0 and 2, according to the definition given in [168]. In this work only the condition corresponding to $S_N = 0.7$ has been considered. To the authors' knowledge, such configuration is numerically investigated here for the first time.

The premixer consists of a 0.171 m long annular duct with an external diameter $D_e = 55\ mm$ and a centred cylindrical bluff body of diameter $D_b = 27.5\ mm$ and is followed by a 1.5 m long cylindrical combustion chamber. The main dimensions of the test rig and the operating conditions are summarized in Table 5.1.

During FDF measurements, an orifice is mounted at the downstream end of the combustion chamber with the aim of preventing the reflection of acoustic waves and the onset of self-excited thermo-acoustic instabilities.

Combustion chamber length [m]	1.5
Combustion chamber diameter [m]	0.2
Premixer Hydraulic Diameter [m]	0.0275
Reynolds Number [-]	37000
Inlet Temperature [°C]	20

Table 5.1: Investigated configuration parameters and operating conditions.

The desired level of acoustic forcing was provided by 4 loudspeakers mounted in the upstream duct with variable length. Such a configuration allows to modify the upstream impedance of the combustor at runtime, exploiting the resonance of the upstream duct to amplify the forcing capability up to 100% of the mean flow velocity.

Detailed experimental measurements are available for this setup, allowing an exhaustive comparison study: a detailed characterization of the isothermal flow field can be found in [25], whereas Schimek et al. [125] measured both the transfer functions of the burner, making possible to calculate the axial and the tangential velocity fluctuations at the burner exit based on the acoustic field upstream, and the FDF, with excitation amplitude up to 60% of the mean flow velocity for the investigated configuration.

5.2 Numerical Setup

The spatially-filtered compressible Navier-Stokes equations have been solved with the pressure-based code ANSYS Fluent v17.1. The computational domain includes the entire combustion chamber, the burner and part of the upstream duct, in order to recreate a homogeneous incoming flow and allow a natural generation of turbulence through the swirler.

The computational grid is shown in Figure 5.2.

It consists of approximately 7 million polyhedral cells: at first an hybrid mesh of about 29 million tetrahedral cells with five layers of prisms adjacent to solid walls was created with ANSYS Meshing and then it was processed with Fluent to generate polyhedral cells. The characteristic size of polyhedral cells is about 1 mm in the burner region and 2 mm in the rest of the chamber, with a refinement of 0.5 mm within the swirler passages.

As far as the mixture properties are concerned, fourth order polynomial functions of temperature are introduced for thermal conductivity, specific heat and viscosity. An ambient pressure condition has been imposed at

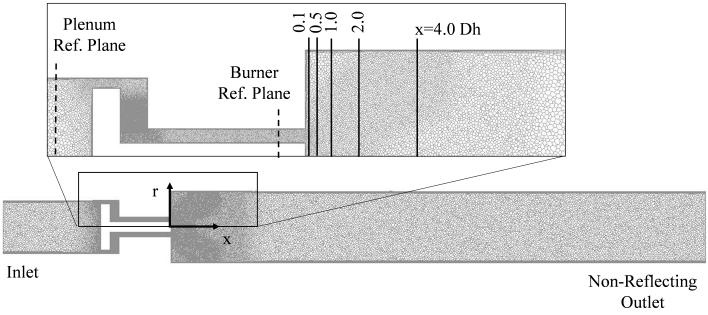

Figure 5.2: Computational grid for LES simulation and measurement planes.

the outlet, whereas the walls of the combustor are considered isothermal, at the constant temperature of 800 K, following the setup used in [121]. A constant temperature of 293 K has been imposed at the inlet section, together with a constant velocity profile in order to match the Reynolds number of Table 1, based on the hydraulic diameter D_h of the premixer.

During the transfer function calculations, a Non-Reflecting Boundary Condition (NRBC) has been imposed at the outlet section to prevent resonances inside the domain, which could eventually alter and deteriorate the FDF identification.

Concerning the numerical setup, a PISO algorithm has been adopted and second order upwind schemes for spatial discretization and a bounded second order implicit formulation for time have been imposed. A Courant number below 0.7 is assured by the adopted time step of $3 \cdot 10^{-6} s$.

5.2.1 Turbulence and Combustion Modelling

The LES sub-grid turbulence has been modelled with the Dynamic Smagorinsky-Lilly formulation to allow an adaptive estimation of Smagorinsky constant in time and space [137]. Assuming that the main turbulent structures are produced when crossing the swirler geometry, no artificial turbulence has been imposed at the inlet of the domain.

As far as the combustion modelling is concerned, to reproduce the complex topology and the stabilization mechanism shown by the flame, approaches characterized by a detailed description of the kinetic mechanisms are required. To this end, the Flamelet Generated Manifold (FGM) model, where a pre-computed laminar flamelet solution is integrated

through a pre-defined probability density function (PDF) to account for turbulence effects, has proved to be capable of accurately describing the flame evolution since it can locally consider finite rate and non-equilibrium [169] and has been successfully applied in similar configurations [170].

A premixed flamelet behavior has been considered and flamelet equations have been solved using the dedicated solver integrated in ANSYS Fluent and exploiting the Gas Research Institute reaction mechanism GRI Mech 3.0 for methane, with 325 reactions and 53 species. Variances of progress variable and mixture fraction have been modelled respectively through a transport equation and an algebraic closure. Finally, the source term of progress variable has been modelled in the present work using both finite rate (FR) formulation and turbulent flame speed (TFC) closures.

The correct account for high strain levels is mandatory in high Reynolds lean combustion modelling, since the quenching effects due to flame front distortion are expected to govern flame parameters like shape, emissions and dynamics. It is thus very important that such effects are included in combustion models.

Concerning TFC, the same extended model that takes into account the effects of flame stretch and heat loss described in 3 has been used. The capability of the extended TFC model in accurately reproducing the nonlinear flame dynamics are presented in the following sections.

5.2.2 Identification Strategies

After obtained a LES solution, mono frequency harmonic excitations have been imposed at the inlet for each frequency of interest and for each level of incoming perturbation. In order to calculate the Burner Describing Functions (BDF), i.e. the transfer function of the burner at different excitation amplitudes, two reference locations (see Figure 5.2 for the location of reference planes), upstream and downstream the swirl generator have been used to record the time histories of velocity fluctuations: the axial U' and the tangential velocity V' fluctuations at the burner exit have been related to the incoming perturbations, within the plenum, through an axial and a tangential BDF respectively. Thus, the BDFs for each frequency of interest and for each level of incoming perturbation is calculated by taking the Fourier Transform (FFT) of the recorderd time histories at the downstream (ds) and upstream (us) reference planes, normalized by means of their mean values, according to:

$$Axial\ BDF\left(\omega,\left|u'\right|\right)=\frac{FFT\left(\frac{U'_{ds}\left(\omega,\left|u'\right|\right)}{\overline{U}_{ds}}\right)}{FFT\left(\frac{U'_{us}\left(\omega,\left|u'\right|\right)}{\overline{U}_{us}}\right)} \tag{5.1}$$

$$Tangential\ BDF\left(\omega,\left|u'\right|\right)=\frac{FFT\left(\frac{V'_{ds}\left(\omega,\left|u'\right|\right)}{\overline{V}_{ds}}\right)}{FFT\left(\frac{U'_{us}\left(\omega,\left|u'\right|\right)}{\overline{U}_{us}}\right)} \tag{5.2}$$

In the same way, to obtain the FDF, time series of acoustic velocity fluctuations at the burner mouth and the global heat release by the flame have been recorded during the same transient CFD runs used to determine the BDFs.

After normalizing the velocity and heat release fluctuation by means of their mean values, the FDFs for each frequency of interest and for each level of incoming perturbation have been calculated, exploiting the Fourier Transform (FFT) of the time histories:

$$FDF\left(\omega,\left|u'\right|\right)=\frac{FFT\left(\frac{Q'\left(\omega,\left|u'\right|\right)}{\overline{Q}}\right)}{FFT\left(\frac{U'\left(\omega,\left|u'\right|\right)}{\overline{U}}\right)} \tag{5.3}$$

5.3 CFD Results

At first, the numerical setup has been validated against unforced non-reacting [25] and reacting experimental measurements [125]. After obtained a statistically-stable LES solution, harmonic perturbations have been imposed in order to calculate the BDFs and the FDF.

Then, the computed FDF has been implemented in a 3D Helmholtz solver and the results of weakly nonlinear acoustic analysis have been compared against experimental measurements and self-excited LES simulations.

5.3.1 Non-reacting flow field

In Figure 5.3 the comparison of the calculated flow field against experimental measurements can be seen. The comparison of the mean axial velocity profiles, extracted at different axial positions along the combustion chamber (see Figure 5.2 for the position of reference planes),

can be observed. Both the axial coordinate and the mean flow component have been normalized by the hydraulic diameter of the premixer D_h and the bulk velocity U_0 respectively.

The predicted results generally show an excellent agreement with the measured profiles. The position and the magnitude of the peak velocities result well caught, as well as the location of the inner recirculation zone that results slightly underpredicted only in the upstream reference plane.

The mean turbulence intensity has been compared as well: results are shown in Figure 5.4 and show a general agreement in terms of magnitude and position of the high turbulence regions, located in the inner shear layer, except for a slight overprediction in the downstream plane.

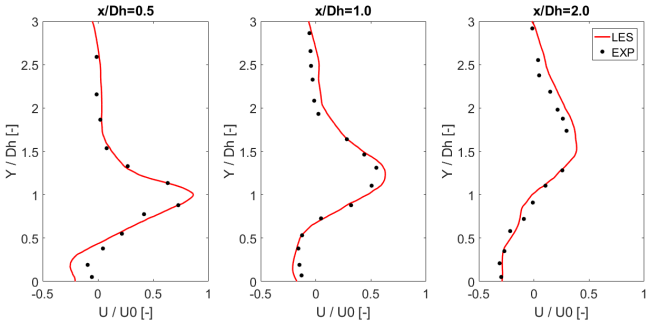

Figure 5.3: Comparison of predicted mean axial velocity against PIV measurements [25].

5.3.2 Burner Describing Functions calculation

The BDFs calculation allows for a complete characterization of the response of the burner, making possible to calculate the axial and the tangential velocity fluctuations at the burner exit based on the acoustic field upstream. In order to validate the numerical setup and the burner modelling, in particular for high amplitude perturbation levels, the calculated BDFs have been compared to the experimental measurements.

After obtained a statistically-stable LES solution, mono frequency harmonic excitations have been superimposed to the inlet velocity boundary condition for each frequency of interest. Since only small dependence of the BDFs on excitation amplitude was seen during the experimental measurements [125], only the response corresponding to acoustic velocity fluctuation at the burner outlet of 10% of the mean value will be shown

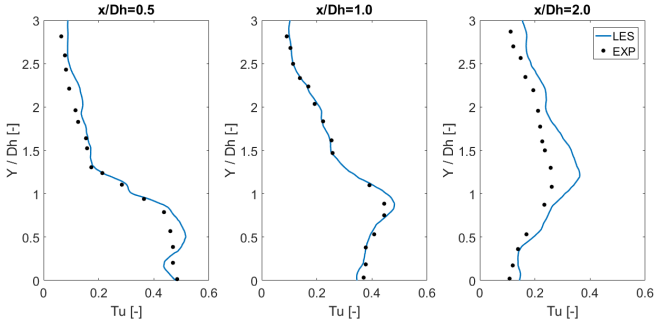

Figure 5.4: Comparison of predicted mean turbulence intensity against PIV measurements [25].

in the following. In CFD calculations, the level of the superimposed perturbation has been chosen in order to get the desired level of acoustic velocity fluctuation at the burner outlet: the upstream excitation amplitude results significantly higher, close to 100% of the mean flow for the high frequency range, meaning that part of the excitation is reflected or dissipated within the swirler.

To obtain the BDFs, time series of the velocity upstream and downstream of the swirler have been recorded during the transient CFD runs. At the burner exit, both axial and velocity fluctuations have been recorded (see Figure 5.2 for the position of reference planes).

Concerning the axial velocity fluctuations, the comparison of measured [125] and calculated BDF is shown in Figure 5.5. The filled markers represent the axial BDF: the swirler cannot be considered acoustically transparent, since the magnitude is generally very low and, for frequencies higher than 200 Hz, less than 10% of the incoming acoustic perturbation reach the combustion chamber as axial fluctuations.

The phase of the BDF decreases continuously, corresponding to a constant time delays of about 2.5 ms. There is a general good agreement between predicted and measured BDF for both the gain and the phase all over the investigated frequency range.

The same comparison is shown for the tangential BDF (white markers). The gain of the function decreases up to 150 Hz and results one order of magnitude lower than the axial BDF for higher frequencies [125]. The phase plot shows a constant time delay of about 6 ms, higher than the axial BDF and corresponding to the convective time from the upstream duct to the burner exit. Both the predicted gain and phase show a good

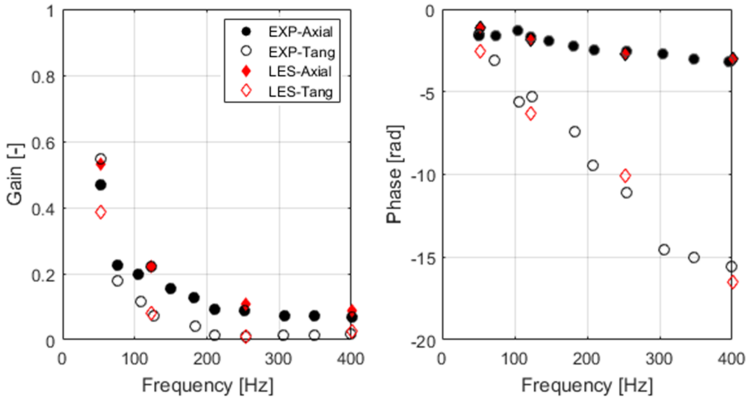

Figure 5.5: Comparison of measured and calculated Axial BDF and Tangential BDF for perturbation amplitude of $\frac{u'}{u_0} = 10\%$.

agreement with the measured one, except for a slight underprediction of the gain at the lowest frequency.

5.3.3 Unforced Flame

In order to validate the combustion modelling, the unforced reacting flow solution has been compared to the experimental data. Mean LES results with the closures available in Fluent [139] for the progress variable source term, i.e finite rate and turbulence flame speed, are shown in the central part of Figure 5.6.

The heat release distribution from OH*-chemiluminescence (first column) and LES have been compared. A black isoline, corresponding to the experimental normalized heat release equal to 0.3 has been superimposed, in order to highlight the heat source location.

With both the closures, FGM-FR and FGM-TFC, there is a strong overestimation of flame reactivity in the outer shear layer and at the premixer exit. In fact, the flame stabilizes with significant reaction rates in both the external and the internal shear layers, resulting in a "M-shaped" flame, whereas the real flame is a "V-shaped".

Especially with TFC, the peak in heat release distribution occurs far upstream than the experimental measurements. The overestimation

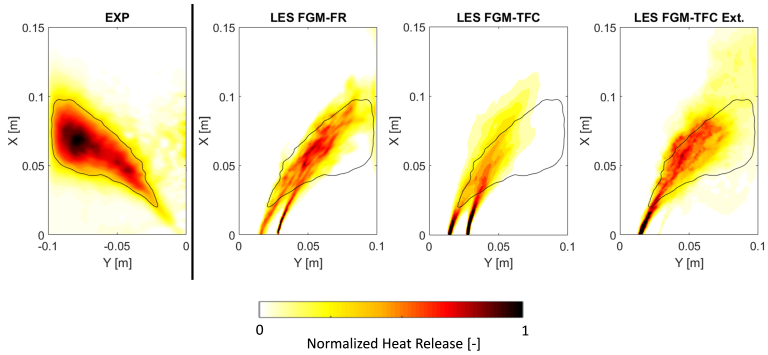

Figure 5.6: Comparison of predicted and measured heat release distribution, varying the progress variable source term closure for LES FGM model.

in flame reactivity leads to an incorrect prediction of the recirculation zone location and magnitude. In particular, TFC overestimates the core velocity of the swirled jet which leads to a lower opening angle with respect to measurements.

In the last column of Figure 5.6 the results of the extended TFC model are shown: the account for flame stretch effects, in particular within the high turbulence regions close to the shear layers, reduces the reaction rates and improves the flame description. The reactivity of the flame in the outer shear layer is lowered and the flame appears as "V-shaped", even if a high reactivity zone is still present at the premixer exit.

Concerning the flow field, the location and magnitude of the recirculation zones are improved, resulting similar to the experimental one, whereas the opening angle of the swirling jet is slightly underestimated.

Mean axial velocity profiles at different axial positions from experiment and LES simulations are shown in Figure 5.7 for the extended TFC model (see Figure 5.2 for the position of reference planes). The calculated profiles are generally in agreement with the measured ones, in particular concerning the magnitude of the maximum of axial velocity, whereas the spread of the swirling jet results slightly underpredicted. Also the recirculating flow is well caught by the model, even if a slight underprediction occurs at the downstream planes.

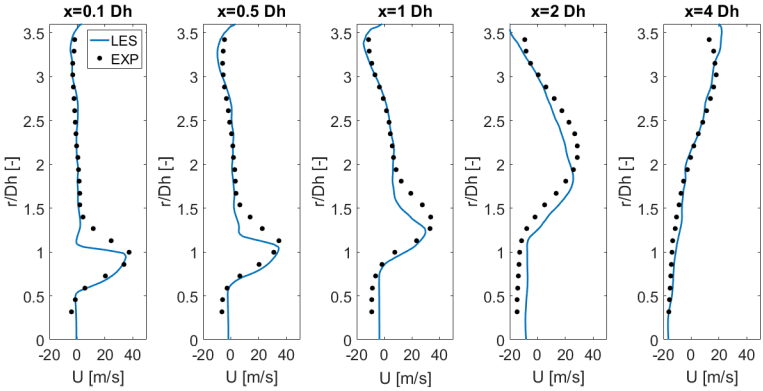

Figure 5.7: Mean axial velocity profiles from experiment and simulation.

5.3.4 Flame Describing Function calculation

After validated the stable flame LES solution with the extended TFC model, mono frequency harmonic excitations have been imposed at the inlet for each frequency of interest and for each level of incoming perturbation.

The FDF is determined according to equation 5.3 for each harmonic excitation. Measurement data are available, for the present configuration, for 7 different excitation amplitudes, as summarized in Table 5.2, together with the corresponding LES runs.

Due to the high computational costs, LES simulations have been performed only at 54, 123, 254 and 400 Hz and for a limited number of excitation levels. Calculations have been performed on at least 8 periods of oscillation, in order to obtain a reliable Fourier Transform of the signals.

Exp. [125]	0.05	0.10	0.15	0.25	0.35	0.45	0.60
LES	0.05	/	0.15	/	0.35	/	/

Table 5.2: Investigated excitation amplitudes.

In Figure 5.8 the comparison of the calculated and measured FDFs can be seen. The calculated FDFs are generally in agreement with the measured ones.

The magnitude of the response is accurately reconstructed within the

whole frequency range, despite a slightly underprediction at 254 Hz, where the FDF peaks. The shape of the gain is properly captured as well as the saturation of the response between 123 and 400 Hz: for each investigated frequency, there is a decrease in the magnitude of the response at high forcing levels, both in simulations and experiments, due to the saturation of flow instabilities, as pointed out in [171].

Concerning the phase, there is an approximately linear decrease with frequency, which indicates a constant time delay of the flame response of about 4.4 ms. There is an excellent agreement with the measurements, and the phase of the response appears to be not dependent on the forcing amplitudes, both in simulations and experiments.

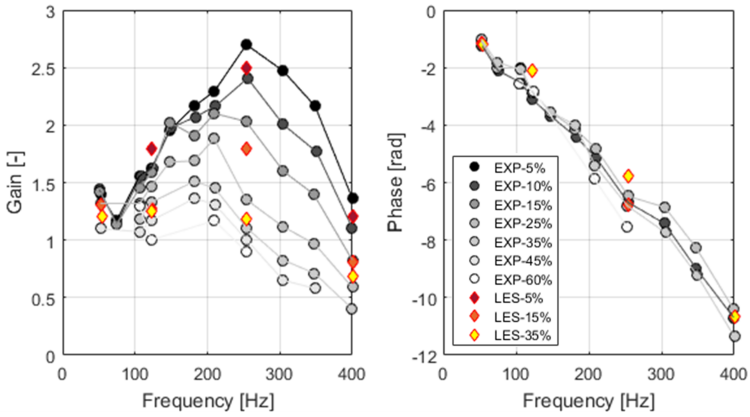

Figure 5.8: Comparison of measured and calculated FDF.

5.4 Stability Analysis

Coupling an acoustic solver with the unsteady heat release rate characterized via experimental or numerical techniques with acoustic forcing is a common approach to numerically study thermo-acoustic systems. An alternative is the self-excited approach, where the flame itself interacts with the acoustics of the chamber within the CFD simulation.

Self-excited instabilities have been suppressed during the measurements of BDF and FDF by employing an orifice at the end of the chamber,

in order to prevent the reflection of the acoustic waves towards the reaction zone. The effect on the outlet acoustic boundary condition was significant: after removing the orifice an instability occured at about 131 Hz for the investigated configuration.

In order to verify the capability of the FDF coupled with a 3D acoustic model of the chamber in predicting such unstable behaviour, a weakly nonlinear stability analysis has been carried out. The onset and the amplitude of the oscillations have been predicted, exploiting both the measured and the calculated flame response.

To further validate the numerical setup used for FDF calculations, a LES simulation without forcing has been carried out and the predicted unstable frequency and limit cycle have been compared to those calculated with the FDF. Both numerical predictions are then compared to experimental data.

5.4.1 Weakly Nonlinear Analysis

A Finite Element Model (FEM) of the combustor is generated in COMSOL Multyphysics [172], as shown in Figure 5.9. The upstream plenum, the swirl generator and the combustion chamber are included in the numerical domain.

The sizing of the mesh has been chosen considering frequencies up to 2 kHz. The inhomogeneous Helmholtz equation is solved in the frequency domain for different levels of the excitation amplitude.

In order to give a more physical representation of the combustor, the temperature distribution has been interpolated from CFD results and density and speed of sound are consequently calculated. The source term of the inhomogeneous Helmholtz equation has been applied within the flame region only, following the approach used in [163], based on the PFR field calculated by means of CFD (see Figure 5.9).

A weakly nonlinear approach is used, considering the nonlinear problem as a perturbation of a linear one, thus fixing a perturbation ratio u'/u_0 and linearizing the FDF into a FTF for each level of the acoustic perturbation. Both the measured and the calculated FDF have been used for the analysis. Two different boundary conditions have been used for the outlet section, in order to mimic the configurations with and without the orifice (see [173] for details), whereas the other surfaces have been treated as rigid walls.

When the open end outlet boundary condition is imposed, one unstable mode is detected for both the FDFs in the range 0-400 Hz, where the data are available. The unstable frequency is predicted in the range 137-140 Hz, as shown in Figure 5.10, where the trajectories in the frequency-growth

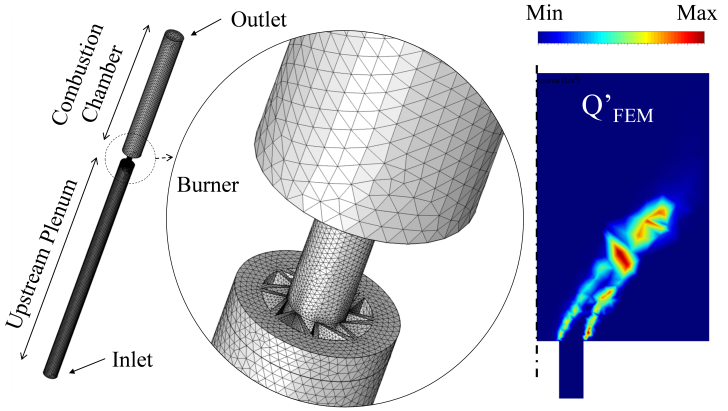

Figure 5.9: FEM model of the combustor (left) with heat release location highlighted (right).

rate plane, coloured by the perturbation ratio u'/u_0, are depicted. A slight decrease of the frequency of the mode with the perturbation ratio can be observed in both the curves, approaching the resonant mode of the configuration without heat release ($q' = 0$) at 133 Hz. Figure 5.8 shows that increasing u'/u_0 a drop of the FDF gain occurs and the magnitude of the source term decreases, mitigating the effects of the unsteady heat release.

Concerning the growth rate, defined as $GR = -Im(\omega)$, there is a monotonic decrease with the excitation amplitude, due to the observed saturation of the flame response. The agreement between the results obtained with different FDFs is good, except for a slight underprediction of the unstable frequency (about 2%) for the calculated FDF.

With the aim of estimating the amplitude of the corresponding limit cycle, the internal damping rate of the system should be considered. Following the method proposed by [24] and described in Chapter 3, an estimate has been done, exploiting the spectra obtained with LES simulations in non-reacting conditions: an internal damping rate of 23 is estimated from the response sharpness of the system to an external perturbation. Considering the trajectories depicted in Figure 5.10, the onset of the instability can be retrieved: initially, for small perturbation amplitudes u'/u_0, the coupling between acoustics and combustion determines a growth of the oscillations. Considering the acoustic damping of the

system, a limit cycle is reached when the growth rate equals the estimated internal damping rate (see Figure 5.10), leading to a velocity fluctuation amplitude u'/u_0 of about 0.35 with both the measured and the calculated FDF (see Figure 5.10 right). Considering the corresponding gain of the FDF at the unstable frequency, the amplitude of the limit cycle associated to heat release fluctuations results $Q'/Q_0 = 0.59$.

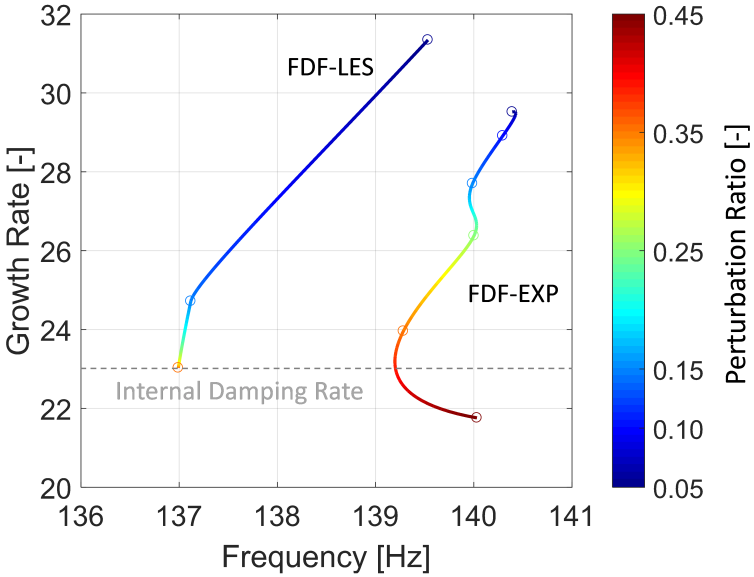

Figure 5.10: Dynamical trajectories in the Frequency-Growth Rate plane of the unstable mode predicted from weakly nonlinear stability for the measured and calculated FDF, colored by the perturbation ratio u'/u_0. Circular marks correspond to the investigated perturbation ratio levels. Grey dotted line represents the internal damping rate estimation.

5.4.2 Self-Excited LES Simulation

The same CFD setup employed for forced response calculations has been used also for the self-excited simulation, removing the non-reflecting boundary condition at the outlet section.

The LES simulation has been performed for 190 ms and highlights an

unstable frequency at about 122 Hz, as can be seen in Figure 5.11 where the comparison between the spectra of heat release fluctuations from experimental measurements and LES self-excited simulation is shown. Only single data points corresponding to the LES peaks are reported, due to the much longer simulation time required to generate a continuous heat release spectrum.

A good agreement was found for the frequencies predicted by LES, whereas the amplitudes result overestimated, probably due to the lower damping in LES with respect to the real combustor. Also the limit cycle calculated from weakly nonlinear stability analysis is shown in Figure 5.11. A better agreement was found for both the frequency and the amplitude, showing the capability of the decoupled FDF-based approach in predicting the instability onset and behaviour.

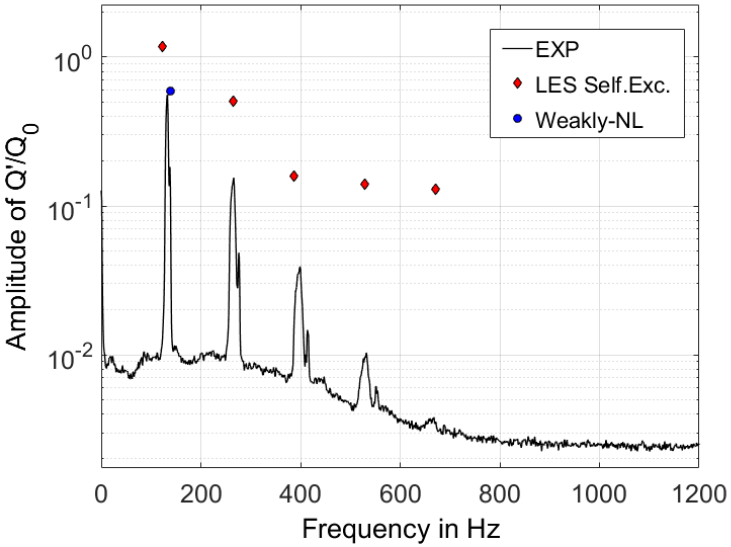

Figure 5.11: Heat release spectra of the instability.

5.5 Concluding remarks

A numerical setup able to reproduce the complex dynamics of a turbulent swirled flame has been validated through the comparison with detailed experimental measurements, showing a good agreement in terms of heat release distribution, flow field and Burner Describing Functions.

Considering the effects of both flame stretch and heat loss into the FGM framework the Flame Describing Functions can be successfully predicted using LES: both the amplitude and the phase of the response, as well as the saturation mechanisms, can be reproduced using the Extended TFC model, thanks to the accurate prediction of the flame topology.

Once obtained the FDF from numerical simulations, it can be used as input for weakly nonlinear thermo-acoustic analysis, in order to accurately predict not only the onset of combustion instabilities but also the behaviour of the system.

A 3D FEM model of the combustor has been used and acoustic analysis have been carried out at different excitation levels, calculating the frequency and the amplitude of the limit cycle of heat release fluctuations.

Finally, results have been compared against experimental measurements and self-excited LES simulations, showing the capability of the simulations to catch the instability observed during the measurements and to accurately predict the behaviour of the system.

Chapter 6

Numerical Prediction of Lean Blow-Off in a Premixed Swirled Combustor

This chapter investigates the blow-off mechanism in a perfectly premixed swirl-stabilized flame experimentally studied at the University of Cambridge. The first part of the chapter describes the experimental test case, together with the measurements that are available and the different investigated flame conditions.

Then, the effect of different modelling choices are assessed. At first, the Finite Rate and Zimont TFC closure for the progress variable source term are compared within the FGM framework. The effects of stretch on the combustion are introduced in Zimont's model firstly with the stretch factor G and a sensitivity to different values of this parameter is carried on. Then, the extended TFC model described in Chapter 3 is validated against experimental data.

Once obtained a numerical setup able to accurately reproduce the flame bahaviour in different operating conditions approaching blow-off, a complete transitory is simulated to gain insight into global extinction phenomena (see [174] and [175] for more details).

6.1 Cambridge Combustor: Test Case Description

The perfectly premixed combustor has been experimentally studied at the University of Cambridge. It was originally used to study ignition of turbulent swirling spray flames (Letty et al. [176], Marchione et al. [177])

and then adapted to study also premixed and non-premixed flames.

In the present work only the premixed methane-air configuration, shown in Figure 6.1, is investigated. The burner consists of an annular duct with a length of 350 mm and an outer diameter of $D_e = 37$ mm and an axial swirler with six vanes oriented at $\theta = 60^\circ$ with respect to the flow direction (Figure 6.2). A bluff-body is located downstream the swirler, ending with a short conical head with a base diameter of $D_b = 25$ mm resulting in a blockage ratio of 50%. The chamber is enclosed by four synthetic optical quartz walls (95 x 150 mm) to enable flame and chemical species visualization. The outlet of the chamber is open to the atmosphere. The burner is fed by a perfectly premixed mixture of air and methane at ambient temperature [26]. The outlet of the chamber is open to the atmosphere. As reported by Cavaliere [26], the swirl number can

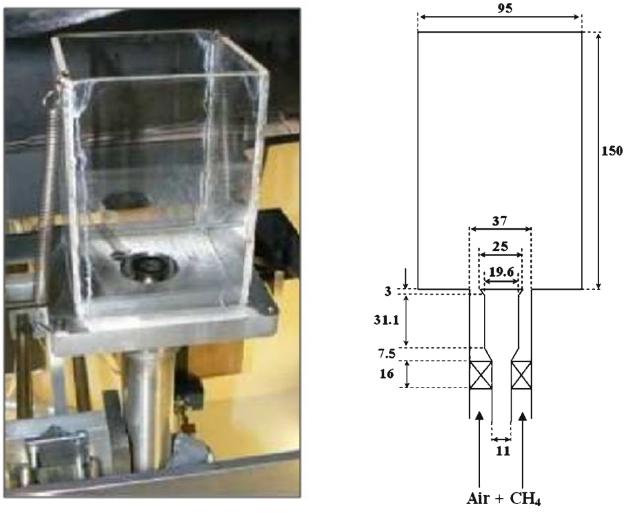

(a) (b)

Figure 6.1: Photograph of Cambridge burner (a) and schematic (b) of the premixed configuration [26, 27].

be estimated with the expression (6.1) derived by Beer and Chigier [178]:

$$S_N = \frac{2}{3} \frac{1 - (D_{hub}/D_{sw})^3}{1 - (D_{hub}/D_{sw})^2} \tan\theta \tag{6.1}$$

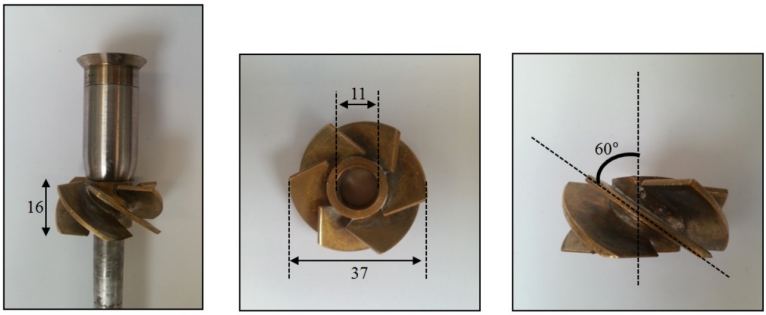

Figure 6.2: Photograph of the bluff body with the swirler (a) and photographs of the swirler from top (b) and side (c) [26].

where D_{hub} and D_{sw} refers respectively to the swirler hub diameter (11 mm) and the swirler tip diameter (37 mm). The swirl number calculated with the previous expression is $S_N = 1.23$.

The burner was developed to understand the mechanisms of local and global extinction in swirl stabilized flames. It was object of several experimental and numerical investigations, mainly focused on the spray flame configuration. The test case was studied during different campaigns using LDA/PDA, OH* chemiluminescence (5 KHz), OH-PLIF (5 KHz) and Mie scattering techniques. Cold flow LDA measurements were carried out by Cavaliere *et al.* [27] with the burner fed by pure air, providing the profiles of mean and RMS velocity components in several axial positions inside the chamber. Different flames were investigated with PDA, OH* chemiluminescence and OH-PLIF with various fuels in spray configuration (Yuan et al. [179]), in dual-fuel (ethanol-methane) mixed-mode (Sidey and Mastorakos [180]), non-premixed (methane) configuration (Cavaliere [26]) and premixed (methane) configuration (Kariuki [28]). These experiments investigated blow-off dynamics, flame stabilization and structure and provided a solid base for numerical modelling. For the purposes of the present study, since the premixed configuration only is considered, the relevant data derive from the experiments of Kariuki [28]. In addiction, cold flow LDA measurements by Cavaliere [26] are used here to validate CFD setup and assess the accuracy of flow field prediction, even if in that condition the inlet velocity magnitude and the Reynolds number are smaller than hot cases. The main results of interest for this work are

presented briefly in the following paragraph.

6.1.1 Flame conditions in premixed configuration

The experimental measurements on premixed flame conducted by Kariuki [28] investigated both stable and approaching blow-off flame. They include:

- Lean blow-off limits;
- OH-PLIF visualizations (5 kHz);
- OH* chemiluminescence visualizations (5 kHz);
- Maps of mean progress variable;
- Flame surface density;
- Probability density function of flame curvature;
- Spectra of OH at different positions.

The flame was analysed through OH-PLIF and OH* chemiluminescence in three operating conditions approaching and during the blow-off. The stable flame conditions are summarised in Table 4.1 as P1, P2 and P3.

Table 6.1: Investigated flame conditions [28].

Name	Case	U_b [m/s]	ϕ	ϕ/ϕ_{BO}
P1	Stable	19.9	0.70	124%
P2	Near BO	19.7	0.61	108%
P3	Just prior BO	19.6	0.57	101%
H1	Just prior BO	30.0	0.60	101%
H2	Transient	30.0	0.57	96%

The conditions are also represented graphically in a bulk velocity-equivalence ratio diagram (Figure 6.3) to evidence their position relative to the lean blow-off limit. The bulk velocity U_b is considered as the nominal axial velocity of the flow entering the combustion chamber, estimated through the total volume flow rate and the area of annulus in that section. The Reynold number ($D_b U_b/\nu$) of the flow in the chamber is around 31500 for the three conditions. The uncertainties relative to flow rate

measurements lead to an error for the bulk velocity and the equivalence ration of $\pm 2\%$ and $\pm 3\%$ respectively [28]. The different conditions were

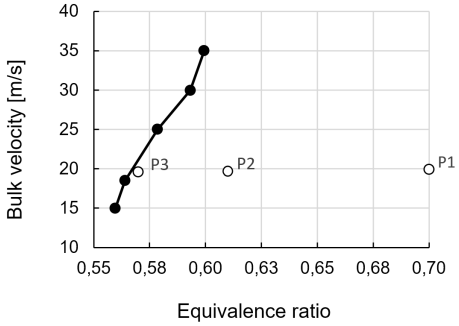

Figure 6.3: Experimental lean blow-off limit (black line) [27] and the three premixed flame conditions investigated.

achieved keeping the air flow rate constant and reducing progressively the methane flow rate. Due to the lower density of methane than air, the reduction of equivalence ratio determines a slight reduction of bulk velocity, following the straight line in Figure 6.3. From the intersection of this line and the blow off limit is determined an experimental blow-off equivalence ratio $\phi_{BO} = 0.566$ and $U_b = 19.59$ m/s.

The P1 condition corresponds to a stable flame that can be regarded as a reference; P2 is a near blow-off condition that should exhibit some quenching features; P3 condition is just prior LBO event, since a further reduction of equivalence ratio leads to the complete extinction. Therefore, in every condition the flame was observed to burn indefinitely.

As can be observed in Figure 6.4, the flame changes its shape significantly. Far from blow-off the light emission is higher near the walls of the chamber. Reducing equivalence ratio to P2 condition moves this emission downstream but is still confined near the walls because of the strong swirl motion. At conditions very close to blow-off the emission is more distributed and expands to the centre of chamber. These behaviours are confirmed by the measurements of OH* chemiluminescence and OH-PLIF. The images of mean OH* chemiluminescence (after forward Abel trasformation to obtain a planar representation of the line-of-sight integrated emission) and mean normalized OH-PLIF for the three conditions are shown in Figure 6.5 and in Figure 6.6.

From the chemiluminescence (Figure 6.5) it can be observed that in

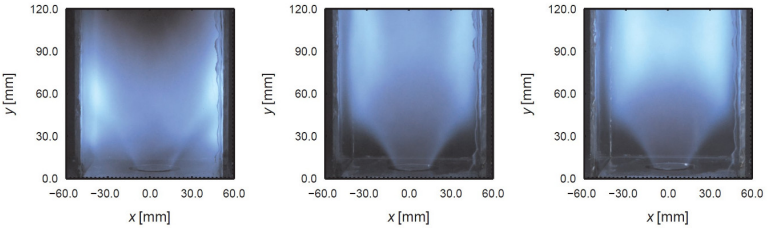

Figure 6.4: Photographs of flames in P1, P2 and P3 premixed conditions (from left to right) [28].

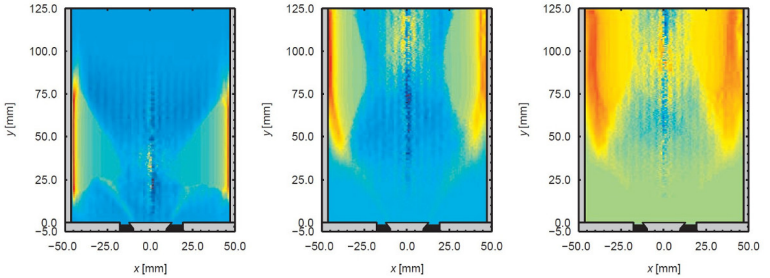

Figure 6.5: Abel trasformed mean OH chemiluminescence of flames in P1, P2 and P3 conditions. The intensity of emission increases from blue to red [28].*

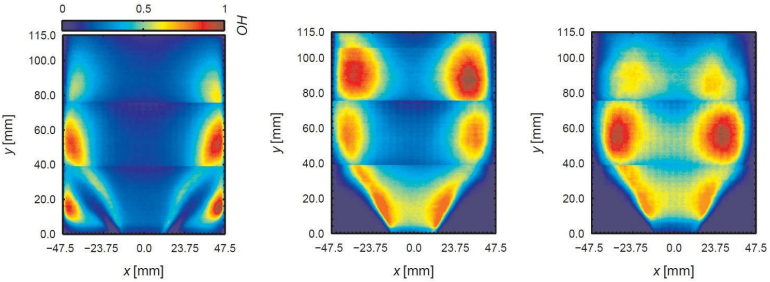

Figure 6.6: Mean normalized OH-PLIF images of flames in P1, P2 and P3 conditions on longitudinal plane. The emission is normalized respect to the maximum value for the single conditions [28].

P1 condition the mean reaction zones are effectively flattened to the walls, with two trails showing that the flame is anchored to bluff body edges. Inside the inner recirculation zone (IRZ) there is no reactivity and it contains almost only burnt gases. At condition near blow-off P2, the flame extends further downstream and the reaction regions are wider, with an emission along the centreline.

Just prior blow-off (P3) the flame brush is much wider and closes toward the centre, while the emission in the anchoring region is very low.

The OH-PLIF images allow to visualise the concentration of hydroxyl radical OH in the plane of laser beam. Differently from other radical like CH, the OH radical can be long-living at elevated temperature and be present in regions where reaction rates are not very high. For this reason the presence of OH does not show exactly the flame front but rather the transition zone from unburned to burnt gas [181]. Observing the Figure 6.6, in P1 condition the double OH peak near the walls is due to the presence of burnt gases both in corner recirculation zones (CRZ) and at about $2D_b$ inside the chamber, where burnt gas from IRZ ignites fresh mixture. At condition P2 the OH radical disappear from the CRZs, revealing that the contact between unburned and burnt gas is maily at IRZ boundary. In fact, a little amount of fresh gas seems to leak near the wall and burn gradually downstream. When the flame is very close to blow-off (P3) the OH peak emission expands and move to the centreline and the bluff body, resulting in a flame that closes across the flow and confines reactivity in the IRZ.

Instead, concerning conditions H1 and H2 in Table 4.1, they were not investigated experimentally except for the blow-off point. In the following, conditions corresponding to P1, P2 and P3 will be investigated at first, in order to validate the numerical setup, while H1 and H2 will be studied in the last part of the chapter for blow-off simulations only.

6.2 Numerical setup

The simulations are carried out using the commercial CFD code ANSYS Fluent v16.1 [139] . The typical procedure to achieve the solution is presented here. At first, RANS simulations for each condition are conducted to simulate the relative isothermal flow field and then the flame. From converged reacting RANS solutions the LES simulations are initialised and the unsteady flow field is calculated until a statistical steady solution is reached. During the final run, time averaged data from LES are extracted sampling approximately 0.07 s of physical time.

6.2.1 Computational domain

The complete computational domain is represented in Figure 6.7 with its main dimensions. Observing the domain three parts can be identified: the burner, the combustion chamber and the far-field and are presented below singularly.

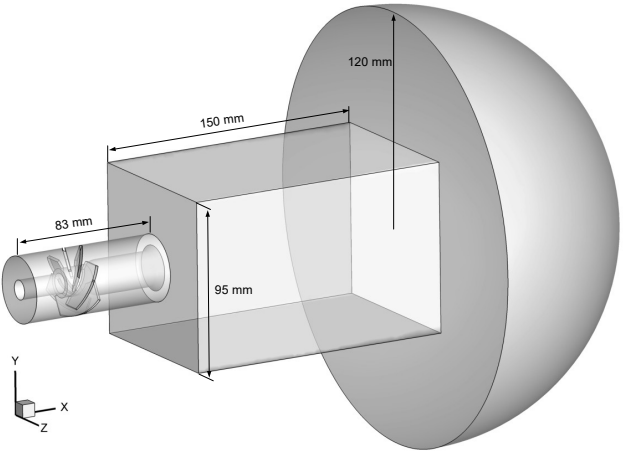

Figure 6.7: Computational domain. Note the hemispherical far-field to model the free atmospheric discharge.

Burner: an annular duct that extends for 83 mm upstream the chamber inlet and includes the axial swirler with six vanes and the bluff body. For the detailed dimensions refer to Figure 6.1b. The length of the burner is chosen arbitrarily to ensure that the inlet is far enough from the swirler and the inlet condition can be imposed without affecting sensibly the flow. After the swirler, the annular passage inner diameter rise to $d = 19.6$ mm and remains constant up to 3 mm before bluff body top where it linearly increases to $D_b = 25$ mm. This sudden reduction in area results in an acceleration of flow and a mitigation of the swirler blades streaks.

Combustion chamber: a simple parallelepiped with a squared cross section of 95x95 mm and 150 mm long. The swirling flow enters the chamber with an axial bulk velocity U_b.

Far-field: an hemisphere with radius 120 mm centred around its outlet. Following Zhang [16], the far-field was added to simulate the open atmospheric discharge and at the same time to reduce acoustic waves reflection on outlet surface. As measured by Cavaliere [26], the inner recirculation zone (IRZ) extends beyond the chamber outlet, thus it is necessary to extend the domain to avoid that the outlet boundary condition influences non-physically the flow field inside the chamber.

Despite the increased computational cost, the burner is included in the domain because it allows a natural generation of turbulence and velocity profiles. The uncertainties associated with LES simulations in complex flows are considered less important than those related to the imposition of velocity profiles and artificial turbulence, needed at chamber inlet if the burner is excluded. As shown in Figure 6.7 the coordinate system is aligned with chamber main dimensions, with x axis being the mainstream direction. For convenience the origin of coordinate system is placed in the centre of bluff body top, so that the xy and xzplanes are longitudinal section planes and $y-$planes are cross section planes. Note that the coordinate system alignment is different from the one used for experimental investigations ([27, 182]).

6.2.2 Boundary conditions

Different conditions are imposed to the boundaries of geometry (Figure 6.8) and are here discussed.

Inlet For all the simulations a constant mass flow rate is specified at the annular inlet. The values were calculated for every condition from the data of Cavaliere et al. [27]. The temperature of the methane-air mixture at inlet is set to 288 K and the density are assumed for methane as $\rho_f = 0.65$ kg/m^3 and for air as $\rho_a = 1.18$ kg/m^3. Since the FGM combustion model is used, mixture composition is determined imposing the experimental values of mixture fraction z. These values are summarised in Table 6.2. In addiction, the far-field base is set as atmospheric pressure inlet of pure air at 288 K. For the RANS simulations a turbulence intensity of 5% and the relative hydraulic diameter is imposed at the inlets. In LES the inlet surfaces are treated as acoustic wave non reflecting surface and no artificial turbulence is introduced. As anticipated before, this was possible because the full burner with the swirler was included in the domain so the structures of flow degenerate spontaneously in turbulence that enters in the combustion chamber.

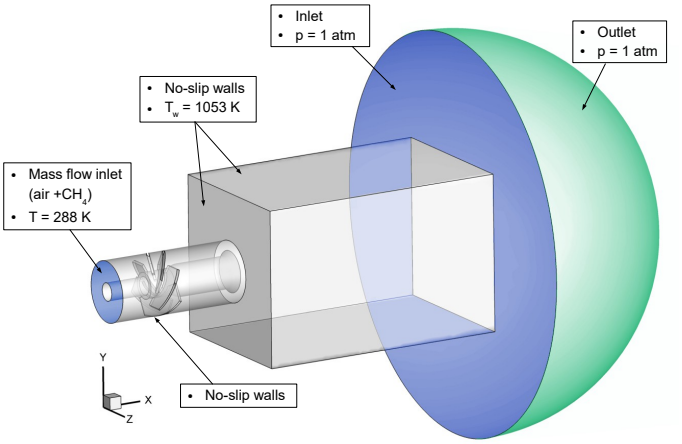

Figure 6.8: Computational domain with the main boundary conditions.

Table 6.2: Inlet conditions derived from [27].

Name	**Case**	U_b [m/s]	ϕ	$\dot{m}$ [g/s]	z
C1	Cold flow	14.3	0	9.83	0
P1	Stable flame	19.9	0.70	13.48	0.0391
P2	Near blow-off flame	19.7	0.61	13.37	0.0343
P3	Just prior blow-off flame	19.6	0.57	13.32	0.0321

Outlet The pressure outlet condition with constant atmospheric pressure (101325 Pa) is imposed to the hemispherical surface of the far-field. In LES the outlet surface is treated as acoustic wave non reflecting surface.

Walls All the other surfaces are representative of solid walls so the non-slip condition is imposed there. The adiabatic condition is set to walls upstream to the flame, like the swirler, the feeding channel and most part of the bluff body up to the conical wedge 3 mm before the top. For the bluff body top and wedge, as well as the chamber walls, it was imposed the temperature of $T_w = 1053$ K, except for the C1 isothermal condition, where they are treated as adiabatic too. This value is estimated because there are no experimental measurements of the wall temperature. A preliminary $k - \varepsilon$ Realizable RANS sensitivity is conducted to assess the impact on flame of the wall thermal treatment.

6.2.3 Mesh

The complete geometry shown in Figure 6.7 is discretized in approximately 7 million polyhedral cells. At first an hybrid mesh of about 28 million tetrahedral cells with three layers of prisms adjacent to solid walls was created with ANSYS Meshing and then it was processed with Fluent v16.1 to generate polyhedral cells. A slice of the mesh is shown in Figure

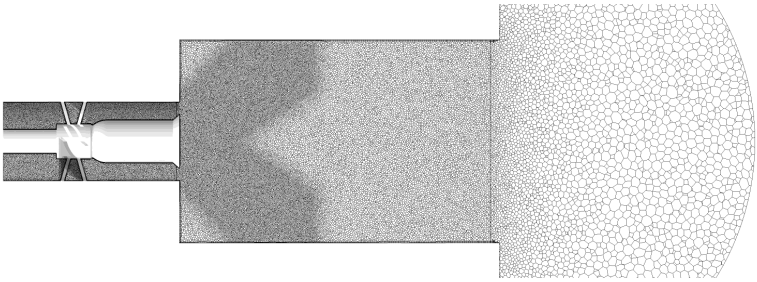

Figure 6.9: Mesh distribution (xy−plane slice).

6.9. The size of polyhedral cells is about 0.5 mm in the burner and 1 mm in the chamber, with a refinement of 0.5 mm that extends inside the chamber for 65 mm in a region with high mixing and shear, as reported by Cavaliere [26]. In the far-field zone the cells gradually raises since

there is no need to resolve detailed flow structures and bigger cells results in a numerical damping of perturbations reflected on outlet surface.

6.2.4 Turbulence model

As far as concern RANS simulations, the turbulence is modelled with the $k-\varepsilon$ two-equation model with the realizability correction [164]. The near wall turbulence is modelled with the scalable wall functions. These functions are equivalent to standard wall functions based on the formulation of Launder and Spalding [183] with a lower limiter y^+ that avoids problems with coarse meshes near wall.

In LES simulations, the sub-grid turbulence is modelled with the Dynamic Smagorinsky-Lilly formulation [137] to allow an adaptive estimation of Smagorinsky constant in time and space.

6.2.5 Combustion model

The combustion was simulated with non adiabatic, compressible, diffusion Flamelet Generated Manifold (FGM) model that in Fluent [139] is based on the control variables of mixture fraction and progress variable. The progress variable source term was closed either with the finite rate model or Zimont Turbulent Flame Speed to evaluate their impact on the flame. In addiction to the standard Zimont TFC model, the extension of TFS model presented in section 3.1.1.3.1 is validated ad used.

6.2.5.1 Chemical database computing

The FGM combustion model requires at first the computation of flamelets to be used to generate the look-up table. The governing equations of laminar flamelets are solved with Fluent built-in CHEMKIN solver with GRI 3.0 reaction mechanism (53 species and 325 reactions) and thermodynamic data. The flamelets were all solved imposing a composition of air-methane with 288 K at the two boundaries in an equally spaced grid of 64×32 points in mixture fraction-progress variable space.

After a preliminary RANS sensitivity to diffusion and various strained premixed counterflow flamelets, it is decided to use the diffusion flamelet to generate the laminar flame database. The flamelets calculated are then pre-integrated in a database or look-up table assuming that the PDFs are $\beta-$distributed. The integration is done specifying 12 points for mixture fraction variance, 21 points for progress variable variance, 41 points for mean enthalpy and including 20 species. For the mixture

thermal conductivity and viscosity, fourth order polynomial functions of temperature are introduced.

6.2.6 Solution methods

The Navier-Stokes equations are solved with the pressure-based solver within Fluent v16.1 with pressure-velocity coupling. The gradients are evaluated with least-squares cell-based method. In RANS simulations the values of the variables in the faces are obtained with the second-order upwind scheme, except turbulence kinetic energy and dissipation for which it was used the first-order scheme. For LES simulations the QUICK scheme is used for energy and FGM equations, while for the momentum the bounded central differencing scheme and second-order upwind for pressure and density.

In LES calculations a time step of $\Delta t = 1 \times 10^{-5}$ s is applied so that the maximum Courant number in the chamber is $Co < 0.6$.

6.3 Results

The numerical setup presented in the previous section is validated in three stable flame operating conditions approaching blow-off, namely P1, P2 and P3 (Table 6.1). The extended TFC model is validated and compared to Finite Rate and Zimont TFC closure for the progress variable source term, within the Flamelet Generated Manifold framework. The effects of stretch on combustion are evaluated also introducing a stretch factor G in Zimont's model and performing a sensitivity to different values of this parameter. When a satisfactory numerical setup over all the three operating conditions is identified, a blow-off transient is simulated.

6.3.1 Non-reacting flow field

To validate the numerical setup and the computational domain, the non-reacting flow field is analysed and compared with LDV measurements by Cavaliere [26]. A *realizable* $k - \varepsilon$ RANS simulation is carried out at the same conditions C1 used for the measurements. The conditions are summarized in Table 6.3.

The value of bulk velocity U_b (i.e. the nominal axial velocity at burner exit) is lower than the one that will be used for flame simulation. However, Cavaliere et al. [27] reported that the main flow-field characteristics do not change qualitatively increasing the inlet flow velocity, so it is meaningful to extend the present isothermal results to the other conditions.

Table 6.3: Isothermal conditions derived from [27].

Name	Case	U_b [m/s]	ϕ	$\dot{m}$ [g/s]
C1	Cold flow	14.3	0	9.83

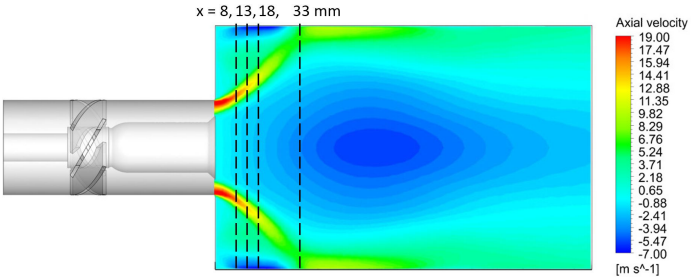

Figure 6.10: Axial velocity field on longitudinal xy plane. The dotted lines represent four experimental LDV sections [26].

In Figure 6.10 the axial velocity flow field on a longitudinal plane is shown. The swirling jet exits the burner forming a conical shape with an angle of roughly 60° and it impinges the wall of the chamber at a distance of about $x/D_b = 1.5$ from the base. The chamber is almost completely occupied by the large inner recirculation zone (IRZ) that extends beyond the chamber. The IRZ progressively shrinks after half the length of the chamber, where the maximum value of reverse velocity is predicted. In the corners two other zones present values of negative axial velocity, forming the corner recirculation zones (CRZ).

The simulated velocity field is compared with experimental data at the different streamwise positions $x = 8, 13, 18, 33$ mm. In Figures 6.11, 6.12 and 6.13 are reported the axial, swirl and radial velocity profiles extracted along the radial direction y (see Figure 6.7) for the selected positions $x = 8, 33$ mm. The radial coordinate is normalized with the radius of bluff body $R_b = 12.5$ and expressed as y/R_b.

As can be seen, the accuracy in prediction of mean velocity field is satisfactory at every streamwise position. The extension of the recirculation zone is correctly reproduced as well as the reverse flow velocity (Figure 6.11). All the components of the swirling jet present values that agree well with the experimental measures, not only at the lower position but also further downstream. The maximum swirl component is slightly

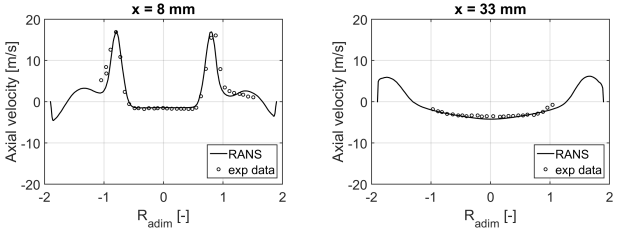

Figure 6.11: Axial velocity profiles along radial y direction for different streamwise locations compared with LDV data [26]. Condition C1.

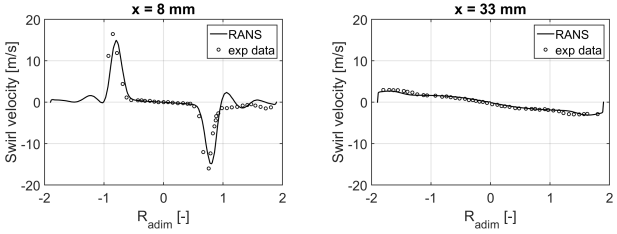

Figure 6.12: Swirl velocity profiles along radial y direction for different streamwise locations compared with LDV data [26]. Condition C1.

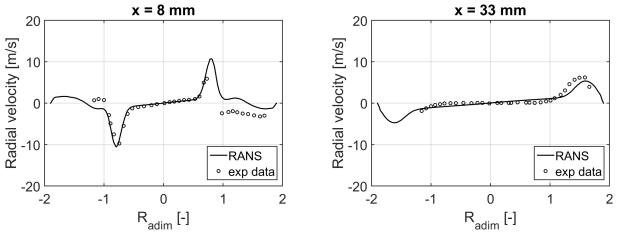

Figure 6.13: Radial velocity profiles along radial y direction for different streamwise locations compared with LDV data [26]. Condition C1.

underestimated at $x = 8$ mm, but the difference is reduced in the next locations. In contrast, the simulated radial component of the velocity results very low in the region near the wall, while the LDV records a little motion toward the axis.

6.3.2 Progress variable source closure sensitivity

As explained in section 3.1.1.2, in the Flamelet Generated Manifold approach the modelling choice that most influences the flame structure is the closure of progress variable source term (see equation (3.4)). The possible closures for $\overline{\dot{\omega}_c}$ available in Fluent [139] are the Finite Rate (FR), the Turbulent Flame Closure (TFC) or an automatic switch to the lower of them.

In the present work the Zimont TFC Zimont et al. [142] and the Extended TFC model are tested and compared for three different flame conditions, reported in Table 6.4.

Table 6.4: Flame conditions simulated.

Name	**Case**	$\boldsymbol{U_b}$ [m/s]	$\boldsymbol{\phi}$
P1	Stable flame	19.9	0.70
P2	Near blow-off flame	19.7	0.61
P3	Just prior blow-off flame	19.6	0.57

In order to be able to predict with reasonable accuracy the inception of blow-off, the desired setup should be able to capture not only the single flame conditions, but also the flame evolution approaching lean blow-off. To do that, the setup should be validated against experimental data over all the flame conditions, and not to be adjusted as the equivalence ratio is decreased.

In general, due to their considerable computational cost, LES simulation is preceded by a RANS study to assess the performance of a model. It is expected that a model should present good accuracy even in RANS framework. The results of simulations with different closures are presented in the following sections.

6.3.2.1 Finite Rate closure

In the Finite Rate closure, the progress variable source term is not modelled, but it is calculated directly from the manifold (see 3.1.1.2.2).

The product formation rates are extracted from the laminar flamelet solutions and pre-integrated with the probability density functions of the progress variable and mixture fraction. During the simulation, the progress variable source term is then accessed like the other tabulated quantities.

The stable flame P1 is simulated with both RANS and LES approach. In Figure 6.14 the average OH mass concentration is reported on the longitudinal xy plane. The value is normalized with the maximum value in the chamber.

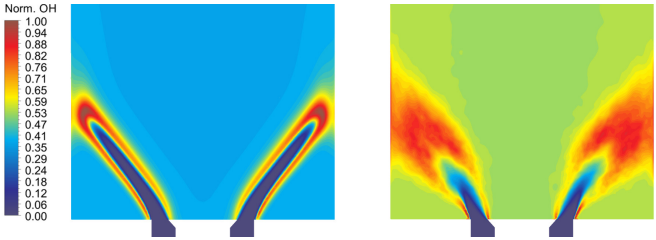

(a) RANS (b) LES

Figure 6.14: Average normalized OH mass fraction on xy plane obtained with RANS (a) and LES (b) simulations using the Finite Rate closure. Stable flame P1 condition.

From the RANS distribution (Figure 6.14a) the flame observed is well defined around the conical swirling jet stream, assuming an "M" shape. The flame extends inside the chamber for about $x/D_b = 1.8$. The shear layers of the jet presents high value of OH and reveals an high reactivity of the flame in these regions. The reaction appears very strong and the fresh mixture burns homogeneously in all directions, without any interruption, starting from bluff-body edge. The peak OH concentration is at the tip of the jet, right before the wall, and no fresh mixture reaches the enclosure of the chamber. All the other parts of the domain are filled with combustion products and there OH concentration is low and uniform. The high temperature of these gases in both the corner and the internal recirculation zones provide a strong stabilization mechanism. The isothermal walls at 1053 K actually reduce the temperature in the CRZ, but this does not seem to reduce flame strength in the external shear layers.

The time-averaged LES results (Figure 6.14b) are quite different, but the high reactivity is clear even there. In fact the fresh mixture is

consumed almost completely before it can reach the walls and the flame is slightly longer up to $x/D_b = 2.2$. However, the fundamental differences are two. At first LES predicts a flame brush that is much wider than RANS does, because of the basically different approach. Within LES simulation most of transport processes are resolved and the average flame distribution is really determined as average of a fluctuating flame front positions. The oscillations of the jet stream spread the fresh mixture over a wider region and high OH concentration are generated. Flame shape in RANS is strictly related to modelled species diffusion (turbulent Schmidt number, here $Sc_t = 0.5$) rather than effective oscillations induced by turbulent mixing. In this sense, the LES prediction is more accurate. The second clear difference is the higher value that LES predicts in RZs with respect to RANS.

Despite the accuracy capabilities of LES simulation, the flame is not well predicted either with RANS or LES. The key features of flame observed by Kariuki [28] with OH-PLIF measurements (Figure 6.6, left image) are not present in the calculated results. In the experimental results the fresh mixture is not burnt as rapidly as in CFD and it impinges the wall of the chamber. Two distinct OH emission peaks show that the regions with high reactivity are divided by the mixture jet. Instead, little OH concentration is found in the shear layers. These discrepancies with PLIF observations can be attributed to an excessive reaction rate used for simulation. In the FGM framework this parameter is represented by the progress variable source term that determines a progress toward equilibrium composition. Since the Finite Rate closure calculates the source term from the solution of laminar flamelets, actually there are not tuning coefficients or other constants to change its value (see section 3.1.1.2.2).

There are only indirect changes which can be made to improve the prediction such as vary the turbulent Schmidt number or the tabulated flamelet, changing their type from diffusion (considered here) and premixed or changing the species in the progress variable definition. With the purpose to analyse further the capabilities of the Finite Rate, all of these attempts are made with RANS simulations. The turbulent Schmidt number is varied within $0.3 - 0.8$ range with diffusion flamelet manifold. However, only minor flame brush width changes are achieved, without improving the prediction. A sensitivity to different premixed flamelets is also carried out with increasing scalar dissipation rates at the stoichiometric mixture fraction from 500 1/s to 6000 1/s using $Sc_t = 0.5$. Although the flame shape changes importantly, the OH mass fraction distribution increasingly deviates from the experimental one. Finally, an alternative

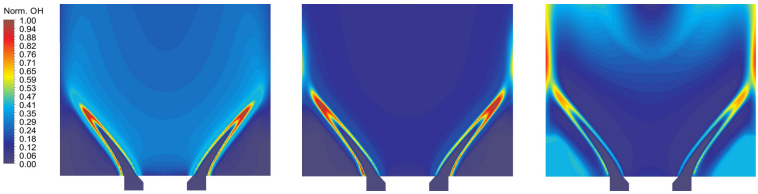

(a) P1 (b) P2 (c) P3

Figure 6.15: Normalized OH mass fraction on xy plane obtained with RANS simulations using Zimont TFC for the P1 (a), P2 (b) and P3 (c) condition.

definition of progress variable based on H_2, H_2O, CO, CO_2 is tested with both premixed and diffusion flamelet. Again, none of these setups allows to increase the accuracy of original results with diffusion flamelet and the default definition of c shown in Figure 6.14a.

Thus, the Finite Rate closure is not considered able to simulate the flame with the precision requested and the Zimont Turbulent Flame Speed closure is employed in the next section.

6.3.2.2 Zimont TFC model

The Zimont Turbulent flame closure derives from dimensional analysis and physical considerations and in the thickened flamelet regime (see 3.1.1.2.3). The model evaluates the progress variable source term using the turbulent flame speed concept and therefore is deeply different from the Finite Rate. Zimont et al. [142] define the turbulent flame speed with a theoretical formulation in function of large scale turbulence parameters and the laminar flame speed.

The Zimont TFC closure is tested with RANS simulations in three flame conditions: P1, P2 and P3. The model constant is assumed as $A = 0.52$ and the stretch factor is not considered, i.e. $G = 1$. The normalized OH distributions that result from the simulation are presented in Figure 6.15. In Figure 6.16 also the corresponding progress variable fields are reported.

From the normalized OH distribution the reaction appears very fast, even more than with the Finite Rate closure. In P1 and P2 conditions the flame brush is thin and becomes wider in front of the swirling jet, consuming all the mixture much before the walls. For the stable flame condition, the corners show no concentration of OH, while in the internal

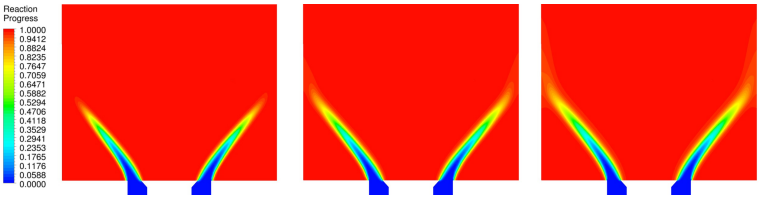

(a) P1 (b) P2 (c) P3

Figure 6.16: Progress variable on xy plane obtained with RANS simulations using Zimont TFC for the P1 (a), P2 (b) and P3 (c) condition.

recirculation there is some radical mass fraction which spreads from the flame brush. In P2 condition this diffusion vanish, and OH is negligible both in the central zone and in the corners. The lower equivalence ratio moves slightly upstream the flame up to $x/D_b = 1.6$, but the flame shape does not change qualitatively. For the conditions just prior blow-off (P3) a noticeable variation of OH concentration can be observed. The reactivity in both internal and external shear layer of the jet slows down, as well as at the tip of fresh mixture stream. The leaner conditions delay the completion of combustion, so that the peak value in OH concentration is registered along the wall at about $x/D_b = 2$. Some radical mass fraction appears also in the corners, probably for a composition slightly different from equilibrium, even if it is not visible in the progress variable contour 6.16c.

The comparison of these results with Kariuki [28] OH-PLIF measurements (Figure 6.6) shows no improvement in the prediction of flame with Zimont TFC with respect to Finite Rate results. What is more, the flame evolution approaching blow-off is not captured. In fact Kariuki observed a radical change between P1 and P2 condition, and the flame that shrinks just prior LBO.

In general, the flame speed seems to be overestimated, with respect to the experimental results. However, the inaccurate prediction of Zimont's model is much deeper. In fact, an overestimation of the progress variable source term could be due to an incorrect value of the constant A and one should expect that reducing its value the accuracy increases. The model is directly related to the laminar flame speed value, calculated at the particular mixture fraction value (see (3.16)). In the simulated flames the fuel and air are perfectly premixed and the mixture fraction is

constant over all the chamber, so it is the laminar flame speed. As the equivalence ratio is lowered from P1 to P3, the mixture fraction and the laminar flame speed decrease. As a result, the progress variable source is reduced, moreover in the same way as would have done decreasing the constant A. In other words, for Zimont's model the reduction of reactivity due to leaner condition is equivalent to a reduction of the model constant. These considerations allow to affirm that the overestimation of reactivity is not systematic over the flame conditions, otherwise the simulated P1 condition should be similar to experimental P2 or P3 condition. However, this is not true, thus excluding the reduction of constant A as possible solution.

Probably the low accuracy of such model is related to the missed modelling of some complex phenomena as the stretch of the flame front, which is able to locally quench the reaction. In the regions with higher strain, where turbulent fluctuations are severe, the reaction rate should be reduced. This lack was acknowledged by Zimont itself and he introduced the stretch factor G to account for this important effect. In the next section the influence of the stretch factor on the accuracy of the standard model of Zimont is assessed.

6.3.2.2.1 Stretch factor influence A possible way to improve the accuracy of flame prediction with Zimont TFC is to introduce the effects of stretch with the stretch factor G (see 3.1.1.2.3). This factor reduces from unity to account for the quenching of flamelets, but necessitates the specification of a critical strain g_{cr} as threshold between totally quenched and unquenched flamelets. It is possible either to specify manually a value for g_{cr} or estimate it through the correlation [139, 143]:

$$g_{cr} = \frac{B S_l^{0\,2}}{\alpha} \tag{6.2}$$

where B is a constant around 0.5. Since one of the purposes of this work is to find a setup that could capture the main flame characteristics approaching blow-off, the correlation (6.2) was used to evaluate g_{cr} instead of a direct specification and different values of the constant B were tested to asses their impact on the flame. This approach allows an automatic reduction of g_{cr}, that is an enhanced sensitivity to stretch of leaner flamelets which have lower values of laminar flame speed S_l^0.

The correlation was implemented in Fluent through a simple user-defined function, assuming a constant value for the thermal diffusivity α and hooking the $S_l^0(z)$ value for the particular condition. The sensitivity was carried out for the stable condition of flame (P1, $\phi = 0.7$) with RANS

simulations. Starting from the usual value of $B = 0.5$, it is progressively reduced to $B = 0.25$ and $B = 0.1$. The resulting values for the critical strain g_{cr} are summarized in Table 3.20.

Table 6.5: Critical strain values corresponding to different costants B in P1 condition.

B	0.5	0.25	0.1
g_{cr} [1/s]	13000	6500	2600

In Figures 6.17 and 6.18 the values of OH mass fraction and progress variable are shown in function of the critical strain g_{cr}. The first distributions 6.17a, 6.18a are obtained with the default model of Zimont (high value for g_{cr}.) As can be seen both in progress variable and OH distributions, there are very little differences between the solutions with totally unquenched flamelets (6.17a, 6.18a) and those with $B = 0.5$ (6.17b, 6.18b), showing that there are negligible zones with estimated stretch over 13000/s. The flame is similarly very short and the reactants burn quickly. If the constant B is further reduced to 0.25, halving the critical strain, the fresh mixture is not consumed completely before reaching the walls of the chamber. The OH mass fraction 6.17c shows two distinct peaks along the wall in both corner recirculation zone (CRZ) and just downstream the impingement point. In addiction, the shear layers of the swirling jet do not presents the high OH concentrations of the previous cases, probably because here the levels of strain are above the threshold g_{cr}.

In the case with the lowest constant $B = 0.1$ the flame is able to stabilize only in the region near the zero-velocity streamline where the strain is lower. While in external shear layer and CRZ there is no reactivity and the mixture is still unburned, there is a considerable OH concentration above the bluff body that connects the thick flame brush on the internal shear layer. However, the most part of the fresh gas burns in the second half of the chamber thanks to the contact with hot products and here the elevated OH concentration shows the transition between them.

From the comparison to the mean OH-PLIF experiments by Kariuki [28] it is clear that the simulation with a constant $B = 0.25$ predicts with reasonable accuracy the stable flame, in particular with the characteristic two separated peaks of OH near the walls (Figure 6.19).

The same constant of $B = 0.25$ was therefore applied to LES. As in RANS framework, with respect to the default setup with $G = 1$, the reduction of g_{cr} has a great influence on the solution. LES predicts a

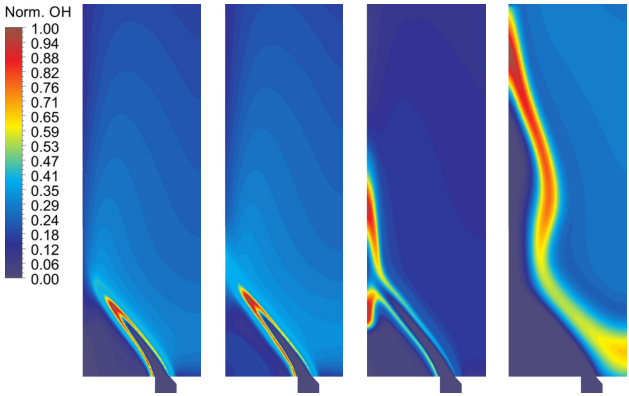

(a) $g_{cr} = 10^8/s$ (b) $B = 0.5$ (c) $B = 0.25$ (d) $B = 0.1$

Figure 6.17: Normalized OH mass fraction on xy plane with different values of g_{cr}.

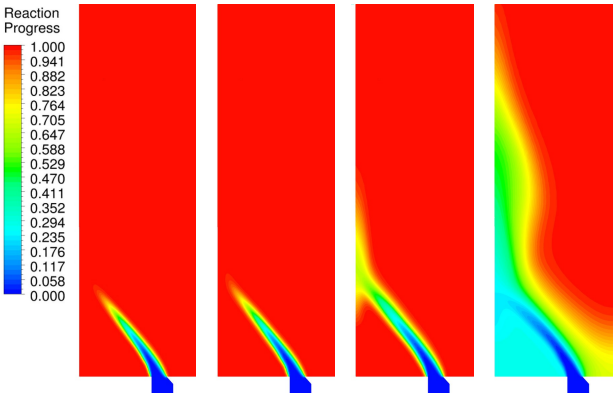

(a) $g_{cr} = 10^8/s$ (b) $B = 0.5$ (c) $B = 0.25$ (d) $B = 0.1$

Figure 6.18: Progress variable on xy plane with different values of g_{cr}.

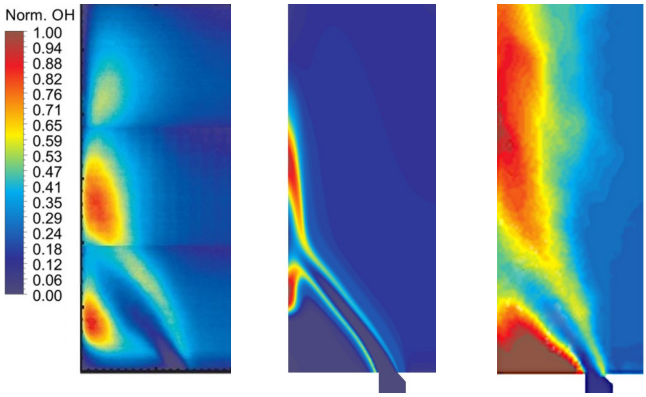

(a) OH-PLIF (b) RANS (c) LES

Figure 6.19: Normalized OH concentration from experiments [28] and simulations with $B = 0.25$. Stable flame P1 condition.

much wider flame brush than RANS simulation, but the key features are maintained with strong OH concentration in CRZ and downstream the point of impingement near the wall. From Figure 6.19 it is clear that in LES the OH distribution has a good agreement with OH-PLIF measurements in the internal shear layer, up to half the length of the chamber, much better than in RANS. On the other hand, the real OH concentration decreases in the second half of the chamber, but this is not captured by LES. Furthermore, LES overpredicts the accumulation of OH in CRZ.

Despite some errors, the stretch factor with a critical strain of $g_{cr} \simeq 6500/\text{s}$ ($B = 0.25$) can improve substantially the solution for the stable flame condition (P1) with respect to the default model, both in RANS and LES. This value is comparable to the commonly used values of $6000 - 8000/\text{s}$ [142, 143].

Applying this FGM setup of Zimont TFC with $B = 0.25$ to P3 condition, i.e. just prior blow-off ($\phi = 0.57$), the flame cannot stabilize and blows off during the numerical transitory in RANS simulation. This is due to the reduced laminar flame speed. In fact, looking at (6.2) the dependence of critical strain g_{cr} to the square value of laminar flame speed leads to a low value of $g_{cr} \simeq 900/\text{s}$ that quenches the flamelet. Actually, P3 condition is very close to the lean blow off limit at the

corresponding bulk velocity ($\phi_{BO} = 0.568$) since the prediction of flame in this conditions is very challenging. For this reason the value of constant B is then increased by steps of 0.05 from 0.25 to find the minimum value that allows the flame stabilization in the RANS simulation. However up to $B = 0.4$ this is not possible: the impossibility to find a value near 0.25 compromises the best setup identified in P1 condition. In fact with values of $B > 0.4$, even if the flame just prior blow-off stabilizes, the prediction of the stable flame would be inaccurate. Therefore the Zimont TFC with the stretch factor formulation is not suitable to simulate the flame in its evolution approaching blow-off.

The stretch effect is overestimated near LBO using the correlation (6.2), probably for its strong dependence on laminar flame speed (see (6.2)). Excluding the correlation, a value for g_{cr} could be imposed directly, but this would require a tuning over all the different conditions in a particular test case. Since the objective of this analysis is to find out one setup valid for all the three flame conditions investigated, the Zimont TFC model with the stretch factor is discarded.

6.3.2.3 Extended TFC application in RANS

As highlighted in the previous results, the stretch factor formulation for Zimont TFC is not able to predict correctly the effects that the deformation of flame front has on the turbulent flame speed. To include the effects of stretch on flame speed in conjunction with the heat loss of flame the model of TFC is extended through the introduction of the correlation for the consumption speed proposed by Tay-Wo-Chong et al. [20]. This value is substituted to the laminar flame speed in standard Zimont TFC closure and the stretch factor G is considered unity by setting $g_{cr} = 10^8$/s. For the details on the correlation and the UDF implementation in Fluent see 3.1.1.3.

The extended TFC model is first tested for all the three flame conditions P1 to P3 with RANS simulations, and the results are presented here. The default constant of the model $A = 0.52$ is not changed.

6.3.2.3.1 Consumption speed distribution The present extension of Zimont relies on a complex dependence of the consumption speed on flow field variables, but the main effects that accounts for are (1) the strain induced by the turbulence and the mean flow and (2) the heat loss with respect to the adiabatic temperature of local products. These two effects enters respectively in the stretch Karlovitz number Ka and in the

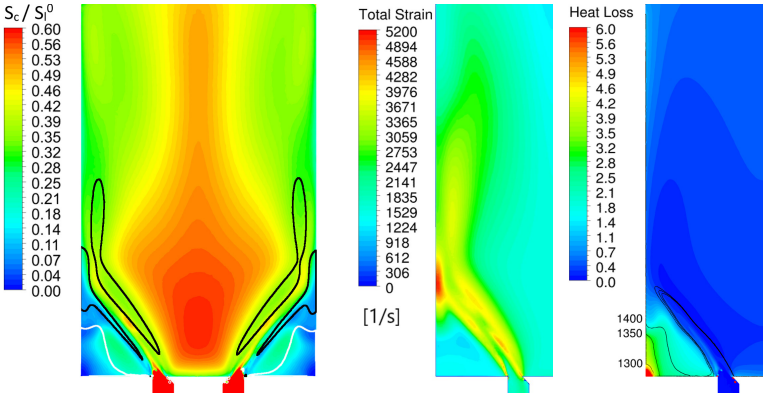

(a) Consumption speed S_c/S_l^0 (b) Total strain $\tilde{a}$ (c) Heat loss φ

Figure 6.20: (a) Field of consumption speed S_c relative to unstretched laminar flame speed S_l^0. Black and white lines represent the isolevels of strain $\tilde{a} = 3400/s$ and heat loss $\varphi = 2$ respectively; (b) Total strain distribution; (c) Heat loss parameter with temperature [K] isolines. Stable flame P1, xy plane.

heat loss parameter φ in:

$$\frac{S_c}{S_l^0} = \exp[-Ka(Ma + \varphi)] \tag{6.3}$$

The ratio (6.3) between the consumption speed and the unstretched laminar flame speed (i.e the default value used without the extension) is plotted in the xy plane for the stable flame condition P1 in Figure 6.20a beside the values of total strain 6.20b and heat loss parameter 6.20c. The consumption speed is significantly lower than the laminar flame speed, with a distribution that follows correctly the levels of strain and heat loss. The strain results high in both the external and internal shear layer with a decreasing tail along the IRZ in the second half of the chamber. The peak value of strain is about 5000/s just before the impingement point of the jet on the wall, between the high velocity of jet and the reverse velocity in the CRZ. Instead the region of the corner at the base and the core of the main recirculation bubble present low values of strain. However, the heat loss 6.20c rises rapidly as the temperature decreases in the corner and amplifies the effect of strain, otherwise negligible there.

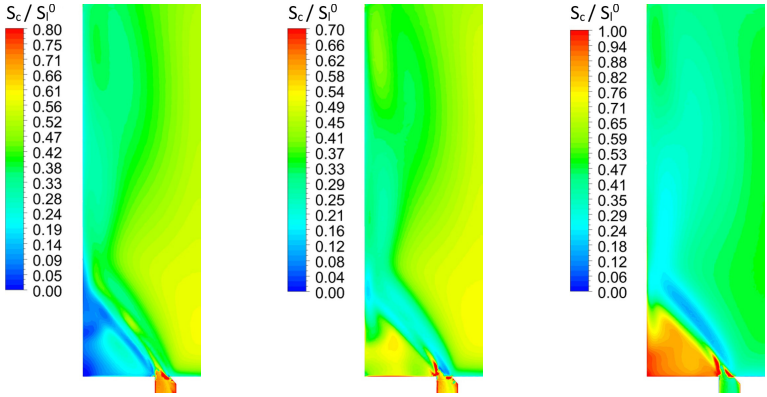

(a) P1 (b) P2 (c) P3

Figure 6.21: Field of consumption speed S_c relative to unstretched laminar flame speed S_l^0 for the three flame conditions P1 (a), P2 (b), P3 (c) on xy plane.

For these considerations, in the internal and external shear layer and in downstream regions the effect on the consumption speed is dominated by the strain while in the corner, where the temperature is lower, is due to the heat loss.

The same observations can be extended to the other flame conditions P2 and P3, as can be seen by the consumption speed fields in Figure 6.21. Since the flow field is not considerably affected by the equivalence ratio variation and the bulk velocity is nearly the same for the three flames, the main features of strain effects are similar. Though the heat loss seems to be much more sensitive to the flame condition, decreasing its effects as the equivalence ratio is reduced. Actually this behaviour is due to the different temperature and composition in the corner zone. If in the stable condition the corner is filled with hot burnt gases ($T \simeq 1300$ K, $c \simeq 0.9$) with high adiabatic temperature ($T_{ad} \simeq 1600$ K), in the condition approaching blow-off (P3) the corner gas has $c \simeq 0.5$ and is colder with a temperature of $T \simeq 1000$ K comparable to the adiabatic one, determining high values of consumption speed therein.

6.3.2.3.2 Flame visualizations In Figure 6.22 the normalized OH mass fraction on xy plane obtained with RANS extension of Zimont's

model are compared to the OH-PLIF results of Kariuki [28] for the three flame conditions P1 to P3. Even if some features of the real flame are not captured by the simulations, the extension shows an improvement of accuracy with respect to the default model.

As far as concern the stable flame P1, the RANS simulation does not show the OH concentration on internal shear layer of the jet captured by PLIF measurements. This differences could be related to the reduced diffusion predicted by the steady simulation. Other key features are actually found in the RANS field, such as the double OH peak just downstream the impingement point of the jet on the wall and the high OH in the corner recirculation. The position of the former is located correctly but indeed its extension is underestimated both in the axis direction and in the flow direction. On the other hand, the OH concentration in the corner is much more extended than in experiments, where the peak is limited to the small bubble of inverse velocity.

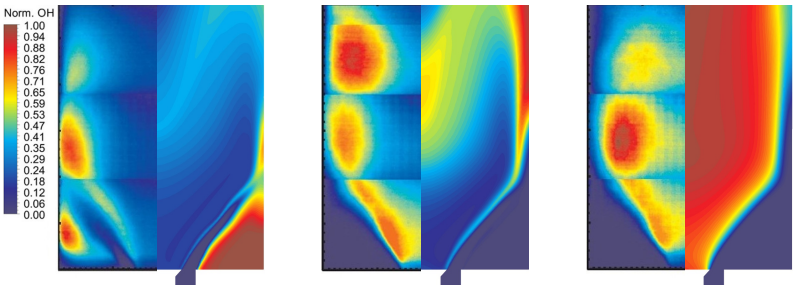

Figure 6.22: Comparison of OH-PLIF (a)(c)(e) [28] and normalized OH mass fraction predicted by RANS simulation with Zimont TFC extension (b) (d) (f) in the conditions P1, P2 and P3 (from left to right).

Approaching blow-off (P2-P3) the experiments indicate that at first the OH concentration disappear completely from the corner zone, showing that the reactivity is only in the internal shear layer around the recirculation, and then just prior LBO the flame closes downstream confining the maximum OH emission to the middle of the chamber. The simulations of these conditions well predict the absence of OH radicals in the corners and the shape of the jet, but for P2 flame the zone above the bluff body and the internal shear layer does not contain almost any OH radical, while in P3 condition here it is moderately overestimated. The simulated flame

P3 does not close across the direction of flow even if a low OH presence along the walls reflects the correct presence of unburned mixture. In the internal recirculation zone the OH seems to be accumulated by CFD because of the low or negative values of axial velocity in this region.

The discrepancies connected with RANS simulation are probably due to the steady state of the solution. Since in FGM framework the OH mass fraction depends primarily on the mean progress variable distribution (the mixture fraction is constant in all the chamber), in regions with low fluctuations, that is low progress variable variance, the OH distribution can present inaccurate value and not actually represent the transition from fresh to burnt gas. This imprecision in RANS prediction can be caused by the modelling assumptions and is expected to vanish during unsteady calculations where the mean OH is really evaluated averaging the distribution on instantaneous progress variable field.

6.3.2.4 Extended TFC application in LES

The extended TFC model is applied to LES with the objective to improve the accuracy of the solutions obtained in extended RANS simulation. Due the uncertainties connected with the specification of the model constant A, a sensitivity analysis is carried out, starting with $A = 1.5$, then reducing to $A = 1$ and $A = 0.925$. In particular, the value of $A = 0.925$ was chosen as equivalent to the RANS constant of 0.52. In fact, in LES formulation differs from RANS for the Smagorinsky constant $C_s^{1/4}$ (equation (3.42)): assuming a reference value of 0.1 (regardless the dynamic Smagorinsky model used for the subgrid turbulence) it can implied in the constant $A = 0.52 = 0.925 \cdot 0.1^{1/4}$. The sensitivity was carried out for the stable flame condition P1 and for the condition just prior blow-off P3 for these three values of A.

6.3.2.4.1 Sensitivity to A constant The results of normalized OH mass fraction obtained averaging 70 ms of simulated time are reported in Figure 6.23 and 6.24 for condition P1 and condition P3 against the experimental results by Kariuki [28].

As can be seen by the OH distribution LES prediction is globally more accurate than RANS simulations, for example concerning the flame brush width. The default value of constant $A = 1.5$ both in condition P1 and P3 results in a shorter flame than that observed experimentally due to an excessive turbulent flame speed, therefore it is judged too high. The fast turbulent flame speed and progress variable source that this value implies lead to a short flame that burns all the mixture before reaching the wall (P1) or in the incorrect presence of OH in the corner and external shear

layer of the jet (P3). With a 50% reduction of A the flame shape changes significantly and similarly to the experiments.

Stable flame condition (P1)

At stable P1 condition with $A = 1$ and $A = 0.925$ the delayed consumption of the fresh gas moves the OH peak concentrations near the wall of the chamber accordingly to measurements (Figure 6.23). Both the lower values of the constant A allow the identification of the two distinct peaks downstream the impingement point and in CRZ, but the mass fraction is underestimated in the internal shear layer with respect to OH-PLIF. The upper OH peak is predicted better by the LES with $A = 1$ since the shape, extension and position are very similar to the experimental measurements. Instead, using a constant A equal to 0.925 the concentration shifts further downstream and flattens to the wall. In the corner the concentration is overestimated in the cases with lower A, with high value extending beyond the CRZ that is the only fluorescent part in PLIF. However, LES with $A = 1$ shows an high OH region slightly smaller and more similar to experiments with respect to the case with $A = 0.925$. Therefore, if an increase in constant A moves upstream the OH concentration peaks, suggesting an optimum value in $1.5 - 1$ range, the higher reactivity would burn the mixture before the jet impinges the wall, leading to an undivided OH peak. On the other hand, reducing the constant value from 1 determines two distinct regions, as shown by experiments. A value of $A = 1$ is thus considered a reasonable trade-off between these two features of OH concentration field in P1 condition.

Just prior blow-off condition (P3)

As far as concern the condition P3 (Figure 6.24), a value of $A = 1.5$ leads to an excessive speed of reaction and features comparable to P1 condition with $A = 0.925$, different from experimental emission. The overestimated OH concentration in the corner is totally eliminated reducing the constant to $A = 1$ and the flame is moved downstream behind the recirculation bubble tail. As for P1 condition, the OH emission in internal shear layer of the swirling jet is under-predicted in the simulation. With respect to the OH-PLIF the LES does not capture the shrinking of OH concentration around the axis near the end of the chamber and the OH mass fraction remains high near the wall. The results with $A = 0.925$ are very similar to ones with $A = 1$ except for the position of OH peak, moved slightly upstream. Nevertheless the experiments show an high OH emission at half the length of the chamber, more concentrated and upstream than in simulations.

The differences between LES with $A = 1$ and $A = 0.925$ result negligible. For that reason the better prediction of P1 condition justifies the choice of $A = 1$ as the more appropriate value. To verify the chosen setup, an additional LES simulation with the extended TFC model has been performed for is then simulated with LES the near blow-off condition P2 with $\phi = 0.61$. The results of normalized mean OH mass fraction are reported in Figure 6.25 for the considered flame conditions P1, P2 and P3. In Figure 6.26 are also reported the instantaneous OH mass concentration distributions for the three cases without normalization.

P2 shows a well predicted OH distribution, in particular concerning the main peak shape and position comparable to the measurements. Nevertheless, the underestimation of OH emission within the internal shear layer persists also in this case and a non-negligible OH mass fraction, not present in PLIF measurement, is predicted in the corner zone, close to the burner exit.

Despite the differences between predicted and measured OH distributions, the overall prediction of all the different flame operating conditions is satisfactory. It is important to stress that the same LES FGM setup with extended TFC model and $A = 1$ is used in every condition without changing. This setup is able to capture the main evolution of flame characteristics approaching blow off, with the progressive reduction of OH in the corner and the thickening of high emission region approaching blow-off. On the other hand, the simulated flame just prior blow-off (P3) does not close across the flow at the end of the chamber as highlighted by experimental measurements. The causes of this behaviour can be various. It is possible that the thermal wall treatment, herein modelled as isothermal walls with an assumed $T_w = 1053$ K, would be important in the regions near to the wall, especially at this condition, and would require further investigations.

6.3.2.4.2 Consumption speed distribution As in RANS application, the consumption speed is the key parameter calculated by the UDF and extends the TFC model, so it is important to analyse its field. In Figure 6.27a is reported an instantaneous distribution of the consumption speed S_c normalized with respect to the unstretched laminar flame speed S_l^0 to highlight the effect of the correction. The black and red lines on Figure 6.27a are isolevels of total strain $\tilde{a} = 3000$/s and heat loss $\varphi = 0.2$ respectively. Strain higher than 3000/s reduces importantly the laminar flame speed especially in the shear layers of the jet and in the second half of the chamber. The total strain calculated by LES is about the double of RANS simulation and in predominantly constituted by the turbulent

strain modelled according to ITNFS model [152]. The heat loss is of the same order of magnitude and is confined near the walls and in the corner where it presents high values which amplify the strain effect over 10 times.

The great difference between RANS and LES for the strain is attributed to the different time scale of the bigger scales of turbulence modelled. In RANS context this coincides with the integral time scale $\tau_t = k/\varepsilon$ while in LES it is the subgrid time scale τ_Δ, that is smaller. With the present formulation the strain is dominated by the turbulent part which is calculated with the inverse of this time scale and corrected with the efficiency function $\Gamma_k\left(L/\delta_l^0,\ u'/S_l^0\right)$. The efficiency is primarily function of the ratio between the biggest scale of turbulence modelled ($L = \Delta$ for LES and $L = L_t$ for RANS) and the laminar flame thickness. Of course in LES this scale of turbulence is smaller than the integral length scale which is considered in RANS simulation and so is the efficiency. However, the efficiency in LES is not low enough to compensate for the smaller τ_Δ, resulting in an overall higher turbulent strain.

The turbulent strain is also the quantity more sensible to the equivalence ratio, among the correction quantities. Due to the complex dependence of the strain on the flow field (see section 3.1.1.3.1) the variation is not straightforward but it can be led back to the reduction of unstretched laminar flame speed S_l^0 with leaner mixtures. For example, moving from P1 to P3 the laminar flame speed halves and the diffusive thickness of flame front doubles making the scale of the biggest modelled eddies appear relatively smaller. The efficiency is then reduced because the spectrum of turbulence that contributes to the strain is narrower ($0.44\delta_l^0 < l < L$), but the turbulence time scale remain roughly the same depending on velocity field. The combined effect is a decrease of the turbulent strain and consequently of the total strain (Figure 6.28). In other words, keeping constant the flow velocity, the extension relaxes as the equivalence ratio is reduces. Instead, the heat loss depends on the temperature field and thus on the flame shape and it is not possible to make similar assessments *a priori*.

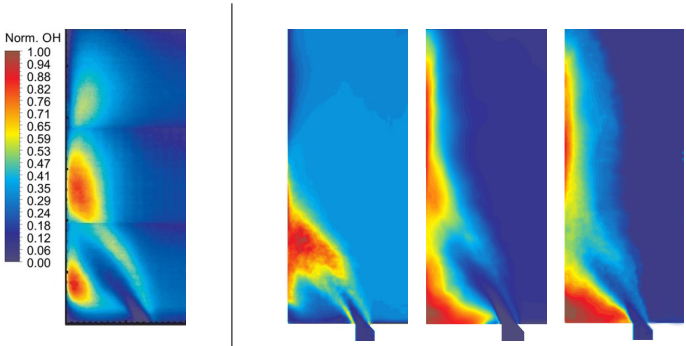

(a) OH-PLIF (b) $A = 1.5$ (c) $A = 1$ (d) $A = 0.925$

Figure 6.23: Comparison of mean OH-PLIF (a) [28] and normalized mean OH mass fraction predicted by LES with Zimont TFC extension with different values for the A constant (b)(c)(d). Stable flame conditions P1, xy plane.

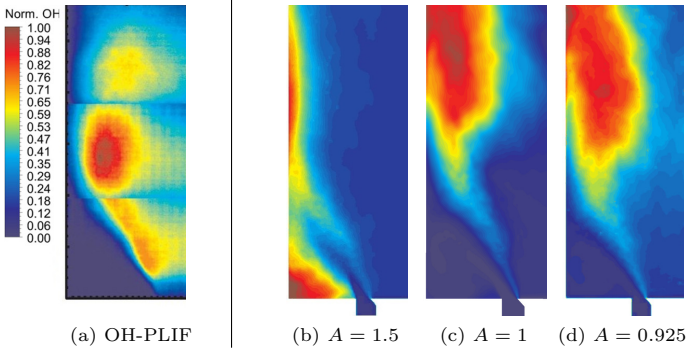

(a) OH-PLIF (b) $A = 1.5$ (c) $A = 1$ (d) $A = 0.925$

Figure 6.24: Comparison of mean OH-PLIF (a) [28] and normalized mean OH mass fraction predicted by LES with Zimont TFC extension with different values for the A constant (b)(c)(d). Just prior lean blow-off conditions P3, xy plane.

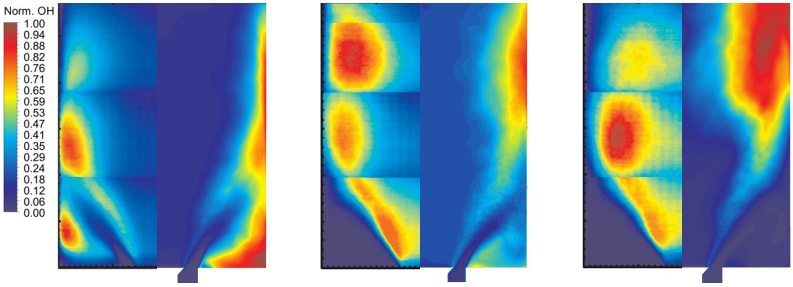

Figure 6.25: Comparison of OH-PLIF (a)(c)(e) [28] and normalized mean OH mass fraction predicted by LES with Zimont TFC extension and $A = 1$ (b)(d)(f) in the conditions P1, P2 and P3 (from left to right).

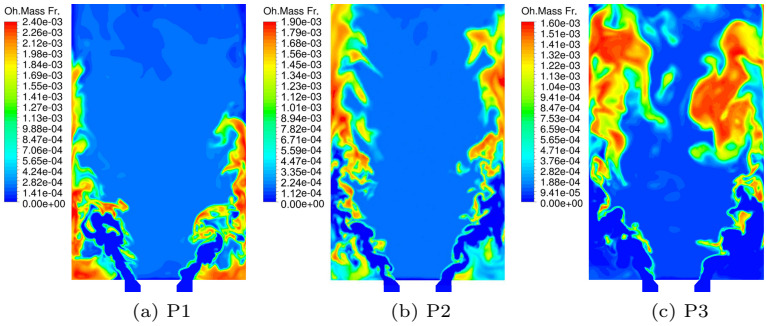

Figure 6.26: Instantaneous OH mass fraction from LES with TFC extension and $A = 1$ for the three flame conditions P1 (a), P2 (b), P3 (c).

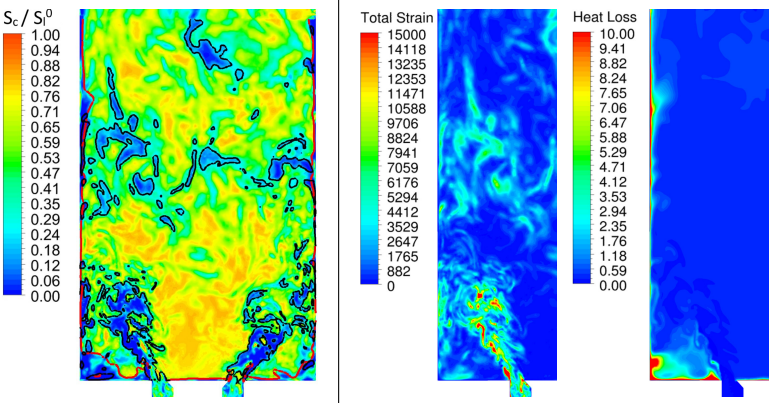

(a) Consumption speed S_c/S_l^0 (b) Total strain $\tilde{a}$ (c) Heat loss φ

Figure 6.27: (a) Instantaneous consumption speed S_c relative to unstretched laminar flame speed S_l^0. Black and white lines represent the isolevels of strain $\tilde{a} = 3000/s$ and heat loss $\varphi = 2$ respectively; (b) Total strain distribution; (c) Heat loss parameter. Stable flame P1, xy plane.

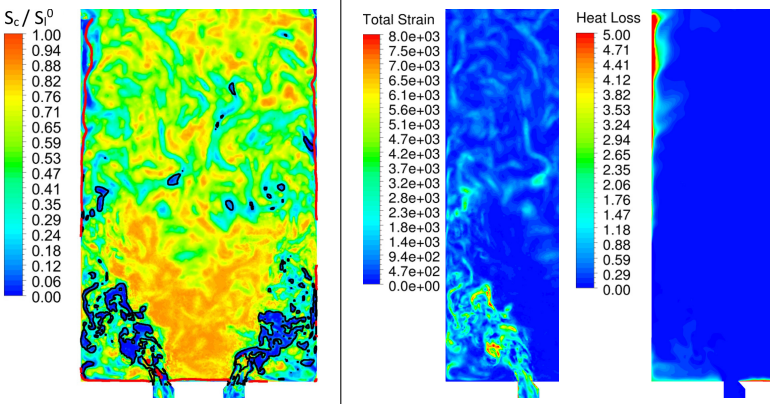

(a) Consumption speed S_c/S_l^0 (b) Total strain $\tilde{a}$ (c) Heat loss φ

Figure 6.28: (a) Instantaneous consumption speed S_c relative to unstretched laminar flame speed S_l^0. Black and white lines represent the isolevels of strain $\tilde{a} = 2000/s$ and heat loss $\varphi = 2$ respectively; (b) Total strain distribution; (c) Heat loss parameter. Just prior LBO flame P3, xy plane.

6.3.3 Blow-off simulation

With the previous simulations a LES-FGM setup able to accurately reproduce the main features of the flame in different operating conditions approaching the blow-off has been identified. For that reason, in the following section the extended TFC with $A = 1$, implemented in Fluent through a user-defined function, has been used. In this section it is investigated the unsteady behaviour of the flame approaching lean blow-off. In the experiments of Kariuki [28] the blow-off of the flame was induced with a gradual reduction of equivalence ratio. After igniting the mixture at conditions far from the blow-off limit, keeping constant the air flow rate, the methane flow rate was gradually reduced. The equivalence ratio resulted in a reduction of roughly $\Delta\phi = -1.7\%\ \phi_{P3}$ every 10 seconds until the blow-off event. The last registered value of bulk velocity was $U_b = 19.6$ m/s.

6.3.3.1 Numerical procedure

To simulate numerically the blow-off transient it is not possible to follow exactly the experimental procedure because of the prohibitive computational costs of such a long simulated time with LES approach. The typical numerical procedure involves an highly accelerated reduction of the equivalence ratio so that the simulated time steps that have to be calculated is not excessive.

Table 6.6: Test points during blow-off transient.

Name	**Case**	$\boldsymbol{U_b}$ [m/s]	$\boldsymbol{\phi}$	$\boldsymbol{\phi/\phi_{BO}}$	$\boldsymbol{\dot{m}}$ [g/s]	$\boldsymbol{z}$
P3	Just prior BO	19.6	0.57	101%	13.32	0.0321
P4	Numerical	19.5	0.54	95.7%	13.29	0.0305
P5	Numerical	19.5	0.51	90.6%	13.25	0.0290

In the present work, a single blow-off event is simulated and analysed. Starting from well developed LES results in P3 condition, the fuel flow rate depletion is obtained with two step reductions, changing the boundary conditions in one go. Reducing over one time-step (1×10^{-5} s) the equivalence ratio of $\Delta\phi = -5\%\ \phi_{P3}$ and the inlet mixture mass flow of about -0.034 g/s each changing, two numerical conditions are identified beyond experimental blow-off limit, namely P4 and P5. The main values in P4 and P5 conditions are summarised in Table 6.6.

These points were calculated as progressive reduction of 5% ϕ_{P3} from the relative previous condition and the bulk velocity was extrapolated by the line of fuel depletion drawn by the other conditions P1, P2 and P3 in $U_b - \phi$ diagram (Figure 6.29). The new conditions P4 and P5 correspond relatively to $\phi/\phi_{BO} = 95.7\%$ and $\phi/\phi_{BO} = 90.6\%$ (experimental $\phi_{BO} = 0.566$), so they correspond to a extinguished conditions in experimental measurements as the flame was already blown off. It is worth to say that a RANS in P4 condition with extended TFC cannot simulate a stable flame and blows off during the solution.

The time interval between the two steps P3-P4 and P4-P5 is not predetermined. Instead, made the first step reduction from P3 to P4 the solution is monitored during the simulation to see if the corresponding equivalence ratio can lead to the global extinction of the flame. However, a such value did not extinguish the flame and after about 0.1 s the second step reduction was applied imposing the P5 conditions. In this condition, the blow-off event was registered after roughly 0.2 s of simulated time, corresponding to very low values of OH concentrations. The exact definition of the blow-off event is presented later in section 6.3.3.2.1. Therefore, the present setup for a bulk velocity of $U_b \simeq 19.6$ m/s predicts the blow-off in an condition between P4 and P5 points. The blow-off range predicted by the simulation is pictured in Figure 6.29. With respect to the experimental value of $\phi_{BO} = 0.566$ [28], there is a good accuracy with an underestimation between $4.3\% - 9.4\%\phi_{BO}$

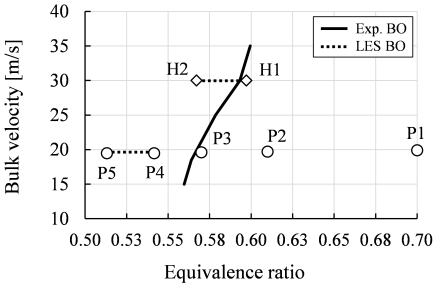

Figure 6.29: Comparison of blow-off range predicted by LES and the experimental blow-off limit [28].

The same approach was followed starting from the stable high flow rate condition H1, reducing the equivalence ratio of 5% ϕ_{H1}. Within the operative condition identified, namely H2, the flame blows off after 120

ms ($\simeq$ 8 FTT).

The accuracy of the extinction limit prediction is remarkable as the blow-off is registered at 95.6% ϕ_{BO} for H conditions and at 90.6% ϕ_{BO} for P conditions. Since the equivalence ratio is reduced impulsively with discrete steps, the numerical observations allow to state that LES blow-off conditions are achieved respectively between H1-H2 and P4-P5. The blow-off ranges predicted are pictured in Figure 6.29. The results confirm that the numerical extinction of a flame during a LES transitory requires leaner mixtures or equivalently higher air flow rates. In fact, in the same test case in non-premixed configuration [135, 184] it was recently observed the LES lean blow-off with a $+20 - 25\%$ air bulk velocity increase respect to experiments, even using different advanced combustion models.

To further investigate the simulated blow-off mechanism, both integral quantities and instantaneous fields are monitored in time, and are presented in the following sections. Similar results are obtained during P and H transitory, so only P results are reported hereinafter for sake of conciseness.

6.3.3.2 Time series of volume-averaged quantities

During the simulation the instantaneous quantities of temperature, product formation rate (PFR, i.e. the specific progress variable source) and the OH mass fraction are volume-averaged in the chamber and monitored to analyse their evolution during the blow-off transient. The results are reported in Figure 6.30. In addiction to the two test points P4 and P5 discussed earlier, to provide a reference value for the quantities, also the P3 condition is initially sampled for 10 ms.

The averaged variables present different behaviours over time. The PFR oscillates much more than temperature, that changes smoothly for its dependence on the entire flow field. Instead, the OH mass fraction presents an unsteady behaviour with high amplitude and slow fluctuations, without a dominant frequency. The quantities that are more sensible to the step reductions of the equivalence ratio are indeed the temperature and the product formation rate. As can be seen from Figure 6.30a and 6.30b, after the changing of boundary conditions at burner inlet, there is a delay of about 10 ms in the response of these variables that corresponds to the time needed to the information to flow through the burner to the chamber. Then, both temperature and product formation rate decreases readily. Changing conditions from P3 to P4 the reduction is rapid for the first 20 ms but, after that, the averaged temperature stabilizes on 1300 K and PFR on about 2.7 1/s; the OH mass fraction does not show a characteristic behaviour and oscillates around 5×10^{-4}, regardless the

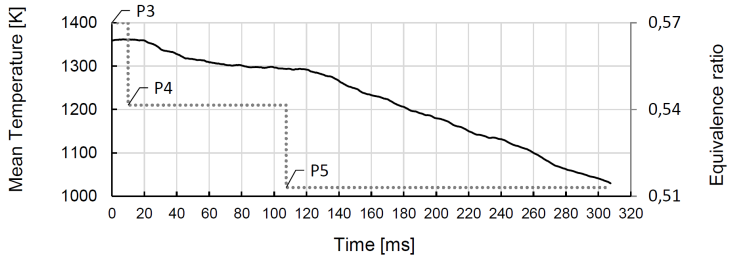

(a)

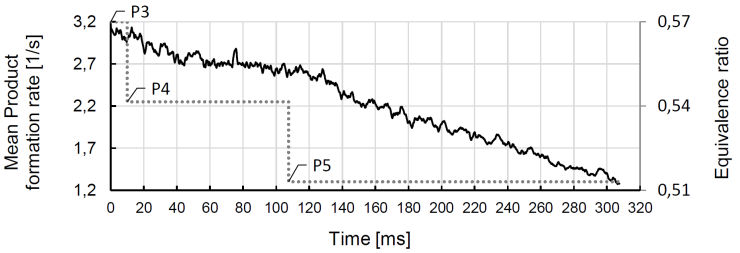

(b)

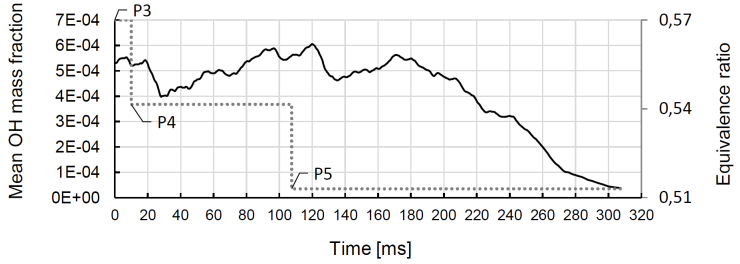

(c)

Figure 6.30: Time series of volume-averaged quantities in combustion chamber during blow-off transient. (a) Temperature, (b) Product formation rate, (c) OH mass fraction. The dotted line represents the equivalence ratio value over time.

reduced ϕ.

From the time history of temperature and PFR it was clear that the global extinction of flame could not be achieved with P3 condition. Therefore, after 0.1 s the conditions were changed to P4. Again, the temperature and the PFR are directly influenced by the leaner condition and exhibit a linear decrease in time over 0.2 s up to the blow-off event. The OH mass fraction continues to fluctuate around a mean value even 90 ms after the reduction of equivalence ratio. However after this delay, at around 200 ms of simulated time the OH mass fraction drops abruptly to zero. This behaviour shows that even if OH mass fraction is extracted from the manifold at a different value of the mixture fraction, it depends much on the flow field. In fact, a lower mixture fraction does not influence instantaneously the OH field, but there is an evolution that will be analysed in the next sections.

6.3.3.2.1 Blow-off duration To define more rigorously the blow-off inception and duration, the approach by Cavaliere et al. [27] in processing the mean OH* chemiluminescence data of the present test case is followed. Here, the volume-averaged OH mass fraction is normalized with its temporal mean value before the final decay to zero (Figure 6.31). This allows to

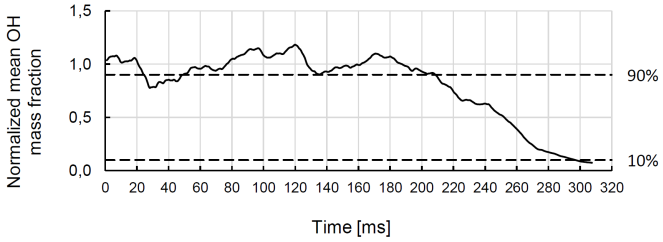

Figure 6.31: Volume-averaged OH mass fraction in combustion chamber during blow-off transient. The value is normalized respect to the mean value before the final decay to zero.

identify the inception of blow-off as the moment in which the normalized OH mass fraction decrease to 90% ($t = 209$ ms) and the blow-off event when it reaches a value of 10% ($t = 297$ ms). The time interval between these events is considered as the extinction time τ_{ext} and lasts 88 ms.

Only as for reference value, the average extinction time measured by Kariuki [28] from many blow off events resulted of 48.6 ms. It should be

emphasized that the OH time history shown in Figure 6.31 represents only a single blow-off event and has not statistical relevance. Obtaining an average extinction time would have a prohibitive computational cost, since it would be necessary to simulate several transients. Moreover, the numerical and experimental procedures to induce the extinction are different and here BO is achieved with leaner conditions. Therefore the direct comparison of the simulated extinction time with experiments is not very meaningful.

6.3.3.3 Flame visualizations

As shown by the volume-averaged value of OH mass fraction in the chamber, this quantity does not respond clearly to the step reduction of the equivalence ratio as the temperature and the product formation rate do. Although, from Figure 6.31 a similar behaviour of OH after each reduction of the equivalence ratio can be observed. In fact after about 10 ms from the inlet condition changing, when the lower mixture fraction value reaches the chamber, the averaged OH presents a rapid drop in its value of about 20%, followed by a relatively slow recovery. While in P4 condition this goes on for almost 100 ms until a new equivalence ratio is imposed, in P5 condition the recovery lasts only about 35 ms and then the final decay of OH occurs.

Here the interest is focused on the last instants of flame, so only its behaviour after the switch to conditions P5 is investigated in detail. In particular, starting from the arrival of the leaner mixture in the chamber ($t = 120$ ms) up to the blow-off event ($t = 297$ ms), three stages of the flame can be identified:

1. Flame positioning in recirculation zone
2. Flame structure fragmentation
3. Destruction of anchoring region

The time location of the stages is represented over average OH concentration time history in Figure 6.32. This subdivision can be found also in instantaneous OH distributions on xy plane and is analysed singularly for each stage. It is worth to note that in all the three stages the equivalence ratio is the same ($\phi = 0.51$).

Stage I (120 − 209 ms)

During the first stage the flame changes significantly its shape and structure due to the lower equivalence ratio imposed. However, the

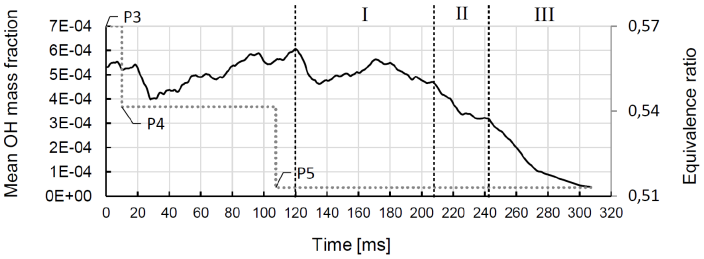

Figure 6.32: The three stages identified during the transient shown over volume-averaged OH mass fraction time history.

variation is not straightforward. The average OH mass fraction in the chamber shows a rapid drop during few milliseconds and a slower recovery. In Figure 6.33 three different acquisitions of instantaneous OH mass fraction, around the drop in average OH value, are presented at $t = 120$, $t = 135$ and $t = 170$ ms. At $t = 120$ ms the average OH has a maximum and corresponds to the last time step with P4 conditions. Instantaneous OH distribution shows a wide flame brush and high values in the IRZ up to $2D_b$ above the bluff body. As soon as the leaner flow gets through the burner to the chamber, the average OH falls rapidly to a minimum value at $t = 135$ ms. This is due to a global reduction in instantaneous OH concentration. The flame brush appears thinner and the flame burns less vigorously.

However, the average OH concentration slowly recovers despite the maximum instantaneous value of OH almost does not change. This is due to the lower equivalence ratio that reduces the speed of flame, leading to local extinctions in the shear layers where the strain is higher. The combustion stabilizes progressively in the IRZ with the confinement of the OH mass fraction peak in the region with reverse flow. Probably this is due to the progressive leakage of fresh reactants across the flame front into the RZ, that dilutes the fully burnt gas. In such a region, the flow presents low velocity and allows the weakened reaction to occur. This high OH concentration zone moves slowly toward the bluff body in the central zone with reverse flow. Roughly at $t = 180$ ms it reaches the bluff body head. The final decay of average OH that leads to blow-off follows rapidly. The same behaviour of instantaneous OH is presented around the drop at $t = 30$ ms after the switch from P3 to P4 condition (not reported here), with OH that at first flattens to the sides and than locates in the central zone.

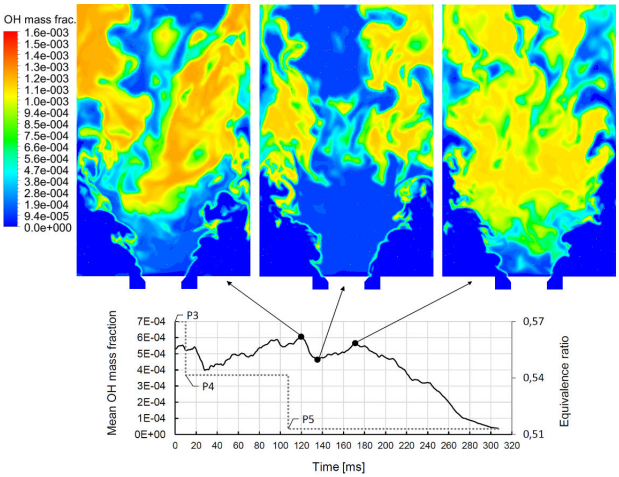

Figure 6.33: OH mass fraction on xy plane around a temporary drop in average value. Left image is taken at $t = 120$ ms, middle at $t = 135$ ms, right at $t = 170$ ms.

This first stage can be regarded as the attempt of the flame adapting the leaner condition. However, if this was possible with P4 conditions, here the flame resists only until a certain point. The flame changes shape and stabilization region, confining the high OH concentration in the internal recirculation. Instead, in this stage, the averaged OH concentration in chamber does not decrease significantly and is confined between $90 - 110\%$ of its mean value.

Stage II (209 − 242 ms)

The second stage starts when the normalized average OH decrease under 90% at $t = 209$ ms. As shown in the section 6.3.3.2.1, this is the instant that is formally associated with the beginning of blow-off event. During this phase, the flame is subjected to strong fluctuations and its structure is severely affected by the turbulence. The behaviour of the flame can be analysed recording the instantaneous OH mass fraction distribution on a longitudinal plane, reported in Figure 6.34 from $t = 210$ ms. It is not easy to understand all the variation on the xy plane reported, because the strong swirl causes out-of-plane movements that cannot be seen here. However, the contours can show how the reduced reactivity of

the flame and the turbulence interact.

At the beginning of the stage, the high concentration zone in the middle starts to fluctuate and appears more and more fragmented. The fragmentation starts on the side at half the length of the chamber and then extends both upstream and downstream. This phenomenon is triggered by the turbulent structures that strain the flame in this region, leading to local extinctions. In the simulation, the effect of turbulent strain on the reaction is included thanks to the Extended TFC model and results in a rapid reduction of local flame speed. Many pockets with low reactivity forms at boundaries of IRZ and cause the corrugation and fragmentation of the flame sheet. A such behaviour is confirmed by OH-PLIF visualizations by Kariuki [28], reported in Figure 6.35. The instability makes the OH concentration near the walls decrease and the most part of OH mass is confined around the axis in IRZ. The reduction of the high OH distribution to a central zone provides an explanation to the abrupt fall in average OH between $t = 210 - 225$ ms (Figure 6.32).

This progressive process of fragmentation alters significantly the flame structure and induces severe fluctuations of OH distribution (Figure 6.34, $t = 225 - 240$ ms). It is important to note that the instabilities that affect the flame start from the central zone near the walls and moves to the centre while extending their influence. However, if the flame in central downstream region is reached rapidly, the high OH zone above the bluff body head resists in this stage. This provides a relative strong stabilization zone for the flame.

Stage III (242 − 297 ms)

The last stage of the flame represents the final instants before complete extinction. In the initial part of the stage, the anchoring region behind the bluff body is destroyed due to the diluted and cooled mixture which descends from the IRZ core. Actually, this happens quite rapidly over about 15 ms ($t = 242-257$ ms), but some OH mass fraction persists longer. The flame progressively disintegrates forming elongated structures and rapidly blows off. The long and narrow shape assumed by the simulated flame in these last instants is not dissimilar from the observations of Kariuki [28] in Figure 6.35. These behaviour are globally confirmed by the rapid decay of average OH (Figure 6.30c) between $t = 242 - 270$ ms. At $t = 270$ ms the the average normalized OH is 20% of its original value (Figure 6.31) and its reduction rate abruptly slows down. Only isolated low-reacting zones are present and are washed out during the remaining instants.

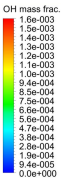

(a) $t = 210$ ms (b) $t = 215$ ms (c) $t = 220$ ms (d) $t = 225$ ms

(e) $t = 230$ ms (f) $t = 235$ ms (g) $t = 240$ ms (h) $t = 245$ ms

(i) $t = 250$ ms (j) $t = 255$ ms (k) $t = 260$ ms (l) $t = 265$ ms

(m) $t = 270$ ms (n) $t = 275$ ms (o) $t = 280$ ms (p) $t = 285$ ms

Figure 6.34: Snapshots on xy plane of OH mass fraction during blow-off from $t = 210$ ms to $t = 285$ ms. P5 condition.

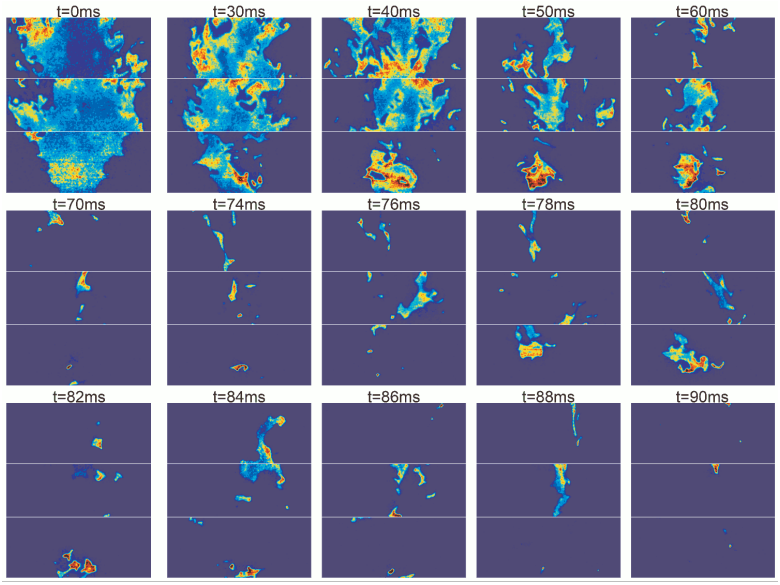

Figure 6.35: OH-PLIF snapshots [28] during blow-off. The time is relative to experiments and is not linked to simulations. OH emission is normalized with the respective maximum for each laser window (anchoring, middle and downstream regions).

6.3.3.4 Progress variable isosurface analysis

In order to investigate the fragmentation of the flame front approaching and during the blow-off, the solution is postprocessed to describe the isosurface of progress variable $c = 0.5$ at different solution times. Computing the extension of this surface inside the chamber at $t = 10,\ 107.5,\ 227.5,\ 267.5,\ 307.5$ ms a noticeable variation is observed (Figure 6.36).

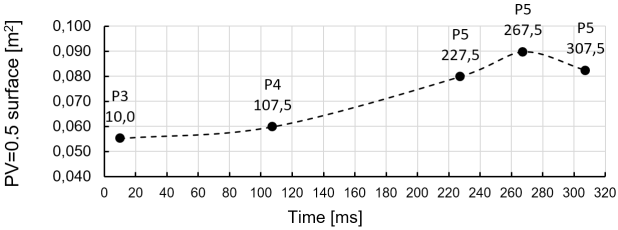

Figure 6.36: Extension of progress variable isosurface of $c = 0.5$ inside the chamber recorded at different moments. The dotted line is a supposed time trend.

Between P3 and P4 the area slightly increases with an average of 0.48 cm^2/ms. The increment rises for the P5 condition to 1.67 cm^2/ms before $t = 227.5$ ms and then to 2.47 cm^2/ms, leading to the maximum registered extension of the surface (897 cm^2). After this point, the area decreases rapidly until the blow-off. Of course the five points analysed cannot reconstruct the real time history and a trend can only be supposed (dotted line in Figure 6.36). Nevertheless, the behaviour shown by the surface area of $c = 0.5$ is very interesting. In fact, the time at which the maximum extension is achieved roughly corresponds to the total destruction of OH concentration behind the bluff-body, which represents the last stage of blow-off (see Figure 6.34 at $t = 265$ ms). Before that moment, the OH distribution shows that the flame is fragmented in small structures. This is probably the cause of the continuous increase of the flame sheet surface. However, at $t = 265$ ms the anchoring region is compromised and the flame abruptly extinguishes, determining the reduction of $c = 0.5$ surface.

In Figure 6.37 the instantaneous progress variable distributions at different cross-sections inside the chamber are reported for the same instants. The $c = 0.5$ level is highlighted with a black line. Axial positions of the section are $x = 15, 25, 40, 50$ mm. Three-dimensional visualizations

of $c = 0.5$ isosurface are also shown in Figure 6.38.

The first two rows in Figure 6.37 and Figures 6.38a(b) correspond to P3 and P4 conditions respectively. The progress variable contours at each axial position and the isosurfaces are very similar. Both inside the IRZ and outside the swirling jet the progress variable is over 0.5, but the real stabilization occurs in the central zone full of burnt gas. The $c = 0.5$ isoline is well defined and located in the shear layer around the swirling jet of mixture, as evident in $x = 15, 25$ mm. Downstream, at $x = 40, 50$ mm sections, the progress variable shows that the majority of the chamber is filled by the burnt gas in the recirculation bubble. This is confirmed by the three-dimensional visualizations (Figure 6.38a(b)) where the $c = 0.5$ isosurface is relatively short and does not present isolated zones downstream.

At $t = 227$ ms (P5 conditions) some differences appear and they are all linked to the stage II identified in the previous section. The strong flame instability, shown by OH in Figure 6.34, that induces the final extinction, corrugates and leads to the fragmentation of the flame sheet. The turbulent strain quenches locally the flame sheet determining low-reactive isolated zones. This phenomenon can be observed at each axial position, but especially at $x = 15$ mm and $x = 50$ mm sections (Figure 6.37). Many isolated zones with $c < 0.5$ detach from the shear layer and move toward the wall. At $x = 25$ mm section many unburned pockets stick to the walls creating holes in the flame sheet. Looking at the $c = 0.5$ isosurface in Figure 6.38c, the fragmentation of the flame front is evident, with zones both upstream and downstream, near the base of the chamber. The corrugation and fragmentation of the flame is the main cause for the $c = 0.5$ surface area increase. The value of progress variable in the IRZ drops from unity, revealing that the gas in the internal recirculation departs from chemical equilibrium. However, at the lower section $x = 15$ mm the progress variable along the axis is higher than in the other sections downstream, providing a stabilization region for the flame.

The fragmentation of the flame is exalted during the next instants. Between $t = 227 - 267$ ms the flame structure is globally altered until the anchoring region is destroyed (stage III). In fact, as clear in Figure 6.34, during this time interval the flame presents strong fluctuations until the OH accumulation above the bluff body is washed out. These instabilities quench locally the reaction and the flame sheet is fragmented, leading to the maximum extension of c isosurface at $t = 267$ ms (Figures 6.36 and 6.38d). The progress variable contours in $x = 15$ mm section (Figure 6.37) present the maximum number of isolated zones, enclosed by black isoline. At $x = 25$ mm the flame sheet is very finely fragmented and the

$t = 10$ ms

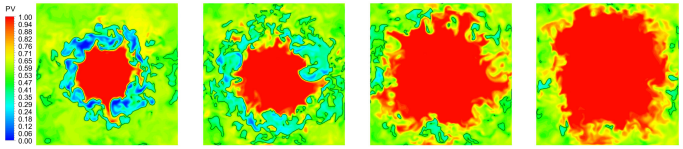

(a) $x = 15$ mm (b) $x = 25$ mm (c) $x = 40$ mm (d) $x = 50$ mm

$t = 107$ ms

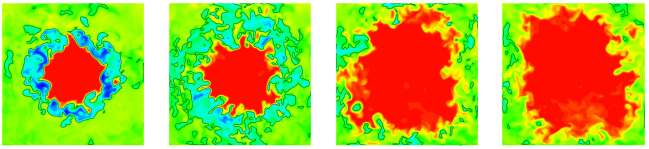

(e) $x = 15$ mm (f) $x = 25$ mm (g) $x = 40$ mm (h) $x = 50$ mm

$t = 227$ ms

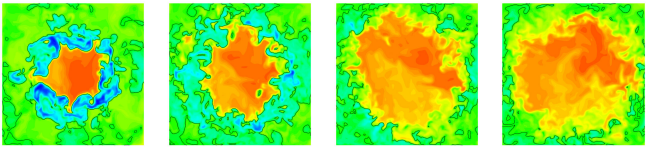

(i) $x = 15$ mm (j) $x = 25$ mm (k) $x = 40$ mm (l) $x = 50$ mm

$t = 267$ ms

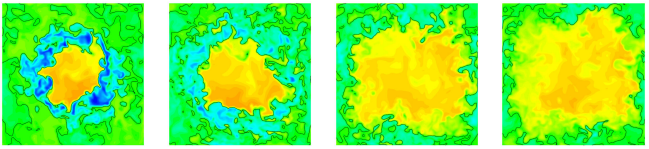

(m) $x = 15$ mm (n) $x = 25$ mm (o) $x = 40$ mm (p) $x = 50$ mm

$t = 307$ ms

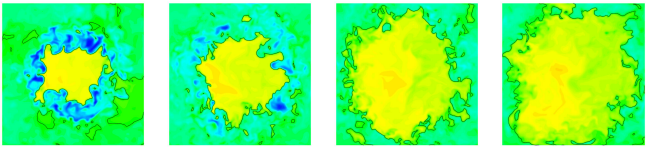

(q) $x = 15$ mm (r) $x = 25$ mm (s) $x = 40$ mm (t) $x = 50$ mm

Figure 6.37: Top view of progress variable at different positions.

majority of fluid adjacent to walls is predominantly unburned. The value of progress variable in the axis shows that the IRZ does not contribute any more to stabilization. After this moment the flames blows off rapidly.

At instant $t = 307$ ms, when the flame is just blown off, the progress variable isosurface and distributions radically change (Figures 6.38e and 6.37). According to the reduced global extension of $c = 0.5$ isosurface (Figure 6.36), the fragmentation is much lower than the previous instant at every section. The chamber has low values of progress variable, especially near the walls. Now the 0.5 isoline is located in the internal shear layer only. This feature is evident also analysing the three-dimensional isosurface of c in Figure 6.38e. The surface seems to "explode" near the base of the chamber. Differently from the others instants, in fact, the outer face of surface situated in the external shear layer is not present here (see Figure 6.37). This deep change reflects the loss of any flame structure.

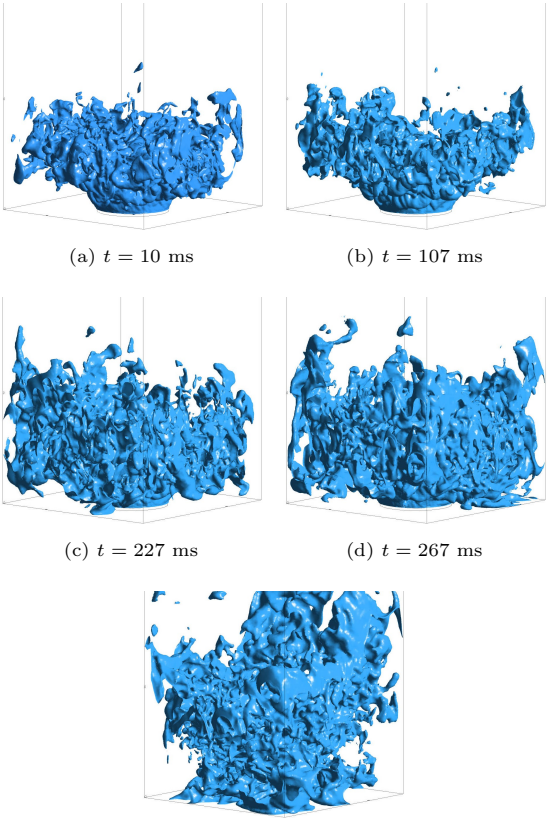

(a) $t = 10$ ms (b) $t = 107$ ms

(c) $t = 227$ ms (d) $t = 267$ ms

(e) $t = 307$ ms

Figure 6.38: Isosurface of $c = 0.5$ in the combustion chamber at different instants approaching blow-off.

6.4 Concluding remarks

The Extended TFC model that has been validated over the three flame conditions is used to predict the blow-off inception. A single blow-off transient is simulated for a bulk velocity of $U_b = 19.6$ m/s. Despite the accelerated numerical procedure with two step reductions of ϕ, the model underestimates the blow-off equivalence ratio between 4.3% - 9.4% ϕ_{BO}, which shows its overall good accuracy.

The flame behaviour during blow-off is analysed with global and instantaneous OH mass concentration and with the visualization of $c = 0.5$ isosurface. The blow-off mechanism observed is the following:

1) Flame positioning in recirculation zone: the flame responds rapidly to the leaner mixture and changes progressively its shape. The reduced flame speed moves the reactivity within the internal recirculation zone where the velocity is lower. This is possible since the reduced reactivity in shear layers allows the entrainment of fresh mixture in the RZ that mixes the fully burnt gas. Instantaneous OH mass concentration in this zone slowly increases and gradually moves toward the bluff body. The averaged OH mass fraction over the chamber does not change much and oscillates between $90-110\%$ of its mean value.

2) Flame structure fragmentation: the high turbulent fluctuations affect importantly the structure of the flame, weakened by the low equivalence ratio. Starting from the sides of RZ at half the length of the chamber, high strain regions further reduce the flame speed, creating numerous pockets with low reactivity. This effect is simulated through the Extended TFC model. The flame stabilized in RZ is increasingly corrugated and fragmented and loses its shape. These instabilities then extends rapidly to all the other zones, except the wake immediately behind the bluff body. That zone remains the main stabilization region of the flame. The averaged OH mass fraction drops rapidly from 90% to 60% of its mean value.

3) Destruction of anchoring region: the indirect effect of turbulent fluctuations destroys the last high OH concentration in the bluff-body wake. Low reacting and cooled gases move gradually from the IRZ core to the bluff body head. As soon as they reach it, the anchoring region is compromised and does not provide any more a stabilization for the reaction. The flame forms long and narrow regions with higher OH and rapidly blows-off. At the same time,

the average OH concentration in chamber reduces quickly from 60% to 20% of its mean value, and then slowly to 10%.

The blow-off mechanism that is observed here from the CFD simulation is very similar to the one reported in literature for non-swirling bluff body stabilized premixed flames [28, 66, 67] approaching blow-off. The fact that the flame investigated in this work presents a strong swirl does not prevent the comparison of these two blow-off processes. Zhang et al. [68] and later Kariuki [28] agreed that the key characteristics of the blow-off mechanism for bluff body stabilized flames shows many similarities to the blow-off in swirl stabilized flame. This observation is confirmed also in the present work.

Most of the key processes that Chaudhuri et al. [66] and [67] identified can be traced also in the present numerical investigation. In particular the similarities with experimental observations approaching blow-off are the following:

- The flame shape changes and the interaction with the shear layer increases;
- Flame front along the shear layer highly strained, resulting in local flame extinctions;
- The downstream parts of the flame are fragmented;
- Thanks to the local flame extinctions, fresh mixture entrains through the shear layers and reacts within the recirculation zone, where the residence time is higher;
- This flame kernel within IRZ can reignite the shear layers and eventually re-ignite the shear layers several times;
- Final blow-off occurs when the flame kernel fails to reignite the shear layers, and the flame at the bluff body edges had been destroyed.

It is worth to emphasize the importance of the Extended TFC model in the last instants of flame. After the flame shape change (during the stage I), the observed phenomenon that really triggers the blow-off is the fragmentation and quenching of the flame sheet. In the simulation, the effect of the turbulent strain affects strongly the consumption speed as calculated by the adopted correction. The regions with high strain reduces exponentially the local flame speed and so the reaction progress is slowed down. At first this changes the global shape of the flame inducing wide fluctuations and fragmentation of the flame front. The

flame stabilizes in the IRZ for the entrainment of fresh mixture, the fluctuations progressively reduce reactivity in the central region and later affect the anchoring region behind the bluff body, leading to blow-off. In contrast, in simulation with the standard TFC model, the turbulent flame speed is increased by the turbulent velocity fluctuations, if the stretch factor is not considered. However the stretch factor results a very simple model that does not perform well over different conditions approaching blow-off. The Extended TFC model include these physical effects of flame front stretching and thus allows a better prediction of the interaction between turbulence and chemistry in the FGM framework.

Moreover, this study shows again the importance of the turbulent fluctuations during the last stages of the blow-off process. With the present investigation it is acknowledged that standard closures in FGM model presents a limited capability when turbulence-chemistry coupling affects significantly the flame behaviour. This complex coupling implies an extraordinary modelling effort and requires ad-hoc detailed models to broaden the capabilities of standard closures in FGM model. In this context, the Extended TFC model represents a valid tool able to increase the accuracy of flame prediction near blow-off, with a negligible increment of computational cost.

Conclusions

Modern gas turbines usually adopt very lean premixed flames to meet the current strict law restrictions on nitric oxides emissions. In such devices, strong combustion instabilities and blow-off susceptibility often prevent from achieving a stable flame in leaner conditions. From a design perspective, a deep insight on lean burn combustion is required and numerical methods to predict thermo-acoustic stability and lean blow-off in turbulent flames are essential to prevent such phenomena.

Direct CFD simulations still represent a challenge, requiring an appropriate modelling for the wide range of different phenomena involved in flame dynamic and stability processes. Thus, various modelling strategies, with huge differences in terms of physical representativeness and computational costs, can be exploited.

This research activity is therefore aimed at developing numerical methods, to be exploited into the industrial design process, which are able of describe the complex phenomena related to flame dynamics and stability and provide reliable predictions in the field of lean-burn gaseous flames for Heavy Duty Gas Turbines.

In the first part of the dissertation the state-of-the-art numerical procedure for linear thermo-acoustic analysis has been applied to the study of a practical Baker Hughes GE gas turbine combustor and validated against experimental results from a recent campaign. A methodology to calculate the flame response by means of URANS simulations coupled with System Identification techniques (CFD-SI) has been exploited, decomposing the flame in its premixed and diffusive components and allowing a deep insight on the global response: a great sensitivity to the relative phase of the sub-flames responses has been highlighted, pointing the way for further design enhancements. A Finite Element model of the combustor to be exploited for stability analysis has been built, implementing and validating a boundary condition for rotational periodicity based on Bloch-Wave theory that allows a significant reduction in computational

costs. Several sensitivities to the main operating parameters have been performed, highlighting their impact on flame response and allowing an exhaustive validation of the procedure.

In the second part of the work, simple flame configurations have been numerically investigated in order to develop advanced numerical modelling in the perspective of future applications on real technically-premixed gas turbine flames.

A LES-FGM setup able to reproduce the complex dynamics of two different turbulent swirled flames, the so-called Extended TFC model, has been developed and validated against detailed experimental measurements. The model, able to include specifically the effects of flame front stretching and heat loss allows a better prediction of the complex flame behaviour, in terms of both nonlinear flame dynamics and lean blow-off predictions, with a negligible computational cost increment.

Concerning the combustor experimentally investigated at TUB, it can be concluded that the Flame Describing Function can be successfully predicted, considering the effects of both flame stretch and heat loss into the FGM framework. Once obtained the FDF from numerical simulations, it can be used as input for weakly nonlinear thermo-acoustic analysis, in order to predict not only the onset of pressure oscillations, but also their amplitude and allowing a deeper understanding of the physics governing the flame dynamics. Results have been compared against experimental measurements and self-excited LES simulations, showing the capability of the analysis to catch the instability and the improvements that can be obtained with respect to the commonly used numerical approaches.

Regarding the Cambridge burner, the availability of detailed experimental measurements for this setup allowed an exhaustive validation of the Extended TFC model. In this framework, the correct account for high strain levels results crucial for an accurate prediction of the main evolution of flame approaching blow-off and the developed model has proven to be suitable for direct simulations of blow-off. Two lean blow-off transitories have been simulated using different flow velocities to predict the numerical extinction limits and study the blow-off dynamics and its precursors in detail. An accelerated procedure with progressive step reductions of the inlet equivalence ratio is used to trigger the flame blow-off with satisfactory accuracy. The flame behaviour during blow-off is analysed with volume-averaged and instantaneous fields of different thermo-chemical quantities. The study of the highest reactivity zones in the chamber through OH mass concentration fields allowed the observation of a particular blow-off mechanism. Three stages were identified just prior the extinction, i.e. (1) the flame positioning in the inner recirculation

zone, (2) the flame structure fragmentation and (3) the destruction of anchoring region.

The validity of the employed models and procedures, now restricted only to simple atmospheric flame configurations, can be extended to allow the flame dynamics and stability study in industrial applications, responding to main design demands.

Bibliography

[1] Lefebvre, Arthur H. and Ballal, Dilip R. *Gas Turbine Combustion*. CRC Press, Taylor & Francis Group, 2010.

[2] Leonard, G. and Stegmaier, J. "Development of an aeroderivative gas turbine dry low emissions combustion system." 116:542–546, 1993.

[3] Zajadatz, Martin, Pennell, Douglas, Bernero, Stefano, Paikert, Bettina, Zoli, Raffaele, and Döbbeling, Klaus. "Development and implementation of the advanced environmental burner for the alstom gt13e2." *Journal of Engineering for Gas Turbines and Power*, 135(6):061503, 2013.

[4] Ceccherini, G., Malquori, D., Petillo, G., and Falsini, M. Retrofitability of dln/dle systems. Technical report, GE Oil & Gas, 2013.

[5] Huber, Andreas. *Impact of fuel supply impedance and fuel staging on gas turbine combustion stability*. PhD thesis, Universität München, 2009.

[6] Huang, Ying, Wang, Shanwu, and Yang, Vigor. "Systematic analysis of lean-premixed swirl-stabilized combustion." *AIAA journal*, 44 (4):724–740, 2006.

[7] Shanbhogue, Santosh J, Husain, Sajjad, and Lieuwen, Tim. "Lean blowoff of bluff body stabilized flames : Scaling and dynamics." *Progress in Energy and Combustion Science*, 35(1):98–120, 2009.

[8] Schmitt, PA, Poinsot, T., Schuermans, B., and Geigle, K. P. "Large-eddy simulation and experimental study of heat transfer, nitric oxide emissions and combustion instability in a swirled turbulent high-pressure burner." *Journal of Fluid Mechanics*, 570:17–46, 2007.

[9] Wolf, P, Staffelbach, G, Balakrishnan, R, Roux, A, and Poinsot, Thierry. Azimuthal instabilities in annular combustion chambers. In *Proc. of the Summer Program*, pages 259–269. Citeseer, 2010.

[10] Andreini, A, Facchini, B, Giusti, A, Vitale, I, and Turrini, F. Thermoacoustic analysis of a full annular aero-engine lean combustor with multi-perforated liners. In *Proceedings of the AIAA-CEAS Aeroacoustic Conference*, 2013.

[11] Poinsot, T. "Prediction and control of combustion instabilities in real engines." *Proceedings of the Combustion Institute*, 36(1):1 – 28, 2017. ISSN 1540-7489.

[12] Andreini, Antonio, Facchini, Bruno, Giusti, Andrea, and Turrini, Fabio. "Assessment of flame transfer function formulations for the thermoacoustic analysis of lean burn aero-engine combustors." *Energy Procedia*, 45:1422–1431, 2014.

[13] Tay-Wo-Chong, Luis, Bomberg, Sebastian, Ulhaq, Ahtsham, Komarek, Thomas, and Polifke, Wolfgang. "Comparative validation study on identification of premixed flame transfer function." *Journal of Engineering for Gas Turbines and Power*, 134(2):021502, 2012.

[14] Laera, Davide, Prieur, Kevin, Durox, Daniel, Schuller, Thierry, Camporeale, SM, and Candel, Sébastien. "Impact of heat release distribution on the spinning modes of an annular combustor with multiple matrix burners." *Journal of Engineering for Gas Turbines and Power*, 139(5):051505–051505–10, 2017.

[15] Esclapez, By L, Ma, P C, and Ihme, M. "Large-eddy simulation of fuel effect on lean blow-out in gas turbines." *Center for Turbulence Research Annual Research Briefs*, pages 103–113, 2015.

[16] Zhang, Huangwei. *Extinction in Turbulent Swirling Non-premixed Flames*. PhD thesis, University of Cambridge, 2015.

[17] Hasti, VG, Kundu, P, Kumar, G, Drennan, SC, Som, S, and Gore, JP. "A Numerical Study of Flame Characteristics during Lean Blow-Out in a Gas Turbine Combustor." *2018 Joint Propulsion Conference, Cincinnati*, AIAA 2018-4955, .

[18] Klarmann, Noah, Sattelmayer, Thomas, Weiqung, Geng, and Magni, Fulvio. "Impact of Flame Stretch and Heat Loss on Heat Release Distributions in Gas Turbine Combustors: Model Comparison

and Validation." *Proceedings of ASME Turbo Expo 2016: Turbomachinery Technical Conference & Exposition (abstract accepted)*, pages 1–12, 2016.

[19] Zimont, V. "Gas premixed combustion at high turbulence. Turbulent flame closure combustion model." *Experimental Thermal and Fluid Science*, 21:179–186, 2000.

[20] Tay-Wo-Chong, Luis, Zellhuber, Mathieu, Komarek, Thomas, Im, Hong G, and Polifke, Wolfgang. "Combined Influence of Strain and Heat Loss on Turbulent Premixed Flame Stabilization." *Flow, Turbulence and Combustion*, pages 263–294, 2016.

[21] Innocenti, Alessandro, Andreini, Antonio, Facchini, Bruno, and Cerutti, Matteo. Numerical analysis of the dynamic flame response and thermo-acoustic stability of a full-annular lean partially-premixed combustor. In *ASME Turbo Expo 2016: Power for Land, Sea, and Air*. American Society of Mechanical Engineers, 2016.

[22] Mensa, G. A., Campa, G., and Moeck, J. P. "Efficient Computation of Thermoacoustic Modes in Industrial Annular Combustion Chambers Based on Bloch-Wave Theory." *ASME Journal of Engineering for Gas Turbines and Power*, 8(138), 2016.

[23] Orchini, Alessandro. *Modelling and analysis of nonlinear thermoacoustic systems using frequency and time domain methods*. PhD thesis, University of Cambridge, 2016.

[24] Palies, P., Durox, D., Schuller, T., and Candel, S. "Nonlinear combustion instability analysis based on the flame describing function applied to turbulent premixed swirling flames." *Combustion and Flame*, 158(10):1980–1991, 2011.

[25] Gockeler, K., Göke, S., Schimek, S., and O., Paschereit C. "Enhanced recirculation in the cold flow field of a swirl-stabilized burner for ultra wet combustion." *Proceedings of 3rd International Conference on Jets, Wakes and Separated Flows, Cincinnati, Ohio, 2010*, 2010.

[26] Cavaliere, Davide E. *Blowoff in Gas Turbine Combustors*. PhD thesis, University of Cambridge, 2013.

[27] Cavaliere, Davide E, Kariuki, James, and Mastorakos, Epaminondas. "A Comparison of the Blow-Off Behaviour of Swirl-Stabilized Premixed , Non-Premixed and Spray Flames." *Flow Turbulence Combustion*, pages 347–372, 2013.

[28] Kariuki, James. *Turbulent premixed flame stabilization and blow-off.* PhD thesis, University of Cambridge, 2012.

[29] Balasubramanian, Koushik and Sujith, R. I. "Non-normality and nonlinearity in combustion–acoustic interaction in diffusion flames." *Journal of Fluid Mechanics*, 594:29–57, 2008.

[30] Crocco, Luigi. "Research on combustion instability in liquid propellant rockets." *Symp. Int. Combust.*, 12:85–99, 1969.

[31] Dowling, A. P. "Nonlinear self-excited oscillations of a ducted flame." *Journal of Fluid Mechanics*, 346:271–290, 1997.

[32] Noiray, N., Durox, D., Schuller, T., and Candel, S. "A unified framework for nonlinear combustion instability analysis based on the flame describing function." *Journal of Fluid Mechanics*, 615: 139–167, 2008.

[33] Gicquel, Laurent Y M, Staffelbach, Gabriel, and Poinsot, Thierry. "Large Eddy Simulations of gaseous flames in gas turbine combustion chambers." *Progress in Energy and Combustion Science*, 38(6):782–817, 2013.

[34] Huang, Ying and Yang, Vigor. "Dynamics and stability of lean-premixed swirl-stabilized combustion." *Progress in Energy and Combustion Science*, 35(4):293–364, 2009.

[35] Dunn-Rankin, Derek. *Lean combustion: technology and control.* Academic Press, 2011.

[36] Bahr, DW. "Technology for the design of high temperature rise combustors." *Journal of Propulsion and Power*, 3(2):179–186, 1987.

[37] Ohkubo, Yoichiro. "Low-nox combustion technology." *Target*, 20 (35):24, 2005.

[38] Cocca, M. A. and Marcucci, N. Performance and reliability improvements for ms5002 gas turbines. Technical Report GER-4171, GE Power Generation.

[39] Thomas, L. L., Simons, D. W., Popovic, P., Romoser, C. E., Vandale, D. D., and Citeno, J. V. E-class dln technology advancements, dln1+. In *Proc. ASME Turbo Expo*, number GT2011-45944, 2011.

[40] Keller, Jacob J. "Thermoacoustic oscillations in combustion chambers of gas turbines." *AIAA journal*, 33(12):2280–2287, 1995.

[41] Dowling, Ann P. "The calculation of thermoacoustic oscillations." *Journal of sound and vibration*, 180(4):557–581, 1995.

[42] Mongia, H C, Held, T J, Hsiao, G C, and Pandala, R P. Incorporation of combustion instability issues into design process: Ge aeroderivative and aero engines experience. In Lieuwen, Timothy C and Yang, Vigor, editors, *Combustion instabilities in gas turbine engines (operational experience, fundamental mechanisms and modeling)*, chapter 3, pages 43–64. American Institute of Aeronautics and Astronautic, Progress in astronautics and aeronautics, 2005.

[43] Fernandes, Edgar C. and Litão, Ivo D. V. Rayleigh criterion: Theory and experiments. In *Advances in Aero-Acoustics and Thermo-Acoustics*. von Karman Institute for Fluid Dynamics, Brussels, 2010.

[44] Krebs, W, Bethke, S, Lepers, J, Flohr, P, and Prade, B. Thermoacoustic design tools and passive control: Siemens power generation approaches. In Lieuwen, Timothy C and Yang, Vigor, editors, *Combustion instabilities in gas turbine engines (operational experience, fundamental mechanisms and modeling)*, chapter 5, pages 89–112. American Institute of Aeronautics and Astronautic, Progress in astronautics and aeronautics, 2005.

[45] Rayleigh, J. S. W. *The Theory of Sound, Volume II.* MacMillan and Co, 1878.

[46] Huang, Ying and Yang, Vigor. "Dynamics and stability of lean-premixed swirl-stabilized combustion." *Progress in Energy and Combustion Science*, 35(4):293–364, 2009.

[47] Zinn, B T and Lieuwen, T C. Combustion instabilities: Basic concepts. In Lieuwen, Timothy C and Yang, Vigor, editors, *Combustion instabilities in gas turbine engines (operational experience, fundamental mechanisms and modeling)*, chapter 1, pages 3–28. American Institute of Aeronautics and Astronautic, Progress in astronautics and aeronautics, 2005.

[48] Shreekrishna, Hemchandra, Santosh, and Lieuwen, Tim. "Premixed flame response to equivalence ratio perturbations." *Combustion Theory and Modelling*, 14(5):681–714, 2010.

[49] Cho, Ju Hyeong and Lieuwen, Tim. "Laminar premixed flame response to equivalence ratio oscillations." *Combustion and Flame*, 140(1):116–129, 2005.

[50] Lieuwen, Tim and Zinn, Ben T. The role of equivalence ratio oscillations in driving combustion instabilities in low nox gas turbines. In *Symposium (International) on Combustion*, volume 27, pages 1809–1816. Elsevier, 1998.

[51] Auer, MP, Hirsch, C, and Sattelmayer, T. Influence of the interaction of equivalence ratio and mass flow fluctuations on flame dynamics. In *ASME Turbo Expo 2005: Power for Land, Sea, and Air*, pages 249–257. American Society of Mechanical Engineers, 2005.

[52] Mansour, Mohy S. "Stability characteristics of lifted turbulent partially premixed jet flames." *Combustion and Flame*, 133(3): 263–274, 2003.

[53] Plee, S. L. and Mellor, A. M. "Characteristic time correlation for lean blowoff of bluff-body-stabilized flames." *Combustion and Flame*, 35:61–80, 1979.

[54] Longwell, John P., Frost, Edward E., and Weiss, Malcolm a. "Flame Stability in Bluff Body Recirculation Zones." *Industrial & Engineering Chemistry*, 45(8):1629–1633, 1953.

[55] Williams, G. C., Hottel, H. C., and Scurlock, A. C. "Flame stabilization and propagation in high velocity gas streams." *Proceedings of the Combustion Institute*, pages 21–40, 1951.

[56] Kundu, K. M., Banerjee, D. D., and Bhaduri, D. D. "On flame stabilization by bluff-bodies." *Journal of Engineering for Power*, pages 209–314, 1980.

[57] Kundu, K. M., Banerjee, D. D., and Bhaduri, D. D. "Theoretical analysis on flame stabilization by a bluff-body." *Combustion Science and Technology*, 17(3-4):153–162, 1977.

[58] Zukoski, E. *Flame stabilization on bluff bodies at low and intermediate Reynolds numbers*. PhD thesis, 1954.

[59] Spalding, D.B. "Theoretical aspects of flame stabilization: An approximate graphical method for the flame speed of mixed gases." *Aircraft Engineering and Aerospace Technology*, 25(9):264–276, 1953.

[60] Yamaguchi, Shigeki, Ohiwa, Norio, and Hasegawa, Tatsuya. "Structure and blow-off mechanism of rod-stabilized premixed flame." *Combustion and Flame*, 62(1):31–41, 1985.

[61] Pan, J. C. and Ballal, D. R. "Chemistry and turbulence effects in bluff body stabilized flame." 1992.

[62] Driscoll, James F. "Turbulent premixed combustion: Flamelet structure and its effect on turbulent burning velocities." *Progress in Energy and Combustion Science*, 34(1):91–134, 2008.

[63] Law, Chung K. *Combustion Physics*. Cambridge University Press, 2006.

[64] Poinsot, Thierry and Veynante, Denis. *Theoretical and Numerical Combustion*. 2005.

[65] Muruganandam, Thiruchengode and Seitzman, Jerry. "Characterization of extinction events near blowout in swirl dump combustors." *American Institute of Aeronautics and Astronautics*, 4331, 2005.

[66] Chaudhuri, S., Kostka, S., Renfro, M.W., and Cetegen, B.M. "Blowoff dynamics of bluff body stabilized turbulent premixed flame." *Combustion and Flame*, 157:790–802, 2010.

[67] Kariuki, James, Dawson, James R, and Mastorakos, Epaminondas. "Measurements in turbulent premixed bluff body flames close to blow-off." *Combustion and Flame*, 159(8):2589–2607, 2012.

[68] Zhang, Q., Noble, D.R., Shanbhogue, S.J., and Lieuwen, T. "Piv measurements in h2/ch4 swirling flames under near blowoff conditions." *5th US Combustion Meeting*, (33), 2007.

[69] Polifke, Wolfgang. "Low−order analysis tools for aero− and termo−acoustic instabilities." *Advances in Aero-Acoustics and Thermo-Acoustics*, von Karman Institute for Fluid Dynamics, Brussels, 2010.

[70] Martin, Charles Etienne, Benoit, Laurent Jean-Louis, Sommerer, Yannick, Nicoud, Franck, and Poinsot, Thierry. "Large-eddy simulation and acoustic analysis of a swirled staged turbulent combustor." *AIAA journal*, 44(4):741–750, 2006.

[71] Selle, Lartigue, Lartigue, Ghislain, Poinsot, Thierry, Koch, R, Schildmacher, K-U, Krebs, W, Prade, B, Kaufmann, P, and Veynante, Denis. "Compressible large eddy simulation of turbulent combustion in complex geometry on unstructured meshes." *Combustion and Flame*, 137(4):489–505, 2004.

[72] Wolf, Pierre, Staffelbach, Gabriel, Gicquel, Laurent, and Poinsot, Thierry. Massively parallel les of azimuthal thermo-acoustic instabilities in annular gas turbines. In *Journal of Physics: Conference Series*, volume 180, page 012035. IOP Publishing, 2009.

[73] Wolf, Pierre, Balakrishnan, Ramesh, Staffelbach, Gabriel, Gicquel, Laurent YM, and Poinsot, Thierry. "Using les to study reacting flows and instabilities in annular combustion chambers." *Flow, turbulence and combustion*, 88(1-2):191–206, 2012.

[74] Boudier, Guillaume, Lamarque, Nicolas, Sensiau, Claude, Staffelbach, Gabriel, Poinsot, T, and Moureau, V. Investigating the thermo-acoustic stability of a real gas turbine combustion chamber using large-eddy simulations. In *11th CEAS-ASC Workshop and 2nd Scientific Workshop of X3-NOISE 27–28 September 2007, Lisbon, Portugal*, 2007.

[75] Chu, Boa-Teh. "On the energy transfer to small disturbances in fluid flow (part i)." *Acta Mechanica*, 1(3):215–234, 1965.

[76] Nicoud and Wieczorek. "About the zero mach number assumption in the calculation of thermoacoustic instabilities." *International journal of spray and combustion dynamics*, 1(1):67–111, 2009.

[77] Walz, Günther, Krebs, Werner, Hoffmann, Stefan, and Judith, Hans. "Detailed analysis of the acoustic mode shapes of an annular combustion chamber." *Journal of engineering for gas turbines and power*, 124(1):3–9, 2002.

[78] Nicoud, Franck, Benoit, Laurent, Sensiau, Claude, and Poinsot, Thierry. "Acoustic modes in combustors with complex impedances and multidimensional active flames." *AIAA journal*, 45 (2):426–441, 2007.

[79] Camporeale, SM, Fortunato, B, and Campa, G. "A finite element method for three-dimensional analysis of thermo-acoustic combustion instability." *Journal of Engineering for Gas Turbines and Power*, 133(1):011506, 2011.

[80] Dowling, Ann P and Stow, Simon R. "Acoustic analysis of gas turbine combustors." *Journal of propulsion and power*, 19(5):751–764, 2003.

[81] Campa, Giovanni and Camporeale, Sergio Mario. "Prediction of the thermoacoustic combustion instabilities in practical annular combustors." *Journal of Engineering for Gas Turbines and Power*, 136(9):091504, 2014.

[82] Campa, Giovanni, Camporeale, Sergio Mario, Cosatto, Ezio, and Mori, Giulio. Thermoacoustic analysis of combustion instability through a distributed flame response function. In *ASME Turbo Expo 2012: Turbine Technical Conference and Exposition*, pages 179–188. American Society of Mechanical Engineers, 2012.

[83] Andreini, A, Facchini, B, Giusti, A, Turrini, F, and Vitale, I. Thermoacoustic analysis of an advanced lean injection system in a tubular combustor configuration. In *Proceedings of the COMSOL Conference 2012 Milan*, 2012.

[84] Andreini, Antonio, Facchini, Bruno, Giusti, Andrea, Vitale, Ignazio, and Turrini, Fabio. Thermoacoustic analysis of a full annular lean burn aero-engine combustor. In *ASME Turbo Expo 2013: Turbine Technical Conference and Exposition*, pages V01AT04A069–V01AT04A069. American Society of Mechanical Engineers, 2013.

[85] Pampaloni, Daniele, Andreini, Antonio, Facchini, Bruno, and Paschereit, Christian Oliver. Les modelling of the flame describing function of a lean premixed swirl stabilized flame. In *2018 Joint Propulsion Conference*, page 4608, 2018.

[86] Laera, Davide and Camporeale, Sergio M. "A weakly nonlinear approach based on a distributed flame describing function to study the combustion dynamics of a full-scale lean-premixed swirled burner." *Journal of Engineering for Gas Turbines and Power*, 139(9):091501–091501–11, 2017.

[87] Laera, D., Campa, G., and Camporeale, S.M. "A finite element method for a weakly nonlinear dynamic analysis and bifurcation tracking of thermo-acoustic instability in longitudinal and annular combustors." *Applied Energy*, 187:216 – 227, 2017. ISSN 0306-2619.

[88] Polifke, Wolfgang, Paschereit, Christian Oliver, and Döbbeling, Klaus. "Constructive and destructive interference of acoustic

and entropy waves in a premixed combustor with a choked exit." *Int. J. Acoust. Vib*, 6(3):135–146, 2001.

[89] Bellucci, Valter, Schuermans, Bruno, Nowak, Dariusz, Flohr, Peter, and Paschereit, Christian Oliver. Thermoacoustic modeling of a gas turbine combustor equipped with acoustic dampers. In *ASME Turbo Expo 2004: Power for Land, Sea, and Air*, pages 635–644. American Society of Mechanical Engineers, 2004.

[90] Hubbard, S and Dowling, AP. "Acoustic resonances of an industrial gas turbine combustion system." *Journal of engineering for gas turbines and power*, 123(4):766–773, 2001.

[91] Candel, Sébastien, Durox, Daniel, Schuller, Thierry, Bourgouin, Jean-François, and Moeck, Jonas P. "Dynamics of swirling flames." *Annual Review of Fluid Mechanics*, 46(1):147–173, 2014.

[92] Moeck, Jonas P. and Paschereit, Christian Oliver. "Nonlinear interactions of multiple linearly unstable thermoacoustic modes." *International Journal of Spray and Combustion Dynamics*, 4(1):1–27, 2012.

[93] Lauer, Martin and Sattelmayer, Thomas. "On the adequacy of chemiluminescence as a measure for heat release in turbulent flames with mixture gradients." *Journal of Engineering for Gas Turbines and Power*, 132(6):061502, 2010.

[94] Chong, Luis Tay Wo, Komarek, Thomas, Kaess, Roland, Föller, Stephan, and Polifke, Wolfgang. Identification of flame transfer functions from les of a premixed swirl burner. In *ASME Turbo Expo 2010: Power for Land, Sea, and Air*, pages 623–635. American Society of Mechanical Engineers, 2010.

[95] Crocco, Luigi and Cheng, Sin-I. *Theory of combustion instability in liquid propellant rocket motors*. Cambridge Univ Press, 1956.

[96] Sattelmayer, Thomas. "Influence of the combustor aerodynamics on combustion instabilities from equivalence ratio fluctuations." *Journal of Engineering for Gas Turbines and Power(Transactions of the ASME)*, 125(1):11–19, 2003.

[97] Polifke, Wolfgang, Kopitz, Jan, and Serbanovic, Ana. Impact of the fuel time lag distribution in elliptical premix nozzles on combustion stability. In *7th AIAA/CEAS Aeroacoustics Conference*, pages 2001–2104, 2001.

[98] Dowling, Ann P. "A kinematic model of a ducted flame." *Journal of fluid mechanics*, 394:51–72, 1999.

[99] Pankiewitz, Christian. *Hybrides Berechnungsverfahren für thermoakustische Instabilitäten von Mehrbrennersystemen.* PhD thesis, Universität München, 2004.

[100] Hirsch, C, Fanaca, D, Reddy, P, Polifke, W, and Sattelmayer, T. Influence of the swirler design on the flame transfer function of premixed flames. In *ASME Turbo Expo 2005: Power for Land, Sea, and Air*, pages 151–160. American Society of Mechanical Engineers, 2005.

[101] Eckstein, J, Freitag, E, Hirsch, C, Sattelmayer, T, Von der Bank, R, and Schilling, T. Forced low-frequency spray characteristics of a generic airblast swirl diffusion burner. In *ASME Turbo Expo 2003, collocated with the 2003 International Joint Power Generation Conference*, pages 471–478. American Society of Mechanical Engineers, 2003.

[102] Eckstein, Johannes. *On the mechanisms of combustion driven low-frequency oscillations in aero-engines.* PhD thesis, Universität München, 2004.

[103] Eckstein, Johannes and Sattelmayer, Thomas. "Low-order modeling of low-frequency combustion instabilities in aeroengines." *Journal of propulsion and power*, 22(2):425–432, 2006.

[104] Hettel, Matthias, Habisreuther, Peter, Büchner, Horst, Bockhorn, Henning, and Zarzalis, Nikolaos. Urans-modelling of flame transfer functions of turbulent premixed jet flames. In *ASME Turbo Expo 2004: Power for Land, Sea, and Air*, pages 517–526. American Society of Mechanical Engineers, 2004.

[105] Kostrzewa, Krzysztof. *Advanced computational methods in identification of thermo-acoustic systems.* PhD thesis, Universität Stuttgart, 2011.

[106] Hermeth, Sebastian. *Mechanisms affecting the dynamic response of swirled flames in gas turbines.* PhD thesis, Toulouse, INPT, 2012.

[107] Hermeth, Sebastian, Staffelbach, Gabriel, Gicquel, Laurent YM, and Poinsot, Thierry. "Les evaluation of the effects of equivalence ratio fluctuations on the dynamic flame response in a real gas turbine

combustion chamber." *Proceedings of the Combustion Institute*, 34 (2):3165–3173, 2013.

[108] Hermeth, Sebastian, Staffelbach, Gabriel, Gicquel, Laurent YM, Anisimov, Vyacheslav, Cirigliano, Cinzia, and Poinsot, Thierry. "Bistable swirled flames and influence on flame transfer functions." *Combustion and Flame*, 161(1):184–196, 2014.

[109] Ljung, Lennart. *System identification*. Springer, 1998.

[110] Polifke, W, Poncet, A, Paschereit, CO, and Döbbeling, K. "Reconstruction of acoustic transfer matrices by instationary computational fluid dynamics." *Journal of Sound and Vibration*, 245(3):483–510, 2001.

[111] Polifke, Wolfgang and Gentemann, Alexander. "Order and realizability of impulse response filters for accurate identification of acoustic multi-ports from transient cfd." *Int. J. of Acoustics and Vibration*, 9(3):139–148, 2004.

[112] Komarek, Thomas and Polifke, Wolfgang. "Impact of swirl fluctuations on the flame response of a perfectly premixed swirl burner." *Journal of Engineering for Gas Turbines and Power*, 132(6):061503, 2010.

[113] Huber and Polifke. "Dynamics of practical premixed flames, part i: model structure and identification." *International journal of spray and combustion dynamics*, 1(2):199–228, 2009.

[114] Huber and Polifke. "Dynamics of practical premixed flames, part ii: identification and interpretation of cfd data." *International journal of spray and combustion dynamics*, 1(2):229–249, 2009.

[115] Polifke, Wolfgang. System identification for aero-and thermo-acoustic applications. In *Advances in Aero-Acoustics and Thermo-Acoustics*. von Karman Institute for Fluid Dynamics, Brussels, 2010.

[116] Yang, Yang, Noiray, Nicolas, Scarpato, Alessandro, Schulz, Oliver, Düsing, K Michael, and Bothien, Mirko. Numerical analysis of the dynamic flame response in alstom reheat combustion systems. In *ASME Turbo Expo 2015: Turbine Technical Conference and Exposition*, pages V04AT04A048–V04AT04A048. American Society of Mechanical Engineers, 2015.

[117] Innocenti, A., Andreini, A., and Facchini, B. Numerical identification of a premixed flame transfer function and stability analysis of a lean burn combustor. volume 82, pages 358–365, 2015.

[118] Innocenti, Alessandro, Andreini, Antonio, Facchini, Bruno, and Peschiulli, Antonio. "Numerical analysis of the dynamic flame response of a spray flame for aero-engine applications." *International Journal of Spray and Combustion Dynamics*, 9(4):310–329, 2017.

[119] Li, Jingxuan and Morgans, Aimee S. "Time domain simulations of nonlinear thermoacoustic behaviour in a simple combustor using a wave-based approach." *Journal of Sound and Vibration*, 346:345 – 360, 2015. ISSN 0022-460X.

[120] Armitage, C.A., Balachandran, R., Mastorakos, E., and Cant, R.S. "Investigation of the nonlinear response of turbulent premixed flames to imposed inlet velocity oscillations." *Combustion and Flame*, 146 (3):419 – 436, 2006. ISSN 0010-2180.

[121] Krediet, H. J., Beck, C. H., Krebs, W., Schimek, S., O., Paschereit C., and Kok, J. B. W. "Identification of the flame describing function of a premixed swirl flame from les." *Combustion Science and Technology*, 184(7-8):888–900, 2012.

[122] Han, Xingsi and Morgans, Aimee S. "Simulation of the flame describing function of a turbulent premixed flame using an open-source les solver." *Combustion and Flame*, 162(5):1778 – 1792, 2015. ISSN 0010-2180.

[123] Karimi, Nader, Brear, Michael J., Jin, Seong-Ho, and Monty, Jason P. "Linear and non-linear forced response of a conical, ducted, laminar premixed flame." *Combustion and Flame*, 156(11):2201 – 2212, 2009. ISSN 0010-2180.

[124] Balachandran, R., Ayoola, B.O., Kaminski, C.F., Dowling, A.P., and Mastorakos, E. "Experimental investigation of the nonlinear response of turbulent premixed flames to imposed inlet velocity oscillations." *Combustion and Flame*, 143(1):37 – 55, 2005. ISSN 0010-2180.

[125] Schimek, S., Moeck, J. P., and Paschereit, C. O. "An Experimental Investigation of the Nonlinear Response of an Atmospheric Swirl-Stabilized Premixed Flame." *ASME Journal of Engineering for Gas Turbines and Power*, 10(133), 2011.

[126] Silva, Camilo Fernando, Nicoud, Franck, Schuller, Thierry, Durox, Daniel, and Candel, Sebastien. "Combining a helmholtz solver with the flame describing function to assess combustion instability in a premixed swirled combustor." *Combustion and Flame*, 160(9):1743 – 1754, 2013. ISSN 0010-2180.

[127] Black, David, Crocker, D. Scott, and Smith, Clifford. "Transient Lean Blowout Modeling of an Aero Low Emission Fuel Injector." *39th AIAA/ASME/SAE/ASEE Joint Propulsion Conference and Exhibit*, (July):1–9, 2003.

[128] Lefebvre, A. H. "Fuel Effects on Gas Turbine Combustion — Ignition , Stability, and Combustion Efficiency." 107(24), 1985.

[129] Feikema, Douglas, Chen, Ruey-Hung, and Driscoll, J. F. "Enhancement of Flame Blowout Limits by the Use of Swirl." 195:183–195, 1990.

[130] Ateshkadi, Arash, McDonell, V. G., and Samuelsen, G. S. "Lean blowout model for a spray-fired swirl-stabilized combustor." 28: 1281–1288, 2000.

[131] Soroudi, M. A., Bafekr, S. Hadi, Timaji, M., and Rasooli, N. "A Priori Calculation of Lean Blowout Limit in an Industrial Gas Turbine Combustor." *Proceedings of the European Combustion Meeting*, (January), 2013.

[132] Sturgess, G. and Shouse, D. "A hybrid model for calculating lean blowouts in practical combustors." *American Institute of Aeronautics and Astronautics - 32nd Joint Propulsion Conference and Exhibit*, 1996.

[133] Zubrilin, Roman A, Zubrilin, Ivan A, Matveev, S. S., and Matveev, S. G. "Gaseous fuel flame stabilization in a modular swirled burner." *Proceedings of ASME Turbo Expo 2016: Turbomachinery Technical Conference and Exposition*, pages 1–10, 2016.

[134] Pierce, Charles D. and Moin, Parviz. "Progress-variable approach for large-eddy simulation of non-premixed turbulent combustion." *Journal of Fluid Mechanics*, 504:73–97, 2004.

[135] Zhang, Huangwei and Mastorakos, Epaminondas. "Prediction of Global Extinction Conditions and Dynamics in Swirling Nonpremixed Flames Using LES / CMC Modelling." *Flow, Turbulence and Combustion*, pages 863–889, 2016.

[136] Hasti, VG, Kundu, P, Kumar, G, Drennan, SC, Som, S, Won, SH, Dryer, FL, and Gore, JP. "Lean blow-out (LBO) computations in a gas turbine combustor." *2018 Joint Propulsion Conference, Cincinnati*, AIAA 2018-4958, .

[137] Lilly, D K. "A Proposed Modification of the Germano-Subgrid-Scale Closure Method." *Physics of Fluids A*, 4(3):633–635, 1992.

[138] Peters, Norbert. *Turbulent Combustion*. 2000.

[139] ANSYS. Fluent 16 Theory Guide, 2014.

[140] Ramaekers, W.J.S., Albrecht, B.A., van Oijen, J.A., de Goey, L.P.H.;, and Eggels, R.L.G.M. "The Application of Flamelet Generated Manifolds in the partially-premixed flames." *Proceedings of the Fluent Benelux User Group Meeting*, (October): 1–5, 2005.

[141] Goldin, Graham, Montanari, Federico, and Patil, Sunil. "A Comparison of RANS and LES of an Industrial Lean Premixed Burner." *ASME Turbo Expo 2014*, 2014.

[142] Zimont, Vladimir, Polifke, Wolfgang, Bettelini, Marco, and Weisenstein, Wolfgang. "An efficient computational model for premixed turbulent combusiton at high reynolds numbers based on a turbulent flame speed closure." *International Gas Turbine & Aeroengine Congress & Exhibition*, pages 1–10, 1997.

[143] Flohr, P and Pitsch, H. "A turbulent flame speed closure model for LES of industrial burner flows." *Center for Turbulence Research, Proceedings of the summer program*, pages 169–179, 2000.

[144] Bray, K. N. C. *Complex Chemical Reaction Systems. Mathematical Modelling and Simulation*. Springer Verlag, 1987.

[145] Zimont, V. L. and Battaglia, V. "Joint RANS/LES approach to premixed flame modelling in the context of the TFC combustion model." *Flow, Turbulence and Combustion*, 77(1-4):305–331, 2006.

[146] Poinsot, T., Veynante, D., and Candel, S. "Quenching processes and premixed turbulent combustion diagrams." *Journal of Fluid Mechanics*, 228:561, 1991.

[147] Tay-Wo-Chong, Luis, T. Komarek, M. Zellhuber, Lenz, J., Hirsch, C., and Polifke, W. Influence of strain and heat loss on flame stabilization in a non-adiabatic combustor. In *Proceedings of the European Combustion Meeting*, pages 1–6, 2009.

[148] Schmid, H., Habisreuther, P., and Leuckel, W. "A model for calculating heat release in premixed turbulent flames." *Combustion and Flame*, 113(3):79–91, 1998.

[149] Tay-Wo-Chong, Luis, Scarpato, Alessandro, and Polifke, Wolfgang. LES Combustion Model with Stretch and Heat Loss Effects for Prediction of Premix Flame Characteristics and Dynamics. In *Proceedings of ASME Turbo Expo 2017: Turbomachinery Technical Conference and Exposition*, pages 1–12, 2017.

[150] Mantel, T. and Samaniego, J.M. "Fundamental mechanisms in premixed turbulent flame propagation via vortex-flame interactions Part II: numerical simulation." *Combustion and Flame*, 118:557–582, 1999.

[151] Veynante, D., Piana, J., Duclos, J.M., and Martel, C. "Experimental analysis of flame surface density models for premixed turbulent combustion." *Symposium (International) on Combustion*, 26:413–420, 1996.

[152] Meneveau, C. and Poinsot, T. "Stretching and quenching of flamelets in premixed turbulent combustion." *Combustion and Flame*, 86(4): 311–332, 1991.

[153] Zhu, M, Dowling, AP, and Bray, KNC. "Transfer function calculations for aeroengine combustion oscillations." *Journal of Engineering for Gas Turbines and Power*, 127(1):18–26, 2005.

[154] Andreini, Antonio, Facchini, Bruno, Innocenti, Alessandro, and Cerutti, Matteo. Flame transfer function identification and thermoacoustic analysis of an annular heavy-duty gas turbine combustor. In *22nd International Congress on Sound and Vibrations, Florence, Italy*. International Institute of Acoustics and Vibration (IIAV) and Associazione Italiana di Acustica (AIA), 2015.

[155] Camporeale, S. M., Fortunato, B., and Campa, G. "A Finite Element Method for Three-Dimensional Analysis of Thermoacoustic Combustion Instability." *ASME Journal of Engineering for Gas Turbines and Power*, 1(133):011506, 2011.

[156] Chu, Boa-Teh. "On the energy transfer to small disturbances in fluid flow (part i)." *Acta Mechanica*, 1(3):215–234, 1965.

[157] Multiphysics, COMSOL. "Acoustics module user guide version 4.3b." *User's Manual*, 2013.

[158] Lehoucq, Richard B, Sorensen, Danny C, and Yang, Chao. *ARPACK users' guide: solution of large-scale eigenvalue problems with implicitly restarted Arnoldi methods*. Siam, 1998.

[159] Walz, G., Krebs, W., Hoffmann, S., and Judith, H. "Detailed Analysis of the Acoustic Mode Shapes of an Annular Combustion Chamber." *ASME Journal of Engineering for Gas Turbines and Power*, 9(136):3–9, 2002.

[160] Campa, G. and Camporeale, S. M. "Prediction of the Thermoacoustic Combustion Instabilities in Practical Annular Combustors." *ASME Journal of Engineering for Gas Turbines and Power*, 1(124): 091504, 2014.

[161] Bloch, F. "Über die Quantenmechanik der Elektronen in Kristallgittern." *Zeitschrift für Physik*, 7-8(52):555–600, 1929.

[162] M. Cerutti, R. Modi, D. Kalitan, and K. K. Singh. Design improvement survey for nox emissions reduction of a heavy-duty gas turbine partially premixed fuel nozzle operating with natural gas: experimental campaign. 2015.

[163] Innocenti, A. *Numerical analysis of the dynamic response of practical gaseous and liquid fuelled flames for heavy-duty and aero-engine gas turbines*. PhD thesis, University of Florence, Department of Industrial Engineering, 2015.

[164] Shih, T. H., Liou, W. W., Shabbir, A., Yang, Z., and Zhu, J. "A New - Eddy-Viscosity Model for High Reynolds Number Turbulent Flows - Model Development and Validation." *Computers Fluids.*, 24(3):227–238, 1995.

[165] Innocenti, Alessandro, Andreini, Antonio, Giusti, Andrea, Facchini, Bruno, Cerutti, Matteo, Ceccherini, Gianni, and Riccio, Giovanni. Numerical Investigations of NOx Emissions of a Partially Premixed Burner for Natural Gas Operations in Industrial Gas Turbine. In *ASME Turbo Expo 2014: Turbine Technical Conference and Exposition*. American Society of Mechanical Engineers, 2014.

[166] Knudsen, E and Pitsch, H. "Large-Eddy Simulation for Combustion Systems: Modeling Approaches for Partially Premixed Flows." *Open Thermodynamics Journal*, 4:76–85, 2010.

[167] Leuckel, W. "Swirl Intensities, Swirl Types and Energy Losses of Different Swirl Generating Devices, 1967.

[168] Schneider, C. *Über die Charakterisierung von Turbulenzstrukturen in verdrallten Strömungen.* PhD thesis, 2005.

[169] Van Oijen, J.A., Donini, A., Bastiaans, R.J.M., ten Thije Boonkkamp, J., and de Goey, L. "State-of-the-art in premixed combustion modeling using flamelet generated manifolds." *Progress in Energy and Combustion Science*, 57:30–74, 2016.

[170] Pampaloni, D., Bertini, D., Puggelli, S., Mazzei, L., and Andreini, A. "Methane swirl-stabilized lean burn flames: assessment of scale-resolving simulations." *Energy Procedia*, 126:834–841, 2017.

[171] Oberleithner, K., Schimek, S., and Paschereit, C.O. "Shear flow instabilities in swirl-stabilized combustors and their impact on the amplitude dependent flame response: A linear stability analysis." *Combustion and Flame*, 162(1):86–99, 2015.

[172] COMSOL. COMSOL Multiphysics User's Manual, 2016.

[173] Krebs, W., Krediet, H., Portillo, E., Hermeth, S., Poinsot, T., Schimek, S., and Paschereit, C. O. "Comparison of nonlinear to linear thermoacoustic stability analysis of a gas turbine combustion system." *Journal of Engineering for Gas Turbines and Power*, 135 (8):86–99, 2013.

[174] Nassini, P. C., Pampaloni, D., Andreini, A., and Meloni, R. "Large eddy simulation of lean blow-off in a premixed swirl stabilized flame." *Proceedings of ASME TURBO EXPO 2019: Turbomachinery Technical Conference and Exposition*, 2019.

[175] Nassini, P. C., Pampaloni, D., and Andreini, A. "Impact of Stretch and Heat Loss on Flame Stabilization in a Lean Premixed Flame approaching Blow-off." *Energy Procedia*, 148:250–257, 2018.

[176] Letty, C, Mastorakos, E, Masri, A R, Juddoo, M, and Loughlin, W O. "Structure of igniting ethanol and n-heptane spray flames with and without swirl." *Exp. Therm. and Fluid Sci.*, 43:47–54, 2012.

[177] Marchione, T., Ahmed, S. F., and Mastorakos, E. "Ignition of turbulent swirling n-heptane spray flames using single and multiple sparks." *Combustion and Flame*, 156(1):166–180, 2009.

[178] Beer, J. M. and Chigier, N. A. "Combustion aerodynamics." *Applied Science*, pages 100–146, 1972.

[179] Yuan, R, Kariuki, J, Dowlut, A, Balachandran, R, and Mastorakos, E. "Reaction zone visualisation in swirling spray n-heptane flames." *Proceedings of the Combustion Institute*, 35(1):1649–1656, 2015.

[180] Sidey, J and Mastorakos, E. "Visualisation of turbulent swirling dual-fuel flames." *Proceedings of the Combustion Institute*, pages 1–7, 2016.

[181] Hassel, Egon P. and Linow, Sven. "Laser diagnostics for studies of turbulent combustion." *Measurement Science and Technology*, 11 (2):37–57, 2000.

[182] Sidey, J. A. M., Giusti, A, Benie, P., and Mastorakos, E. The swirl flames data repository, 2017. URL `http://swirl-flame.eng.cam.ac.uk`.

[183] Launder, B. E. and Spalding, D. B. "The Numerical Computation of Turbulent Flows." *Computer Methods in Applied Mechanics and Engineering*, 3:269–289, 1974.

[184] Ma, Peter C., Wu, Hao, Labahn, Jeffrey W., Jaravel, T., and Ihme, Matthias. "Analysis of transient blow-out dynamics in a swirl-stabilized combustor using large-eddy simulations." *Proc. Combust. Inst.*, pages 1–10, 2018.